Surf Zone Hydrodynamics

by

Yoshimitsu Tajima

B.S., Civil Engineering (1996)
University of Tokyo

Submitted to the Department of Civil and Environmental Engineering
in partial fulfillment of the requirements for the degree of

Master of Science in Civil and Environmental Engineering

at the

MASSACHUSETTS INSTITUTE OF TECHNOLOGY

June 2001

Signature of Author .....
Department of Civil and Environmental Engineering
May 11, 2001

Certified by .....
Ole S. Madsen
Professor, Civil and Environmental Engineering
Thesis Supervisor

Accepted by .....
Oral Buyukozturk
Chairman, Departmental Committee on Graduate Studies

Surf Zone Hydrodynamics

by

Yoshimitsu Tajima

Submitted to the Department of Civil and Environmental Engineering
on May 11, 2001, in partial fulfillment of the
requirements for the degree of
Master of Science in Civil and Environmental Engineering

Abstract

A hydrodynamics model for the surf-zone is developed. Although a strong non-linearity is expected inside the surf-zone, we apply linear wave theory by adopting an equivalent linear wave which takes non-linearity into account. The model consists of following three elements. (1) Non-linear wave asymmetry and skewness model, (2) Breaking wave dissipation model and (3) Undertow model.

Numerical experiments are performed using Nwogu's (1993) Boussinesq equations. Under the assumption that the energy flux is conserved between theories, several non-linear wave parameters are extracted from the experiments and expressed in terms of equivalent linear wave parameters. Using these parameters, we propose a methodology to represent the non-linear wave height and non-linear bottom orbital velocity profile from the equivalent linear wave conditions.

We apply Watanabe's (1984) breaking criteria to breaking of the equivalent linear wave. The breaking wave attenuation model is a modification and combination of Dally et al.'s (1985) and Watanabe and Dibajnia's (1988) wave energy dissipation models. The value of a parameter, which was taken as a single constant value by Dally et al. (1985), is determined semi-empirically to be a function of the bottom slope.

Based on the two-dimensional horizontal momentum equation, the theoretical formulation of the time-averaged undertow profile is derived. This formula requires evaluation of three unknown variables. All these variables are expressed by the equivalent linear wave. A new formulation of a surface roller model is introduced to explain the excess amount of return flow inside the surf-zone. Our surface roller model also explains the observation that the surface shear stress, right after breaking, acts in the seaward direction.

The validity of the various models is examined through comparison with experimental data. Since all the models are based on the equivalent linear wave, they are easy to apply to practical problems. Moreover, linear wave theory also enables us to extend the models to random wave conditions.

Thesis Supervisor: Ole S. Madsen
Title: Professor, Civil and Environmental Engineering

Acknowledgements

First of all, I am so grateful to have the opportunity to work with Professor Ole S. Madsen. He has taken so much time to help me and provide stimulating discussions. Through the discussions, I had learned a lot of things that are very helpful to accomplish the thesis. His conscientious proofreading was also appreciated.

I also thank all my friends at MIT and my wife, Kayo, who have not only given me helpful advice but also provided plenty of relaxing time.

Finally, I gratefully acknowledge the financial support over two years of my Master's study at MIT by my company, Penta-Ocean Construction.

Contents

List of Figures

List of Tables

Chapter 1

1. Introduction

1.1 General Remarks

The estimation of beach erosion is one of the most significant concerns to coastal engineers. It is generally known that beach topography change is caused by the unbalance of the bottom sediment transport due to waves and currents. One of the simplest models for evaluating the beach erosion is to predict the equilibrium beach profile. The equilibrium beach profile is defined as having a local, time-averaged, cross-shore sediment transport of zero and a constant long-shore sediment transport. By estimating the equilibrium beach profile, we establish the stationary beach characteristics over long periods of time.

A large number of models for evaluating the equilibrium beach profile have been proposed. Generally, two different approaches have been taken to establish these models. One is an empirical approach and the other is a process-based approach. Although an empirical approach is simple and easy to use, it is difficult to apply to arbitrary conditions such as various waves, currents and sediment characteristics. A process-based approach is therefore preferable since it

will allow various conditions to be taken into account.

A process-based model generally consists of two steps. First step is to evaluate wave and current conditions, which cause sediment transport. The second step is to estimate sediment transport rates from wave and current conditions and eventually to determine the equilibrium beach profile. Generally, the process-based model requires the more detailed and accurate information on wave and current conditions since it is based on the evaluation of physical processes. Moreover, it is also important to evaluate appropriate wave and current conditions effectively because the process-based model tends to require more complicated and time-consuming computations.

The goal of this study is, therefore, to develop wave and current models, which are sufficiently reliable to form the basis for a process-based equilibrium beach profile model.

1.2 Previous Equilibrium Beach Profile Models

1.2.1 Empirical Model

Of the empirical models for estimating the equilibrium beach profile, the Bruun/Dean model (Bruun, 1954; Dean, 1977) is the best known. According to this model, the beach profile is estimated by the form, $h \propto x^m$, where h is the water depth and x is the distance from the shoreline toward offshore. From a large number of measured beach profiles, m is empirically estimated as m=2/3. If assuming that the depth should be determined by wave dissipation per unit volume being constant, the value of m, $m=2/3$, is derived by following procedures. If wave dissipation per unit surface area is $\overline{D}$ in water depth, h, then the energy dissipation per unit volume is

$$\varepsilon = \frac{\overline{D}}{h}\,, \tag{1.1}$$

where ε is assumed constant. Since the energy dissipation is related to the energy flux and taking the wave height inside the surf zone to be approximately proportional to the water depth,

$$\varepsilon = \frac{\overline{D}}{h} = \frac{d(EC_g)}{dx}\frac{1}{h} \propto \frac{d(H^2\sqrt{h})}{dx}\frac{1}{h} \propto \frac{d(h^{5/2})}{dx}\frac{1}{h} \propto h^{1/2}\frac{dh}{dx}\,. \tag{1.2}$$

Since ε is a constant, equation (1.2) results in,

$$h = Ax^{2/3} \tag{1.3}$$

where A is a sediment scale parameter (Dean,1991). Clearly, this formula is valid only inside the surf zone.

The most conspicuous advantage of this model is its simplicity although it is not clear how energy dissipation per unit volume actually moves sediments. In spite of its simplicity, this model agrees well with numerous beach profiles. Because of its simplicity and applicability to the prediction of beach profiles, this model has gained considerable recognition.

This empirical model, however, includes a few significant weak points. First, the model does not consider the different wave conditions although it is generally known that the steeper the wave, the steeper the beach slope tends to become. Second, this model is applicable only inside the surf zone because the model assumes that wave heights linearly decrease as water depth decreases. These points detract from the applicability of the model to the more general estimation of beach profiles.

According to Inman et al. (1993), the whole beach profile including the area outside the surf zone is approximately estimated by connecting two different formulas at the breaking point.

They applied the formula, $h=Ax^m$, both inside and outside of the surf zone with little theoretical background, where A and m are determined by a more complicated empirical methodology. For example, the averaged values of these parameters are $A=1.06$ and $m=0.36$ outside the surf-zone and $A=0.78$ and $m=0.41$ inside the surf-zone. By using these different parameters inside/outside the surf-zone, the Inman et al. (1993) model can predict the bar-profile around the breaking point.

However, this model loses the simplicity, which is the strongest advantage of the empirical models. Besides the determinations of A and m inside/outside the surf-zone, this model also requires the determination of the origins of these two fitting curves inside/outside the surf-zone, which directly affects the location of the bar. For example, the height of the origin for the fitting curve inside the surf-zone is 3~4 m above the still water level and the depth in which the two curves are switched is 2~4m below the still water level. The ambiguity of the determination of these origins also makes it difficult to apply this model to more general predictions of equilibrium beach profiles.

1.2.2 Energetics-based Model

As mentioned above, empirical models have their limitations. In order to improve the model accuracy and applicability for a variety of local conditions, it is necessary to understand the mechanism of shore erosion. In this sense, therefore, a process-based model is to be preferred.

The basic idea of the process-based model is, (1) estimating local sediment transport rate and (2) evaluating the equilibrium beach profile assuming that it should reach its equilibrium state when local sediment transport rate is close to zero at any point along the profile. The local sediment transport rate, i_t, is denoted as the sum of both bedload transport rate, i_b, and suspended

transport rate, i_s, i.e.,

$$i_t = i_b + i_s = 0 \tag{1.4}$$

To estimate the local sediment transport rate, two different approaches, energetics-based and traction-based, have been taken. The traction-based model is discussed in the next section.

The concept of energetics-based approach is that a portion of fluid energy is expended in maintaining a sediment transport load. As an example of this approach, Bailard's model(1981), which is an improved version of Bagnold's model(1963), is well known. In this model the rate of work done in moving sediments at the speed, u_s, should be equal to some fraction of the total energy dissipation. The resulting bedload transport rate is expressed as,

$$\vec{i}_b = \frac{u_s}{|u_s|} \frac{\varepsilon_b \Omega}{\cos\beta \left(\tan\phi - \frac{u_s}{|u_s|} \tan\beta \right)} \tag{1.5}$$

where ε_b is the efficiency factor for the bedload, β is the slope of the beach, ϕ is the internal angle of friction, ρ is the fluid density and ρ_s is the sediment density. The total dissipated energy Ω is expressed as

$$\Omega = \overline{\tau(t)u(t)} = \rho C_d \overline{|u(t)^3|} \tag{1.6}$$

where C_d is the drag coefficient. Similarly, assuming that a fraction of the total amount of energy dissipated in the stream should be equal to the amount of energy necessary to keep sediment suspended, Bailard also derived the suspended transport rate in the normal steady flow as,

$$i_s = \frac{\varepsilon_s \Omega}{w_f / u_s - \varepsilon_s \sin\beta} \tag{1.7}$$

where w_f is the average sediment fall velocity, ε_s is the efficiency factor for suspended load. In

this formula, uniform steady flow in the down-slope direction is assumed for evaluating the energy dissipation in the stream. Since these formulae include the beach slope, they may be used to find the equilibrium slope, which gives a total sediment rate of zero.

However, this approach includes a few vital weaknesses. First of all, there is no physical justification for using Bailard's suspended transport for coastal environments, where oscillatory flow is supposed to exist, since equation (6) is derived only for normal steady flow. Second, efficiency factors are hard to quantify and have been shown to fluctuate with varying hydrodynamic conditions (Nairn and Southgate, 1993). To make matters worse, furthermore, these efficiency factors have a great influence on the beach profile. Third, this model also has no threshold for sediment motion, i.e., this model can be used only under strong wave conditions. In addition to these weaknesses, this model also cannot be applied to coupled wave-current theory. In this sense, therefore, the energetics-based approach seems to be too limiting.

1.2.3 Traction-based Model

Traction-based models, such as Madsen and Grant(1976) or Madsen(1991), estimate the sediment transport rate as the total movement of sediment grains, which are induced to move by friction forces acting on the grains by the moving fluid. Meyer and Madsen(1998) applied this model to the prediction of equilibrium beach profiles. Their model is mainly based on the following four concepts.

(a) The local sediment transport rate, i_t, is denoted as the sum of both bedload transport rate, i_b, and suspended transport rate, i_s, (Equation (1.4)).

(b) Sediment transport rate induced by waves on a plane bottom is in the shoreward direction

because of wave non-linearity.

(c) Bottom slope in the seaward direction cancels the shoreward sediment transport due to wave non-linearity.

(d) In the surf zone, the offshore flow induced by breaking waves, the undertow, has the effect of moving suspended sediment in the sea-ward direction and, as a result, produces bar profile around the breaking point.

Based on these concepts, Meyer and Madsen (1998) suggested two major advantages of their model compared to energetics-based models. First, there is no empirical efficiency factor. Second, the mechanics of sediment transport based on a traction model makes it possible to incorporate wave-current interaction and a sediment movement threshold. Hereafter, the components of their model are briefly introduced and advantages of the model are also discussed.

(1) Bedload Transport

Madsen(1991) proposes that:

$$NF_d = \tau_b - \tau_{cr}, \text{ hence, } q_{SB} = Nu_{s\infty}\forall_s = u_{s\infty}\forall_s \frac{\tau_b - \tau_{cr}}{F_d} \tag{1.8}$$

where N is the number of grains moving per unit bottom area, F_d is the drag force acting on these moving grains, q_{SB} is bedload transport rate, $u_{s\infty}$ is terminal sediment grain velocity, $\forall_s$ is the sediment volume transport per unit width perpendicular to the transport direction, and τ_b, τ_{cr} are bottom and critical shear stresses, respectively. Figure-1.1 shows a simple free body diagram of a sediment grain resting on a sloped bed. Each force shown in the figure is as follows.

$$F_N = normal\ \ force \quad = (\rho_s - \rho)\forall_s g\cos\beta$$
$$f \quad = frictional\ \ force = F_N \tan\phi$$
$$F_g = gravity\ \ force \quad = (\rho_s - \rho)\forall_s g\sin\beta$$

where ρ_s and ρ are the sediment and fluid densities, β is beach slope angle and ϕ is the internal angle of friction, either static(ϕ_s) or kinetic(ϕ_k).

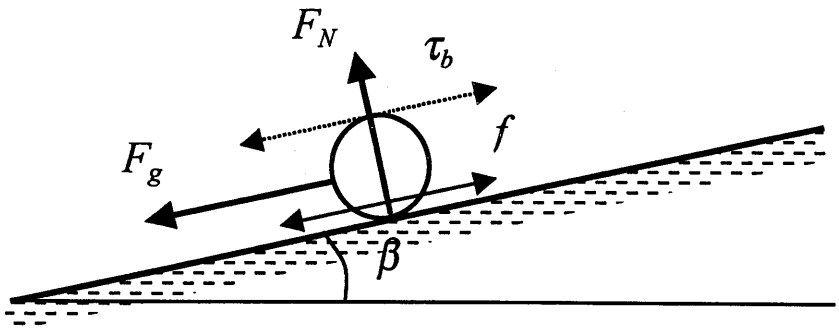

Figure-1.1 Sediment grain on slope

Taking all these forces into account, Madsen(1991) derived a bedload transport rate as,

$$q_{SB} = \begin{cases} \dfrac{\pm 8(|\tau_b| - \tau_{cr})}{(s-1)\rho g\cos\beta(\tan\phi_k \pm \tan\beta)}(u_* - \alpha u_{*cr}) & (|\tau_b| > \tau_{cr}) \\ 0 & (|\tau_b| < \tau_{cr}) \end{cases} \qquad (1.9)$$
$$\alpha = \sqrt{\frac{\tan\phi_k \pm \tan\beta}{\tan\phi_s \pm \tan\beta}}$$

where u_* and u_{*cr} are bottom and critical shear velocity. This formula consists of two equations, i.e., (+) sign signifies that the orbital velocity is in the shoreward direction (under the crest of the

wave) and a (-) sign in the seaward direction (under the trough of the wave). From the above equation, sediment transport rates in the down-slope direction become larger than those in the up-slope direction for the same value of $|\tau_b|$. This is because the gravity force acts in the down-slope direction while wave action creates a shear stress that acts in both shoreward and seaward directions. Therefore, this formula predicts that sediment transport on a slope would tend to move in the down-slope direction if fluid oscillations were completely symmetrical. This effect suggests the existence of an equilibrium beach slope, which is the value of the slope that cancels shoreward sediment transport induced by nonlinear waves.

(2) Suspended Transport

Inside the surf zone, estimation of suspended load is necessary not only because a strong undertow exists in order to compensate the shoreward mass transport but also because turbulence, which enhances the suspension of sediments, becomes stronger due to the effect of breaking waves. This is the reason why the characteristics of beach profiles inside the surf zone differ from those outside the surf zone.

Once the sediment concentration profile, C, and the undertow velocity profile, U, are found, the suspended load can be estimated by the following integration:

$$q_{SS} = \int_{Z_R}^{h} (CU)dz \tag{1.10}$$

where z is vertical upward axis with $z=0$ at the bottom, Z_R is defined as the point near the bed below which sediment transport is considered to be bedload and above which it is to be suspended load and h is mean water depth. Madsen and Meyer(1998) find C by solving the

following equation for the time-invariant concentration distribution with appropriate boundary conditions.

$$\frac{\partial}{\partial z}\left[(w_f C)+\left(\nu_s \frac{\partial C}{\partial z}\right)\right]=0 \tag{1.11}$$

where w_f is the fall velocity of the sediment and ν_s is the sediment diffusion coefficient, which is approximated by the turbulent eddy viscosity. According to Meyer and Madsen(1998), boundary conditions specified for this equation are defined as follows: (1) no sediment is transported through the surface and (2) a reference concentration, C_R is specified at a reference height above the bottom, Z_R. Z_R is defined as proportional to sediment diameter and C_R is theoretically considered to be proportional to the bedload transport rate. In this sense, therefore, this suspended load model also indicates that beach slope should cancel the sediment transport induced by waves and currents including undertow and, therefore, equilibrium beach profiles should exist.

(3) Wave and Current Model

Since the model is based on a specific conceptual mechanism of the sediment movement, we need more detailed wave and current information. As seen in equations (1.8) and (1.9), the model requires the information of the time variation of bottom shear stress, i.e., orbital bottom particle velocity, and vertical distribution of time-averaged undertow. Especially for orbital bottom particle velocity, asymmetric oscillations due to non-linear wave effects must be estimated appropriately in order to evaluate the shore-ward sediment transport which causes the formation of an equilibrium beach slope when balanced by the seaward slope effect.

Meyer and Madsen(1998) applied the Stokes and Cnoidal wave theory to evaluate wave

induced orbital velocity conditions. Since both theories have their limits of validity, they switched the wave model from Stokes Wave Theory to Cnoidal Wave Theory when the wave shoals and the Ursell Number exceeds 25. As for breaking waves, they simply defined that breaking wave height, H, should be proportional to the water depth, h, i.e., $H=0.8h$. They showed that their model gives reasonable equilibrium beach slope when both theories are theoretically applicable. However, they also showed that, in the shallow area such as inside the surf zone, their equilibrium beach slope becomes too steep because their shoreward sediment transport due to wave non-linearity is estimated too strong. This is caused by their overestimation of wave asymmetry.

In order to estimate more accurate equilibrium beach profiles, therefore, it is necessary to evaluate appropriate wave and current conditions including wave asymmetry profiles. For practical reasons, we therefore develop an improved wave and current model which is applicable as input to a traction-based sediment transport model.

1.3 Thesis Organization

The thesis is organized into three sections, Chapters 2, 3 and 4. In Chapter 2, we develop the wave models. For practical reasons, all models are constructed based on linear wave theory. First, the relationship between non-linear and an equivalent linear wave is discussed and a wave asymmetry model and bottom orbital velocity model is developed. Next, breaking wave dissipation models are developed. The applicability of these models is examined through comparison of their predictions with measured experimental data.

In Chapter 3, the undertow model is developed. Since the wave model is based on linear

wave theory, the undertow model is also developed based on linear wave theory. Particular attention is paid to the effect of surface rollers for which a new theoretical formulation is proposed. The applicability of the model is also tested through comparison with measured experimental data.

In Chapter 4, all the models are summarized and further extensions of the model are discussed.

Chapter 2

2 Wave Model

As discussed in the Introduction, wave asymmetry must be accurately evaluated to estimate sediment transport induced by waves. Since the wave asymmetry is caused by wave non-linearity, we need to accurately estimate the wave non-linearity.

Meyer and Madsen (1998) estimated the wave asymmetry using both Stokes and Cnoidal wave theories. They switched the wave theory from Stokes wave to Cnoidal wave when the wave shoals and the Ursell number exceeds 25 and computed wave conditions in each depth applying the conservation law of energy flux. It is already confirmed that this methodology gives accurate wave heights near the breaking point (e.g. Shuto, 1974). However, it is also known that Cnoidal wave theory breaks down in terms of its prediction of wave non-linearity in orbital velocity when the wave shoals and H/h, the ratio of wave height to mean water depth, becomes large. According to Horikawa (1985), the limitation of the Cnoidal wave theory is $H/h < 0.4$. This implies that we cannot apply Cnoidal wave theory near the breaking point where H/h is expected to be considerably larger than 0.4.

When the wave shoals on a slope, furthermore, it is known that the wave profiles become saw-tooth type in shape due to the effect of the bottom slope. Cnoidal wave theory cannot evaluate this feature because the theory assumes constant depth condition. Meyer and Madsen (1998) also showed that their wave asymmetry was too strong, especially inside the surf-zone, and resulted in too steep an equilibrium beach profile in the surf-zone.

Based on Cnoidal and Stokes wave theory, Isobe and Horikawa (1981) proposed semi-empirical formulae to compute some parameters, which represent wave asymmetry and skewness. They also showed that their parameters, based on Cnoidal and Stokes wave theories, gave too strong wave asymmetry, especially when the water depth is considerably smaller than the wavelength. Although they modified their approximate formulae to coincide with experimental data, their model is not a function of the bottom slope.

To take both wave non-linearity and the effect of the bottom slope into account, a numerical wave model is useful. Recently, a number of numerical non-linear wave models have been proposed and the applicability of these models is also confirmed. However, numerical models still have practical limitations in terms of computation time and boundary problems.

In this study, therefore, we apply linear wave theory to evaluate local wave conditions and propose a semi-theoretical methodology to determine the wave asymmetry caused by wave non-linearity for waves climbing a slope.

2.1 Non-Linear Wave Model

As discussed before, our goal is to estimate the asymmetrical profile of the bottom orbital velocity from the equivalent linear wave conditions. In order to evaluate the saw-tooth type

profiles as waves shoal, we also need to account for the effect of the bottom slope. To achieve this goal, we first perform a numerical experiment to evaluate local wave conditions and bottom velocity characteristics. Throughout this experiment, the relationship between computed wave height and equivalent linear wave height is also examined, which will be used to develop our breaking wave dissipation model.

2.1.1 Outline of the Model

Similar to Isobe and Horikawa's (1981) model, we evaluate the following five parameters, (1) H/H_*, (2) T_{c1}/T, (3) T_{c2}/T, (4) u_c/U_b and (5) U_b/U_{b*}. Here, H is computed wave height, H_* is the equivalent linear wave height, T_{c1} and T_{c2} are different wave-crest periods and T is a wave period. Moreover, u_c is maximum bottom orbital velocity, U_b is total "height" of bottom orbital velocity, which is the difference between maximum and minimum bottom orbital velocity, and U_{b*} is the equivalent linear total height of the bottom orbital velocity. The definition of these parameters is shown in Figure-2.1. Here, different definition of T_c(i.e., T_{c1} and T_{c2}) are necessary to improve the applicability of our asymmetry model over that of Isobe and Horikawa (1981), who used a single value to express asymmetry.

As discussed previously, all our parameters should be functions of local wave height, wave period and bottom slope. For convenience, we use the following three dimensionless variables to determine our parameters. (A) Deep water wave steepness, H_0/L_0, which is converted from the local wave and depth conditions, (B) the ratio of still water depth to deep water wave length, h/L_0, and (C) bottom slope, $\tan\beta$.

A numerical experiment is performed to determine the selected parameters as functions of

H_0/L_0, h/L_0 and tanβ. From the numerical result, we develop approximate formulae to evaluate these wave parameters.

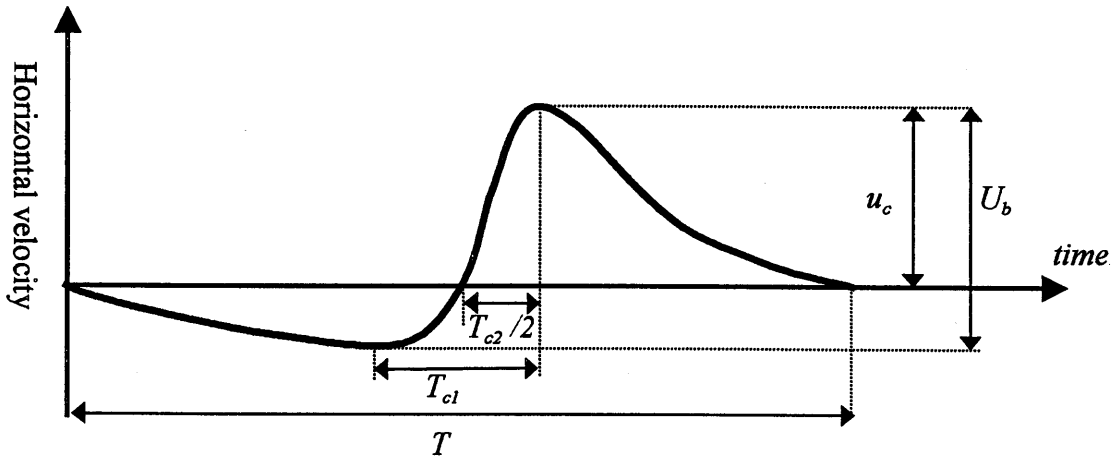

Figure-2.1 Asymmetry parameters of the wave orbital velocity

2.1.2 Numerical Experiment

(1) Governing Equations

For the numerical experiment, we apply Nwogu (1993)'s modified Boussinesq equations, which are as follows.

$$\eta_t = -\{(h+\eta)u_\alpha\}_x - \{a_1 h^3 u_{\alpha xx} + a_2 h^2 (hu_\alpha)_{xx}\}_x \tag{2.1}$$

$$\{u_\alpha + b_1 h^2 u_{\alpha xx} + b_2 h(hu_\alpha)_{xx}\}_t = -g\eta_x - u_\alpha u_{\alpha x} \tag{2.2}$$

$$a_1 = \frac{1}{2}\left(\frac{z_\alpha}{h}\right)^2 - \frac{1}{6},\ a_2 = \left(\frac{z_\alpha}{h}\right) + \frac{1}{2},\ b_1 = \frac{1}{2}\left(\frac{z_\alpha}{h}\right)^2,\ b_2 = \frac{z_\alpha}{h} \tag{2.3}$$

Here, z_α is an arbitrary point on the z-axis between bottom and still water level where the z-axis is

upward with $z=0$ at the still water level. Nwogu (1993) showed that if one takes $z_\alpha=-0.533h$, his Boussinesq equations give the optimum dispersion relationship that is close to that of small amplitude linear wave theory. In our application of this numerical model, therefore, we take $z_\alpha=-0.533h$. Moreover, u_α is the horizontal particle velocity at $z=z_\alpha$. Subscripts x and t denote partial differentiation where t is time and x is horizontal axis taken positive in the shoreward direction. Using z_α and u_α, the horizontal particle velocity at an arbitrary point, $u(z)$, is determined as

$$u(z)=u_\alpha+\frac{1}{2}\left(z_\alpha^2-z^2\right)\ u_{\alpha xx}+\left(z_\alpha-z\right)\left(hu_\alpha\right)_{xx} \tag{2.4}$$

Detailed methodologies of space-discretization and time derivation are discussed in Appendix A.

(2) Conditions

Computation was performed on variable uniform slopes for various deep-water wave steepnesses, H_0/L_0. Table-2.1 shows all the cases of the computation. Here, H_0/L_0 for each case was estimated directly from the numerical results of wave conditions near the offshore boundary. Methodology of this estimation is discussed later. Incident wave conditions, i.e., time variation of free surface profile and current profile, were obtained by 5th order Stokes Wave Theory (Isobe, 1978) or Stream Function Theory with 19 terms (Dean, 1965).

The geometrical conditions for the computations are shown in Figure-2.2. In order to introduce stable and accurate incident waves into the system, the constant depth region was set at the offshore boundary.

Table-2.1 Numerical experiment cases

SLOPE	CASE	H_0/L_0	Offshore water depth(m)	Incident wave height(m)	Incident wave theory
1/10	A1	0.001	10.0	0.093	STK5th
	A2	0.002	10.0	0.186	SFM19
	A3	0.005	10.0	0.466	SFM19
	A4	0.010	10.0	0.931	SFM19
	A5	0.020	15.0	1.824	SFM19
	A6	0.050	20.0	4.583	STK5th
1/20	B1	0.001	10.0	0.093	STK5th
	B2	0.002	10.0	0.186	SFM19
	B3	0.005	10.0	0.466	SFM19
	B4	0.010	10.0	0.931	SFM19
	B5	0.020	15.0	1.824	SFM19
	B6	0.050	20.0	4.583	STK5th
1/35	C1	0.001	10.0	0.093	STK5th
	C2	0.002	10.0	0.186	SFM19
	C3	0.005	10.0	0.466	SFM19
	C4	0.010	10.0	0.931	SFM19
	C5	0.020	15.0	1.824	SFM19
	C6	0.050	20.0	4.583	STK5th
1/50	D1	0.001	10.0	0.093	STK5th
	D2	0.002	10.0	0.186	SFM19
	D3	0.005	10.0	0.466	SFM19
	D4	0.010	10.0	0.931	SFM19
	D5	0.020	15.0	1.824	SFM19
	D6	0.050	20.0	4.583	STK5th
1/100	E1	0.001	10.0	0.093	STK5th
	E2	0.002	10.0	0.186	SFM19
	E3	0.005	10.0	0.466	SFM19
	E4	0.010	10.0	0.931	SFM19
	E5	0.020	15.0	1.824	SFM19
	E6	0.050	20.0	4.583	STK5th

*STK5: Stokes 5th order wave theory / SFM19: Stream function of 19th order

The length of this region is $2.5L_{in}$, where L_{in} is the incident wave length. The constant offshore depth, h_{in}, which is shown in Table-2.1 for each case, was selected so as to keep the Ursell number less than 10 as well as h_{in}/L_{in} less than 0.2. This condition allows us to apply both Boussinesq equation and Stokes wave theory. Near the onshore boundary, constant depth is again assumed and a sponge layer was introduced in order to absorb the waves and avoid reflected waves. The constant depth at the onshore boundary was chosen about 50% larger than the wave breaking depth, which is determined from incident wave conditions by Goda's (1970) breaking wave criteria. The starting point of the sponge layer was adjusted as shallow as possible for the numerical computation keeps stable. Although this depth varies by each case, it was always deeper than $H/0.6$, which slightly exceeds the criteria of the valid use of the Boussinesq equations. As for the sponge-layer conditions for the numerical computation, we applied the model proposed by Cruz et al. (1993). Further details are given in Appendix A.

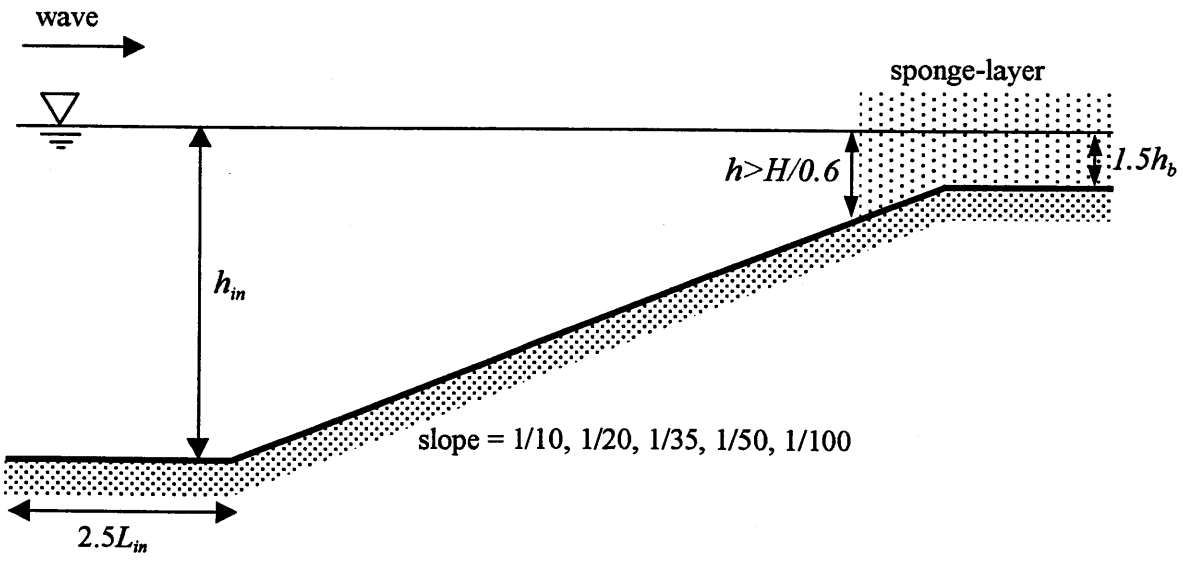

Figure-2.2 Topography conditions for the computation

Computation was conducted for sufficiently long periods so that quasi-steady waves were achieved everywhere. During the computations, all variables such as H, U_b, u_c, T_{c1} and T_{c2} are extracted at each horizontal grid from the beginning point of the uniform slope to the sponge-layer.

(3) Estimation of H_0/L_0

Since all our wave parameters are determined from the equivalent linear wave condition, we need to estimate the exact equivalent linear wave conditions for each numerical computation. Assuming that energy flux should be conserved between this numerical model and linear wave theory, we estimate linear wave conditions from the results of the numerical experiments. Since we have no energy dissipation term except for the sponge-layer and negligible reflection is expected, we simply estimate energy flux near the offshore boundary in the constant depth region and assume that energy flux should be conserved for all other locations except inside the sponge-layer region. In the numerical experiment, wave energy flux in the constant depth region, E_f, is determined as

$$E_f = \frac{\rho C}{T}\int_0^T dt \int_{-h}^{\eta} u^2 dz \tag{2.5}$$

where C is wave phase velocity, ρ is fluid density, T is wave period, u is horizontal particle velocity, h is still water depth, η is the free surface displacement and z is the vertical axis positive upward with $z=0$ at the still water level. Wave phase velocity is determined by $C=L/T$, where wavelength, L, is directly estimated from the numerical results by the zero-up-crossing method. Integration over depth in (2.5) can be done analytically using (2.4).

$$\begin{aligned}\int_{-h}^{\eta} u^2 dz &= \int_{-h}^{\eta} dz\left\{A^2 - 2z(hu_\alpha)_{xx}A + z^2\left[\left((hu_\alpha)_{xx}\right)^2 - u_{\alpha xx}A\right] + z^3 u_{\alpha xx}(hu_\alpha)_{xx} + \frac{1}{4}z^4(u_{\alpha xx})^2\right\} \\ &= \left[A^2 z - z^2(hu_\alpha)_{xx}A + \frac{1}{3}z^3\left[\left((hu_\alpha)_{xx}\right)^2 - u_{\alpha xx}A\right] + \frac{1}{4}z^4 u_{\alpha xx}(hu_\alpha)_{xx} + \frac{1}{20}z^5(u_{\alpha xx})^2\right]_{-h}^{\eta} \\ &= A^2(\eta + h) - (hu_\alpha)_{xx}A(\eta^2 - h^2) + \frac{1}{3}\left[\left((hu_\alpha)_{xx}\right)^2 - u_{\alpha xx}A\right](\eta^3 + h^3) \\ &+ \frac{1}{4}u_{\alpha xx}(hu_\alpha)_{xx}(\eta^4 - h^4) + \frac{1}{20}(u_{\alpha xx})^2(\eta^5 + h^5)\end{aligned} \tag{2.6}$$

where

$$A = u_\alpha + \frac{1}{2}z_\alpha^2 u_{\alpha xx} + z_\alpha (hu_\alpha)_{xx} \tag{2.7}$$

Evaluating (2.5) from (2.6), we can estimate the equivalent linear wave condition. The deep water wave height, H_0, is therefore computed from obtained E_f by

$$E_f = \frac{1}{16}\rho g H_0^2 \frac{gT}{2\pi} \quad \Rightarrow \quad H_0 = \sqrt{\frac{32\pi E_f}{\rho g^2 T}} \tag{2.8}$$

Through the computation, it was confirmed that actual wave height introduced at the offshore boundary agreed well with the equivalent linear wave height at the offshore boundary estimated by linear wave theory from the deep water wave height obtained by (2.8). This is because the Ursell number is so small that non-linearity is essentially negligible from deep water to the depth at the offshore boundary.

(4) Results

Figures 2.3 and 2.4 show H/H_*, the ratio of computed wave height to equivalent linear wave height as a function of h/L_0 and H_0/L_0 on each bottom slope. The plotted curves estimated from the computation are terminated at the beginning point of the sponge layer, which is

supposed to be close to the limit of validation of our numerical model. For comparison, Figure-2.4 also shows the variation of H/H_* for constant depth conditions computed by 1st order Cnoidal Wave Theory (Isobe, 1985). Equivalent linear wave height, H_*, is estimated from deep-water wave steepness by linear wave theory. Since little reflection is expected in this numerical experiment, we assume that the linear wave heights should be identical to the equivalent linear wave heights for each local non-linear wave conditions. In these figures, the dotted lines represent approximation curves to be discussed later. From the figure, it is found that the effect of the slope becomes conspicuous when h/L_0 is small. It is also found that H/H_* becomes smaller when the bottom slope is steeper.

Similarly, Figures 2.5 to 2.11 show T_{c1}/T, T_{c2}/T, u_c/U_b and U/U_{b*} as a function of h/L_0 and H_0/L_0 on each bottom slope. From these figures, we can see that T_{c1}/T, T_{c2}/T and u_c/U_b become closer to 0.5 and U_b/U_{b*} become closer to unity when H_0/L_0 is smaller or h/L_0 is larger, i.e., wave non-linearity becomes weaker. In contrast, it is observed that T_{c1}/T and T_{c2}/T become smaller and u_c/U_b becomes larger when the wave non-linearity is expected to be stronger, i.e., H_0/L_0 is larger or h/L_0 is smaller.

It is also seen that the steeper bottom slope tends to make T_{c1}/T, T_{c2}/T and u_c/U closer to 0.5. For example, the value of u_c/U when $H_0/L_0=0.01$ and $h/L_0=0.01$ decreases from 0.62 to 0.52 when the bottom slope increases from 0.01 to 0.1 (see Figure-2.7 and 2.11). Furthermore, it is interesting to note that the variation of U/U_* is much less than that of H/H_*. This observation implies that we can estimate bottom orbital velocity "height" within a relatively small error only by linear wave theory from the equivalent linear wave heights.

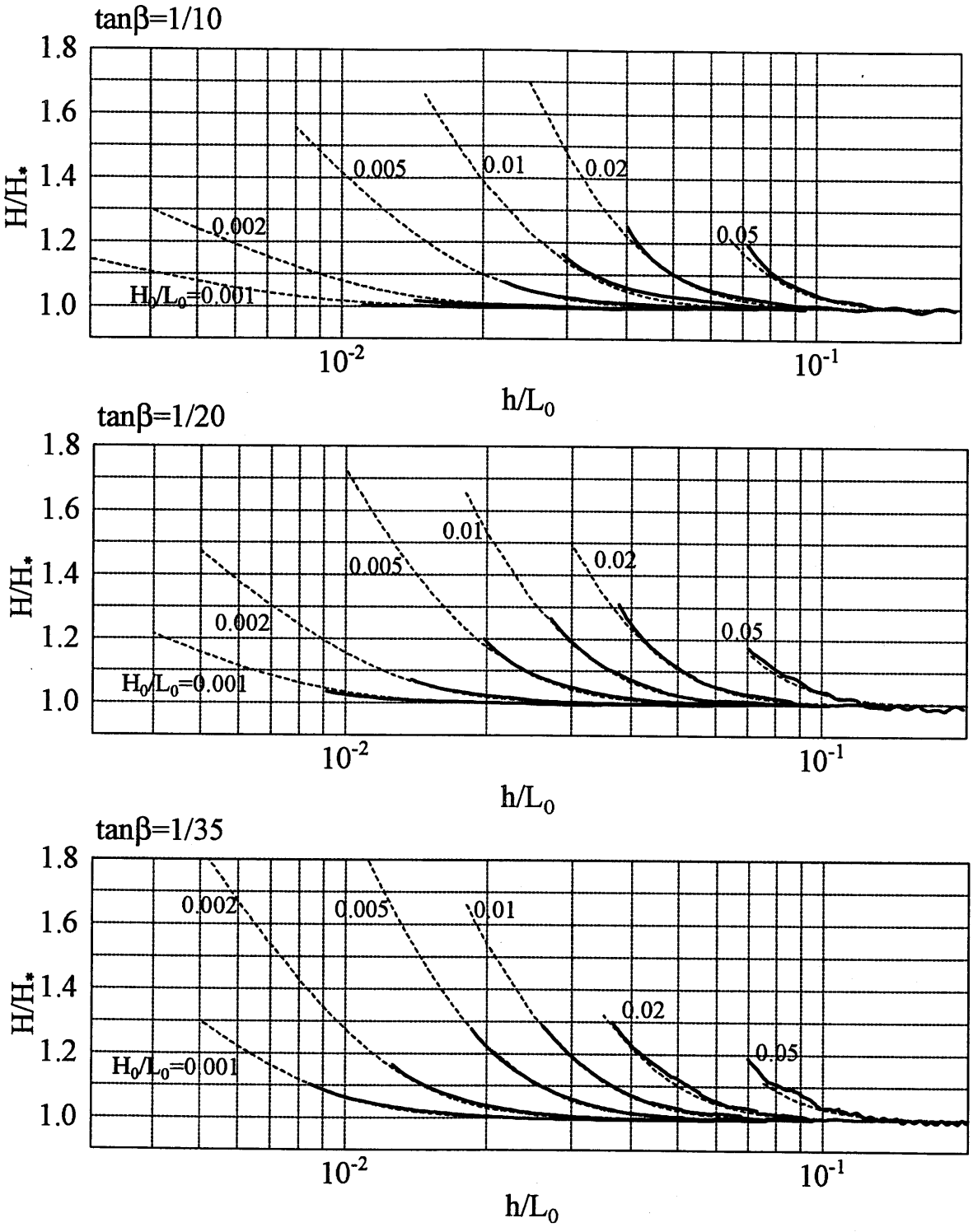

Figure-2.3 H_*/H vs. h/L_0 (tanβ=1/10, 1/20, 1/35)

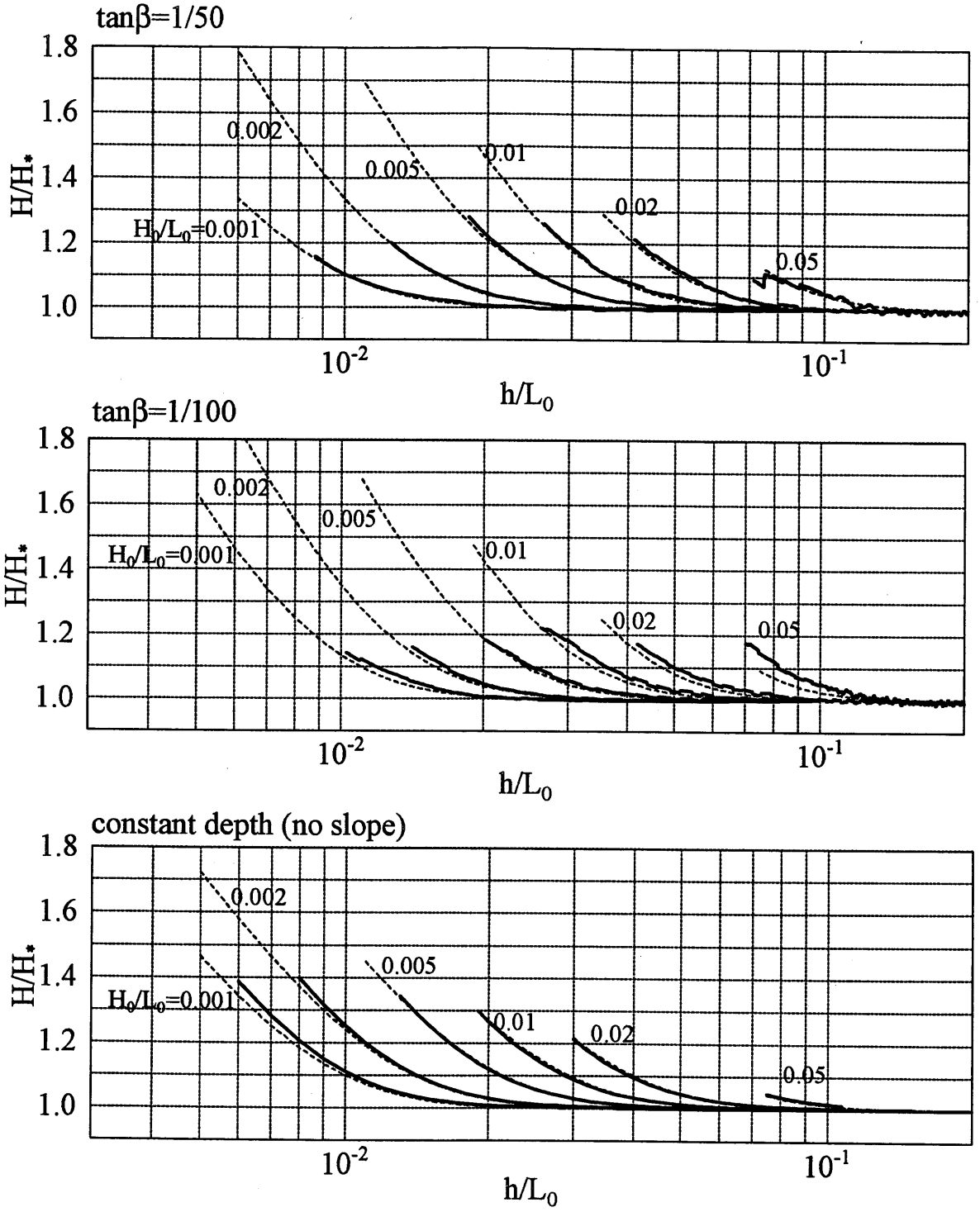

Figure-2.4 H/H_* vs. h/L_0 (tanβ=1/50, 1/100 and no slope)

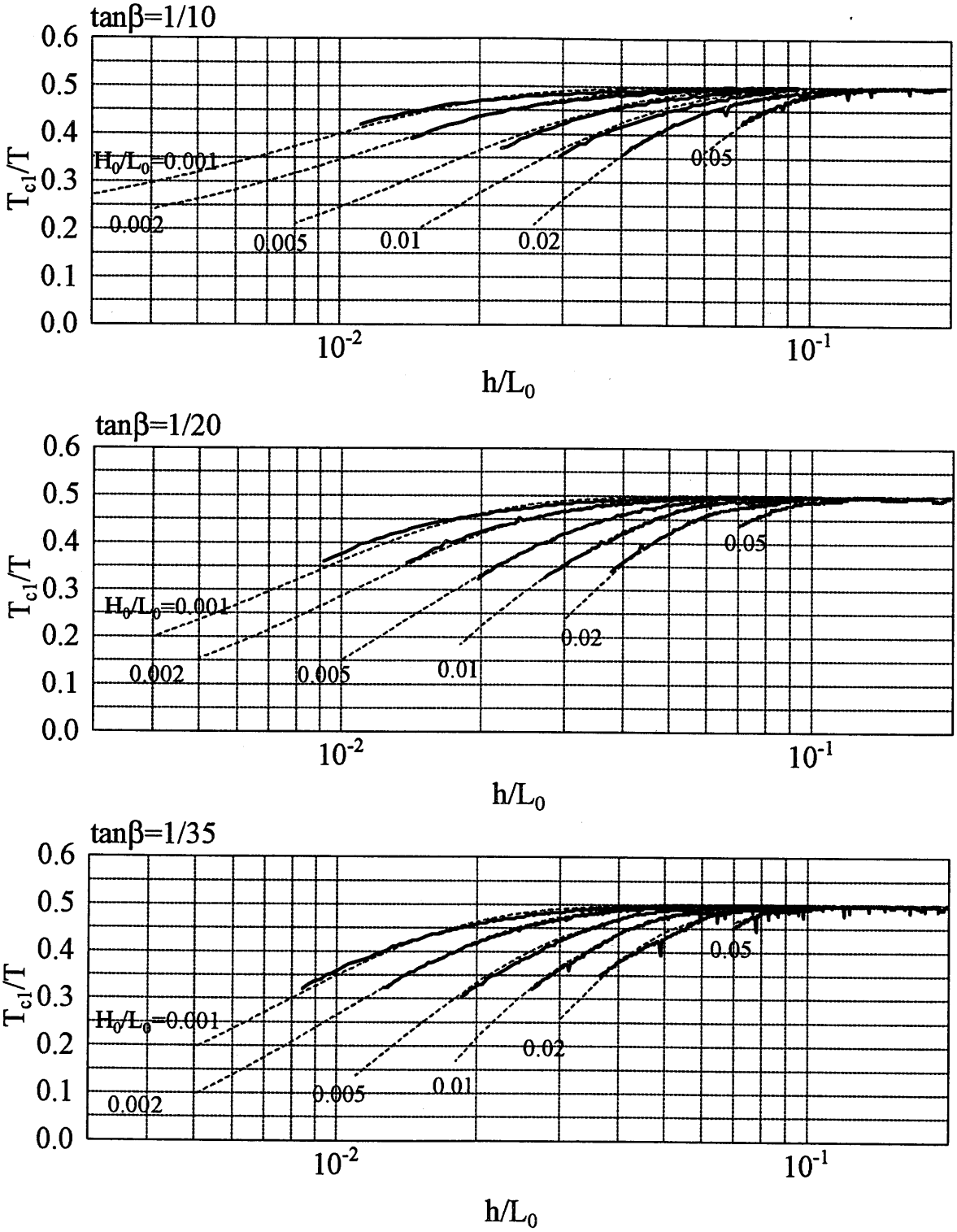

Figure-2.5 T_{cl}/T vs. h/L_0 (tanβ=1/10, 1/20/ 1/35)

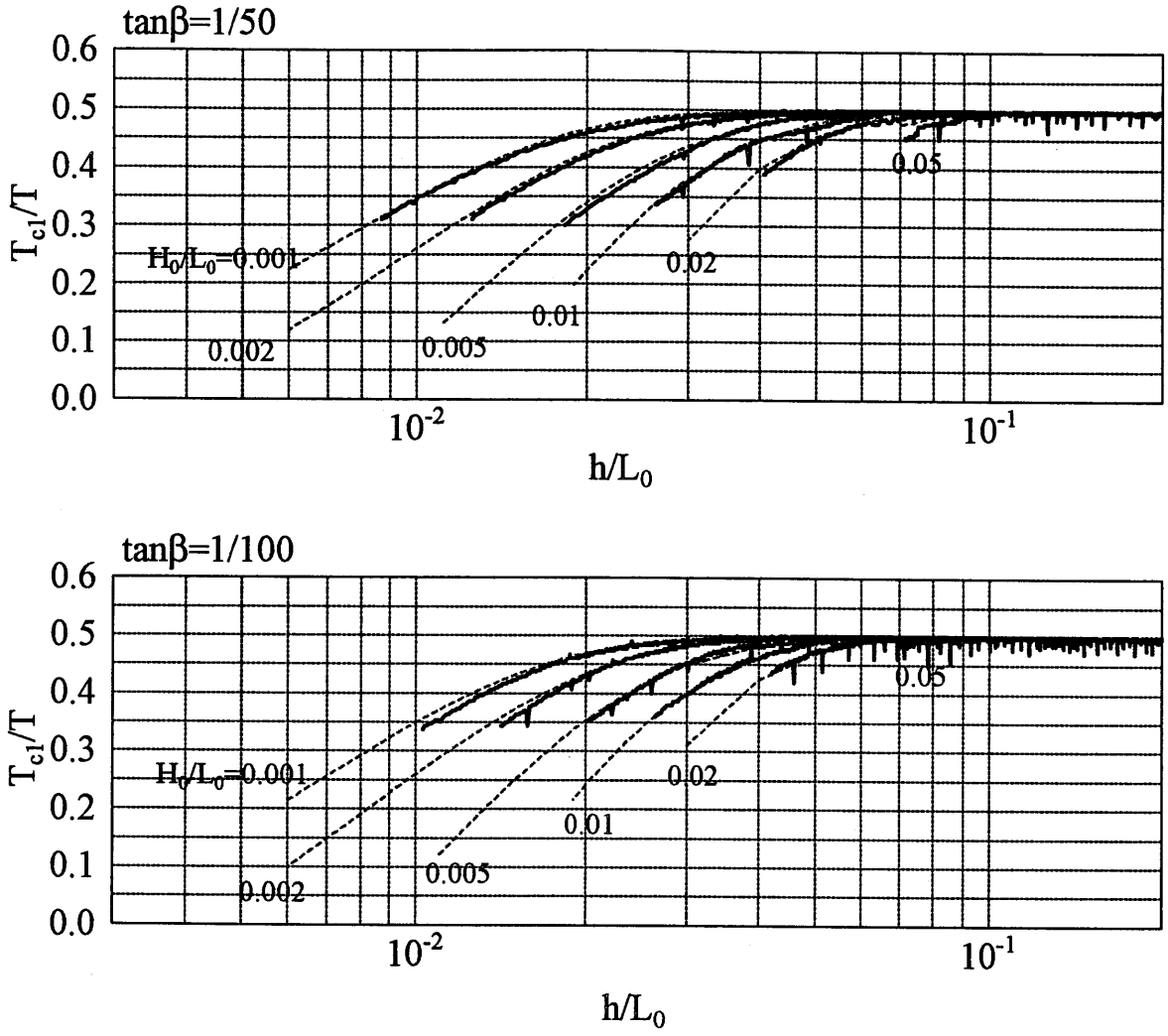

Figure-2.6 T_{c1}/T vs. h/L_0 (tanβ=1/50 and 1/100)

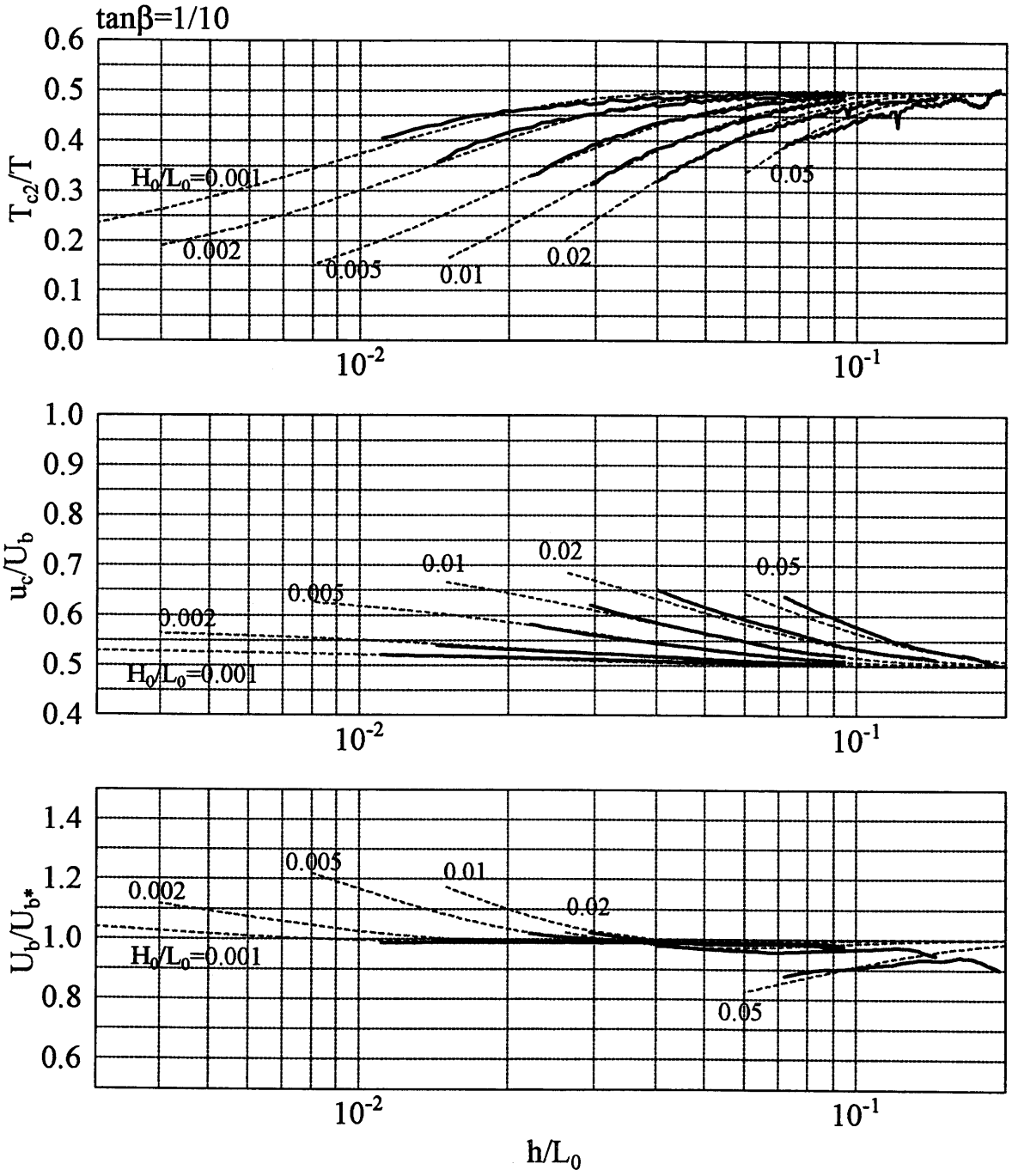

Figure-2.7 T_{c2}/T, u_c/U_b and U_b/U_{b*} vs. h/L_0 (tanβ=1/10)

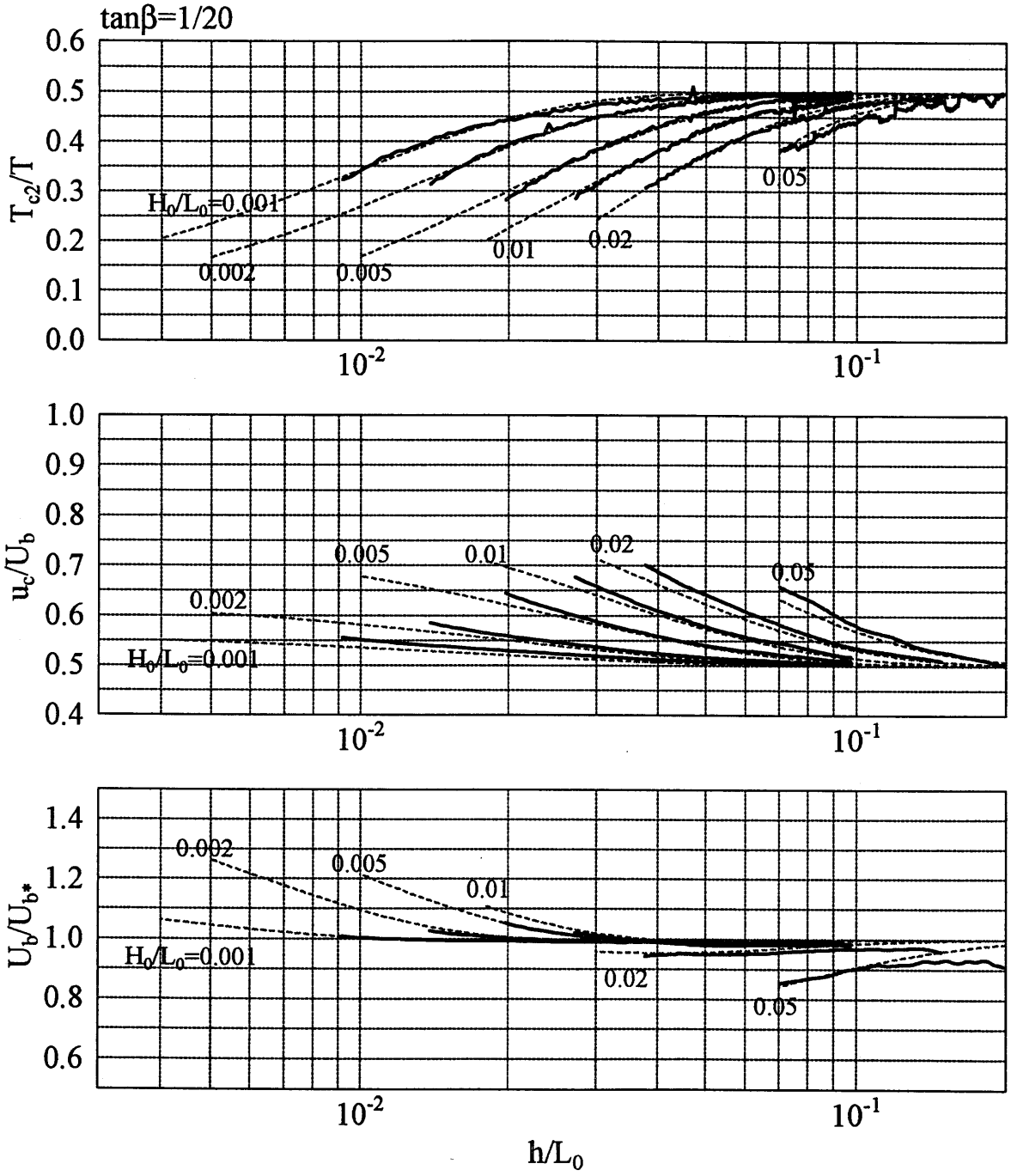

Figure-2.8 T_{c2}/T, u_c/U_b and U_b/U_{b*} vs. h/L_0 (tanβ=1/20)

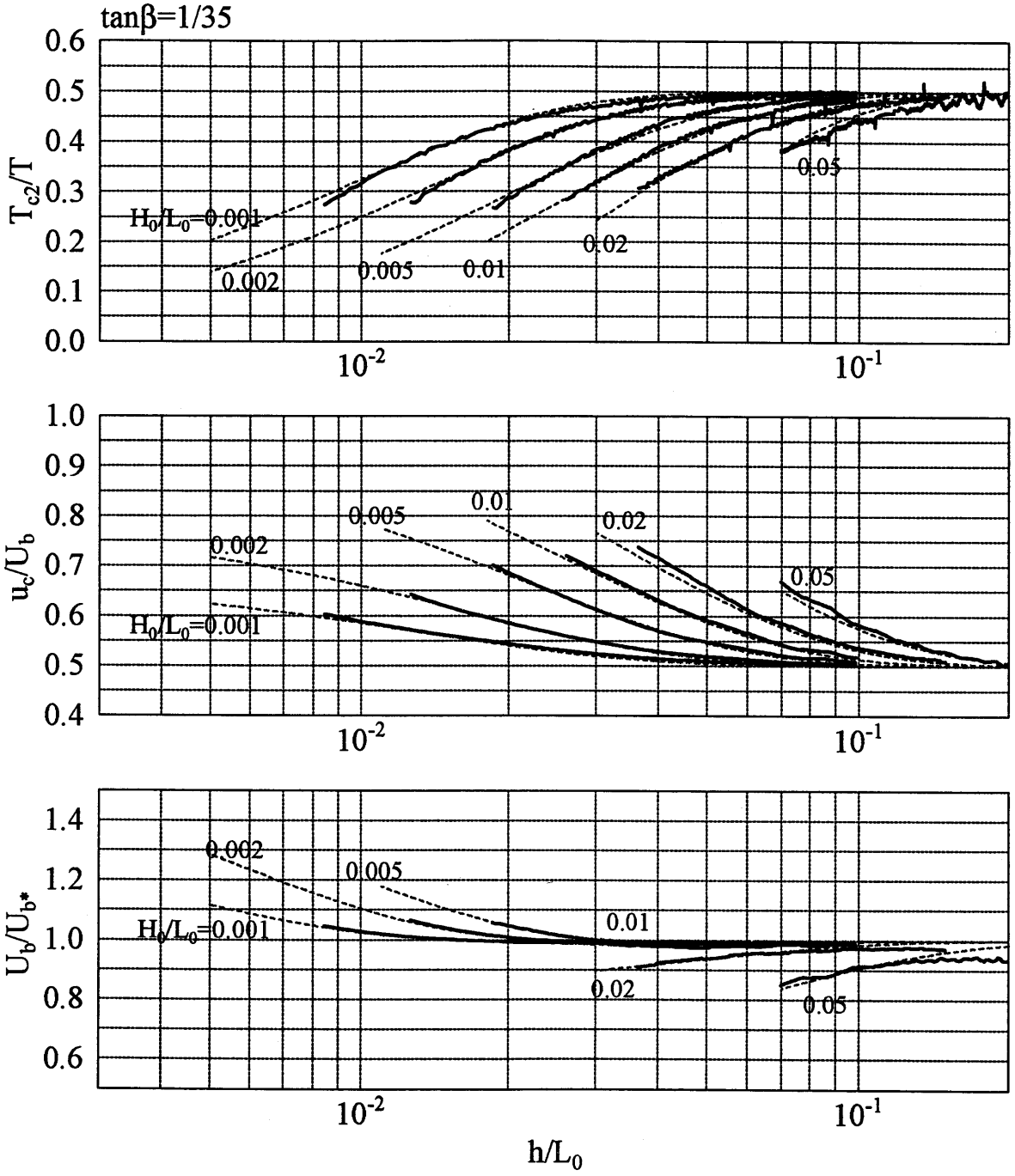

Figure-2.9 T_{c2}/T, u_c/U_b and U_b/U_{b*} vs. h/L_0 (tanβ=1/35)

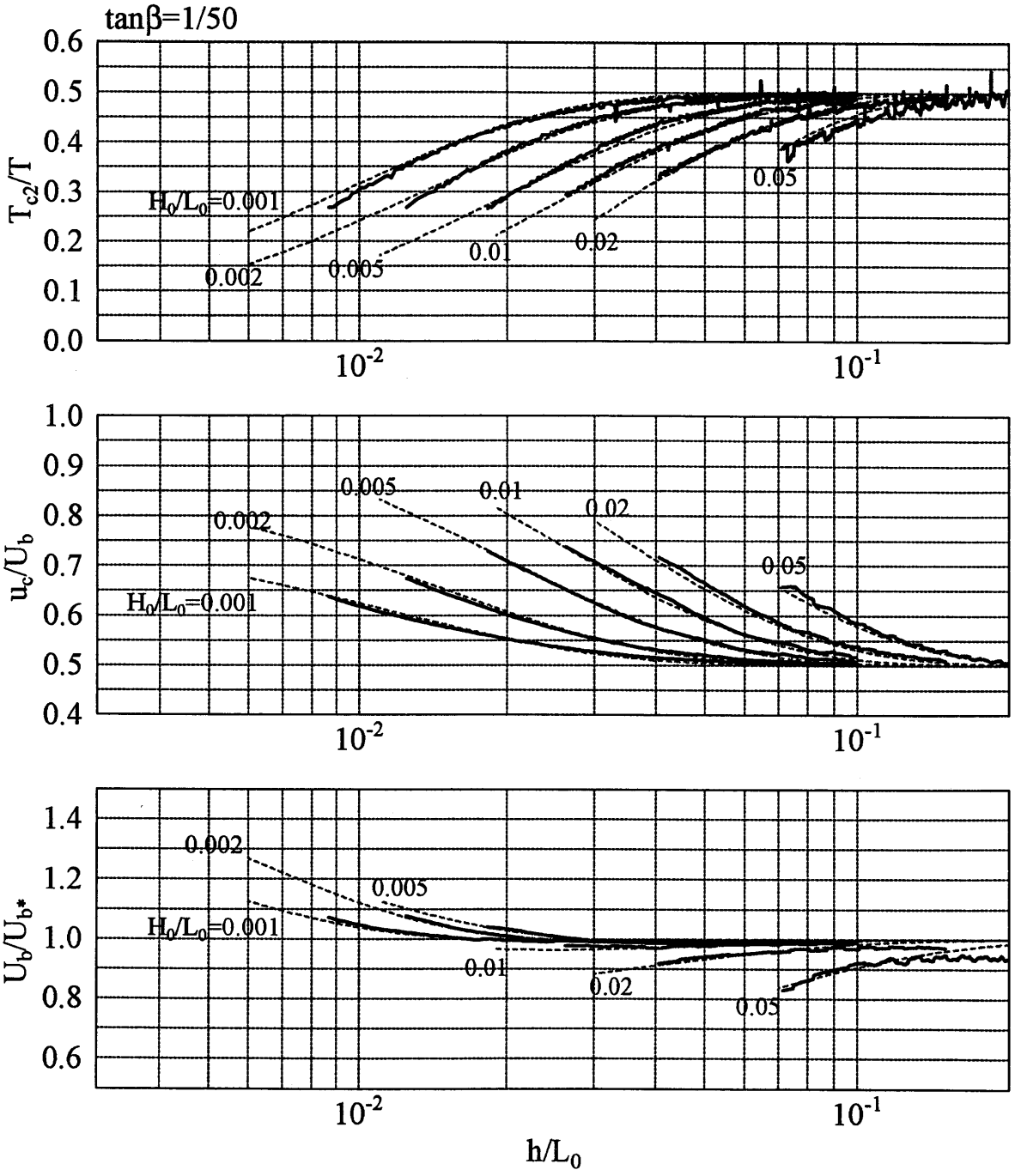

Figure-2.10 T_{c2}/T, u_c/U_b and U_b/U_{b*} vs. h/L_0 (tanβ=1/50)

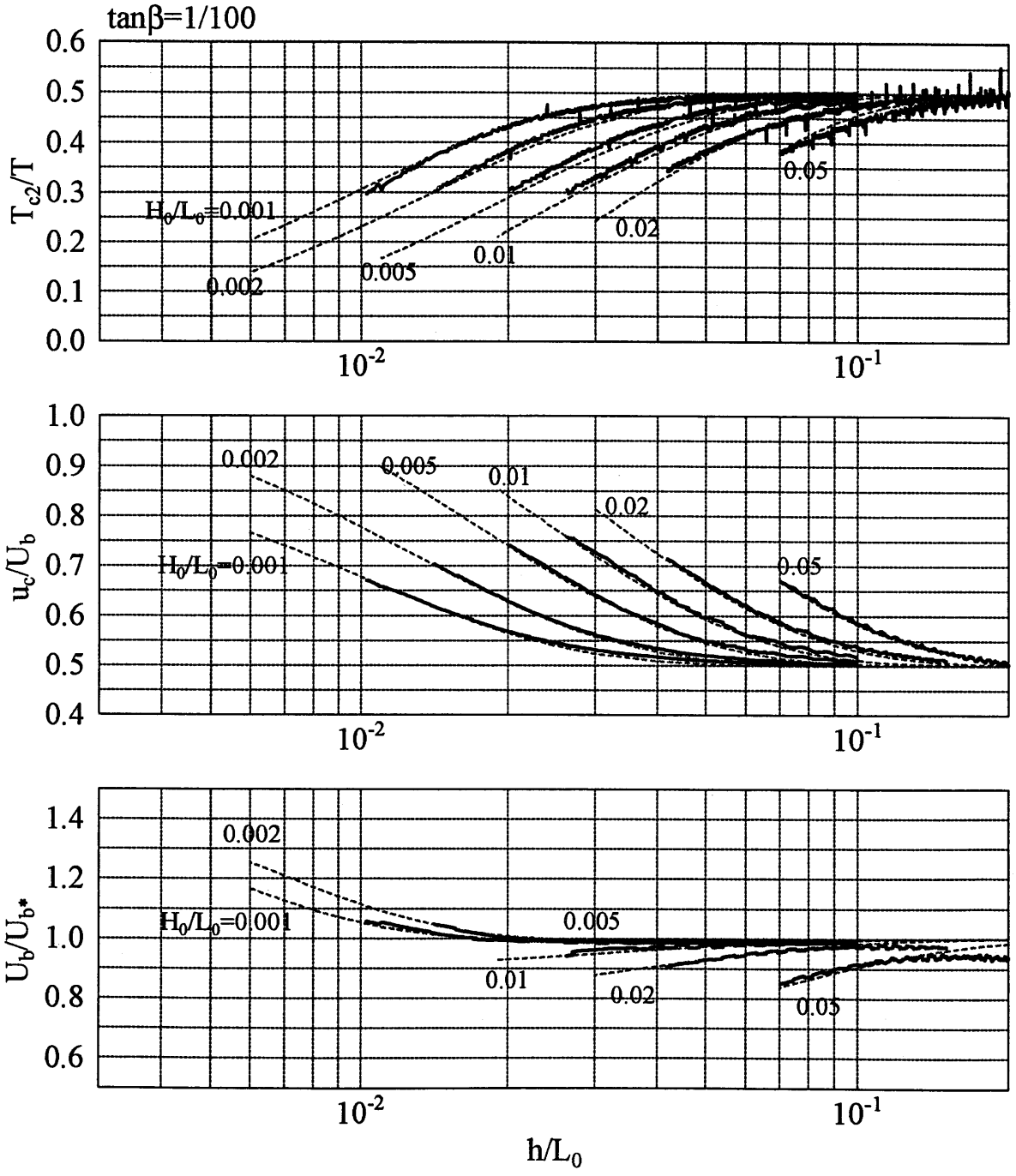

Figure-2.11 T_{c2}/T, u_c/U_b and U_b/U_{b*} vs. h/L_0 (tanβ=1/100)

2.1.3 Wave Shoaling

From the results of the numerical computation, approximation curves for H/H_* are determined to be

$$H/H_* = 1.0 + d_1 \exp[-d_2(h/L_0)]$$

$$\left.\begin{aligned} d_1 &= (2.2 + 2\tanh(55\tan\beta))\tanh\left[\left(1.6(\tan\beta)^{-1.5} + 25\right)(H_0/L_0)\right] \\ &\quad + 30(\tan\beta)^{0.1}(H_0/L_0) \\ d_2 &= 9.5(H_0/L_0)^{-0.5} + 10 \end{aligned}\right\} \quad when\ \tan\beta > 0 \qquad (2.9)$$

$$\left.\begin{aligned} d_1 &= 2.2 \\ d_2 &= 9.5(H_0/L_0)^{-0.5} + 10 \end{aligned}\right\} \quad when\ \tan\beta \le 0$$

Figures 2.3 and 2.4 show the approximation curves estimated by (2.9) as dotted lines. Approximation curves are extended from the end of the numerical computation to the breaking point determined by Goda's (1970) breaking criteria. From arbitrary linear wave conditions, we can determine the deepwater wave height and wavelength, and we can then estimate actual non-linear wave height from the approximation formula (2.9). If the bottom slope is negative, i.e., depth is increasing in the shoreward direction, we apply the no-slope condition.

2.1.4 Wave Asymmetry Parameters

Similarly, from the result of the numerical computation, we determined the following approximate formulae for three wave asymmetry parameters and the orbital velocities as

functions of H_0/L_0, h/L_0 and $\tan\beta$.

$$
\begin{aligned}
T_{c1}/T &= 0.5 - a_1 \exp[-a_2(h/L_0)] \\
a_1 &= 33 + 110\exp[-30\tan\beta](H_0/L_0) + 0.69\exp[-8.7\tan\beta] \\
a_2 &= 40 + 60\exp[-30\tan\beta] + 0.3(H_0/L_0)^{-0.8}
\end{aligned}
\tag{2.10}
$$

$$
\begin{aligned}
T_{c2}/T &= 0.5 - a_1 \exp[-a_2(h/L_0)] \\
a_1 &= 0.5 + 14(H_0/L_0) + (0.1 - 0.4\tanh(10\tan\beta))\exp[-300(H_0/L_0)] \\
a_2 &= 30 + 0.3(H_0/L_0)^{-0.8}
\end{aligned}
\tag{2.11}
$$

$$
\begin{aligned}
u_c/U_b &= 0.5 + b_1 \exp[-b_2(h/L_0)] \\
b_1 &= \exp[-\exp\{-1.3 - 3.6\exp(-30\tan\beta)\}] \\
&\quad \times \exp\{(-0.3 - 0.25\exp(-10\tan\beta)) \cdot \ln(H_0/L_0)\} \\
b_2 &= \exp[2.4 - 0.5\exp\{-45\tan\beta\}] \cdot (H_0/L_0)^{-(0.18 + 0.24\exp\{-25\tan\beta\})}
\end{aligned}
\tag{2.12}
$$

$$
\begin{aligned}
U_b/U_{b*} &= 1.0 - c_1 \exp[-c_2(h/L_0)] + c_3 \exp[-c_4(h/L_0)] \\
c_1 &= 5.4(H_0/L_0)^{0.75} \\
c_2 &= 80(H_0/L_0)^{-0.1} - 90 \\
c_3 &= 49\{(95 + 1100\exp\{-60\tan\beta\})(H_0/L_0)\}^2 \\
&\quad \times \exp\left[-4\sqrt{(95 + 1100\exp\{-60\tan\beta\})(H_0/L_0)}\right] \\
c_4 &= -8 \cdot (H_0/L_0)^{-0.5}
\end{aligned}
\tag{2.13}
$$

These approximation curves are shown in the Figures 2.5 to 2.11 by the dotted lines and are extended to the breaking point determined by Goda's (1970) breaking criteria. Within the no breaking range, these formulae approximate the numerical results sufficiently, which will be shown later.

2.1.5 Improved Approximation Model for Bottom Orbital Velocity Profile

Utilizing the asymmetry parameters obtained in the Section 2.1.4, approximate bottom orbital velocity profiles can be modeled as a combination of four sinusoidal waves. Figure-2.12 illustrates the approximated velocity profile. Each of the four sinusoidal curves is numbered. The model outline is as follows.

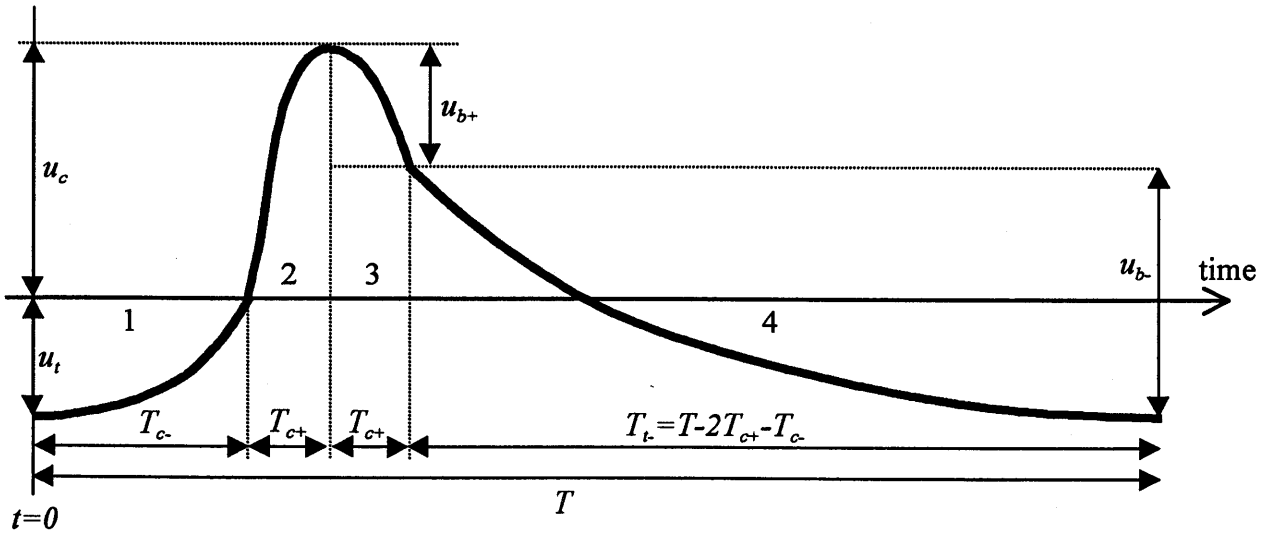

Figure-2.12 Approximation of the bottom orbital velocity profile

In the figure, each sinusoidal curves is expressed as

$$
\begin{aligned}
&1.\ u = -u_t \cos\left(\frac{\pi}{2T_{c-}}t\right) && (0 \le t \le T_{c-}) \\
&2.\ u = u_c \sin\left(\frac{\pi}{2T_{c+}}(t - T_{c-})\right) && (T_{c-} \le t \le T_{c+}) \\
&3.\ u = u_{b+} \cos\left(\frac{\pi}{2T_{c+}}(t - T_{c-} - T_{c+})\right) + u_c - u_{b+} && (T_{c-} + T_{c+} \le t \le T_{c-} + 2T_{c+}) \\
&4.\ u = -u_{b-} \sin\left(\frac{\pi}{2T_{c+}}(t - T_{c-} - 2T_{c+})\right) + u_c - u_{b+} && (T_{c-} + 2T_{c+} \le t \le T)
\end{aligned}
\tag{2.14}
$$

Here, u_t, T_{t-}, T_{c-} and T_{c+} are estimated from the asymmetry parameters from (2.10) to (2.10) as

$$
\begin{aligned}
u_t &= U_b - u_c \qquad T_{t-} = T - T_{c1} - 0.5T_{c2} \\
T_{c+} &= 0.5T_{c2} \qquad T_{c-} = T_{c1} - 0.5T_{c2}
\end{aligned}
\tag{2.15}
$$

Now unknown parameters are u_{b+} and u_{b-}. Since the sum of u_{b+} and u_{b-} should be identical with total "height" of the orbital velocity,

$$
u_{b+} + u_{b-} = u_c + u_t = U_b \tag{2.16}
$$

From the condition that average velocity must be zero,

$$
\begin{aligned}
&\int_0^{T_{c-}} u_1 dt + \int_0^{T_{c+}} u_2 dt + \int_0^{T_{c+}} u_3 dt + \int_0^{T_{t-}} u_4 dt = 0 \\
&\therefore -u_t T_{c-} + u_c T_{c+} + \frac{\pi}{2}(u_c - u_{b+})(T_{c+} + T_{t-}) + u_{b+} T_{c+} - u_{b-} T_{t-} = 0
\end{aligned}
\tag{2.17}
$$

From (2.16) and (2.17), u_{b+} and u_{b-} are determined as

$$
\begin{aligned}
u_{b+} &= u_c\left(1 - \frac{T_{c2}}{(1-\pi/2)(T - T_{c1})}\right) + \frac{u_t}{1-\pi/2} \\
u_{b-} &= \frac{u_c T_{c2}}{(1-\pi/2)(T - T_{c1})} - \frac{u_t \pi/2}{1-\pi/2}
\end{aligned}
\tag{2.18}
$$

2.1.6 Model Application

The applicability of our approximation formulae was examined through the comparison with experimental data presented by Cox et al. (1995) and Cnoidal Wave Theory.

(1) Comparison with Cox et al. (1995) experimental data

Cox et al., (1995) measured the time variance of the free surface and current velocity at multiple depth points for the regular wave propagating on the uniform slope of 1:35. Detailed condition of the experiment is to be presented later. From their data, wave height, mean water depth, wave period and bottom orbital velocity profile are specified. Since measured wave height is including wave non-linear effect, we first estimate the equivalent linear wave heights from measured data by (2.9). The estimation must be done numerically. The methodology of this computation is summarized as follows.

1. For an initial value, take equivalent linear wave height identical to measured wave height, H_m, i.e., $H_*=H_m$.
2. From H_*, measured mean water depth, h, and the wave period, estimate H_0/L_0 and h/L_0 by linear wave theory.
3. Substituting H_0/L_0, h/L_0 and $\tan\beta$ into (2.9), estimate nonlinear wave height, H.
4. Replace H_* by following formula, go back to 2 and iterate the same procedure until computed H becomes sufficiently close to H_m.

$$H_*^{new} = H_*^{old}\left(1+\frac{H_m - H}{H_m}\right) \tag{2.19}$$

Approximate velocity profile is then evaluated from the equivalent linear wave conditions by

approximation formulae, (2.10)-(2.14). Figures 2.13 and 2.14 show the computed velocity profile with measured data. In the figure, station 1 and 2 are outside the surf zone while stations 3, 4, 5 and 6 are inside the surf zone. Because of the existence of return flow, Measured data are adjusted by adding a constant value to make the measured average velocity zero. Approximation profiles agree well with measured data even inside the surf zone.

(2) Comparison with Cnoidal Wave Theory

Although our asymmetry profile model is based on the numerical experiments for uniform non-zero slope conditions, the applicability for the constant depth condition was also tested through comparison with Cnoidal 3rd order wave theory (Isobe, 1979). The relationship between non-linear wave height and linear wave height was determined by the same procedure as previous application. Figures 2.15 and 2.16 show comparison of velocity profiles estimated by 3rd order Cnoidal Wave Theory and present model. From the figures, it is found that our model also agrees well with Cnoidal wave theory.

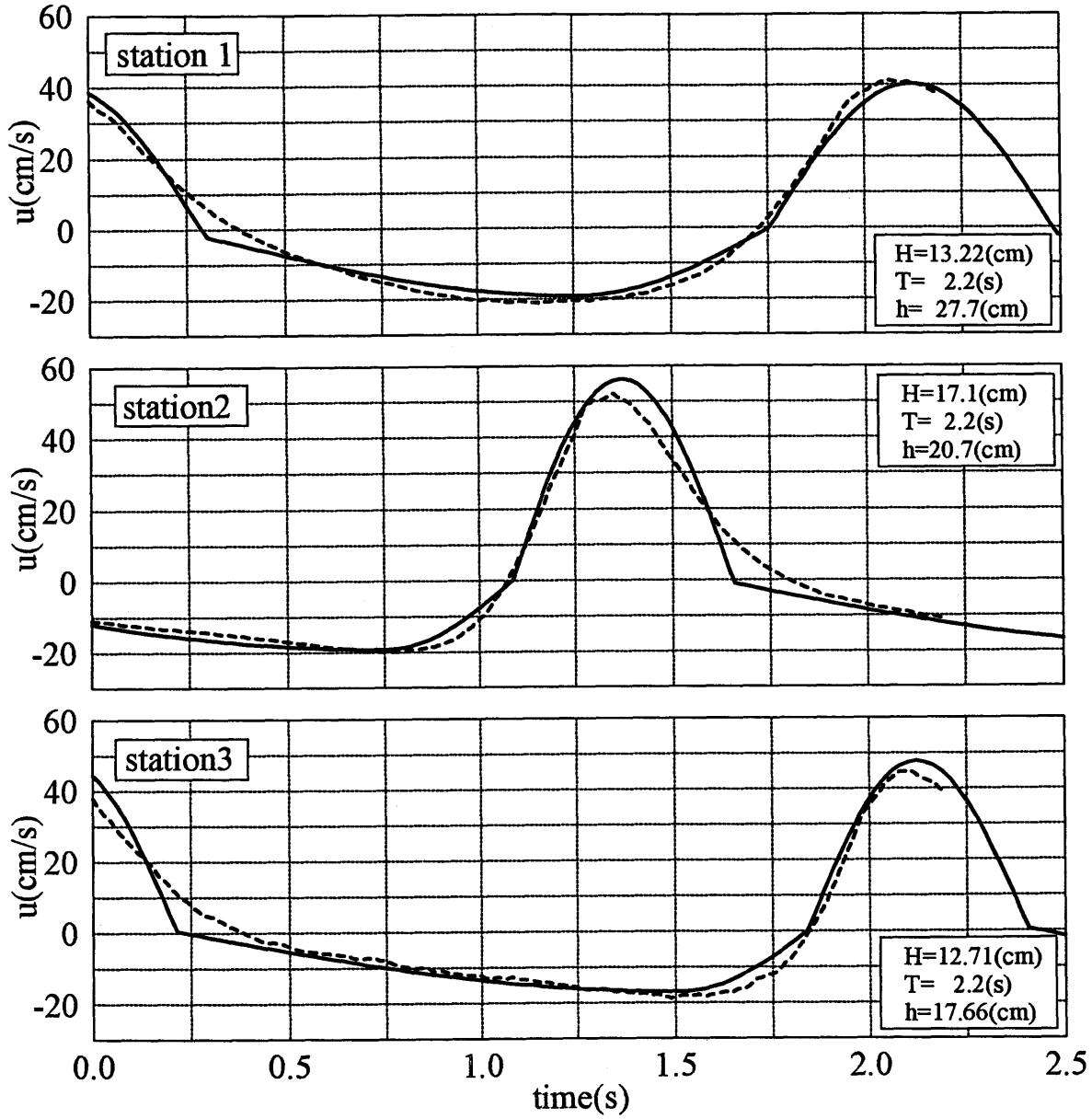

Figure-2.13 Approximation of the bottom orbital velocity profile with experimental data (Cox et al., 1995)

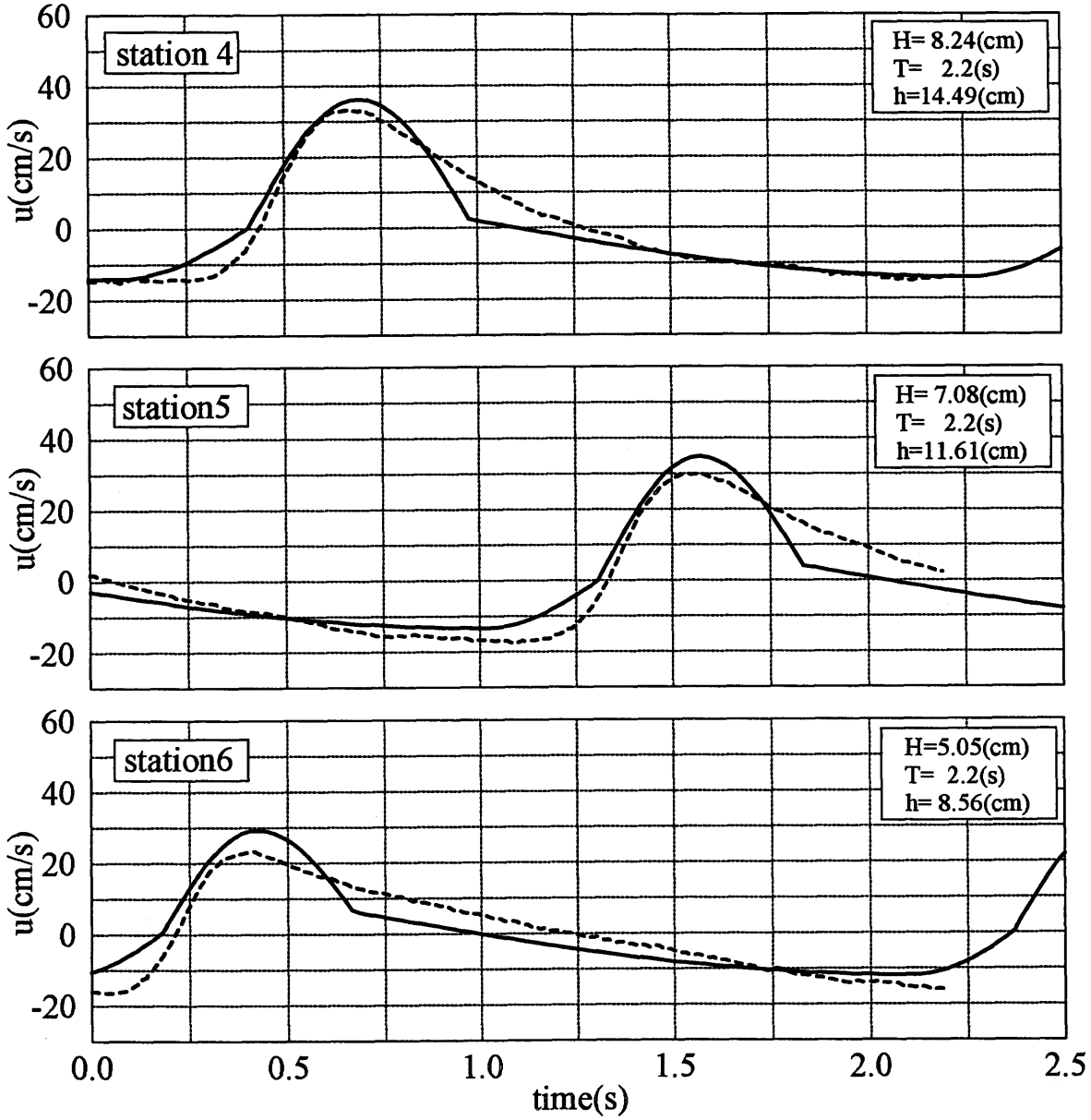

Figure-2.14 Approximation of the bottom orbital velocity profile with experimental data (Cox et al., 1995)

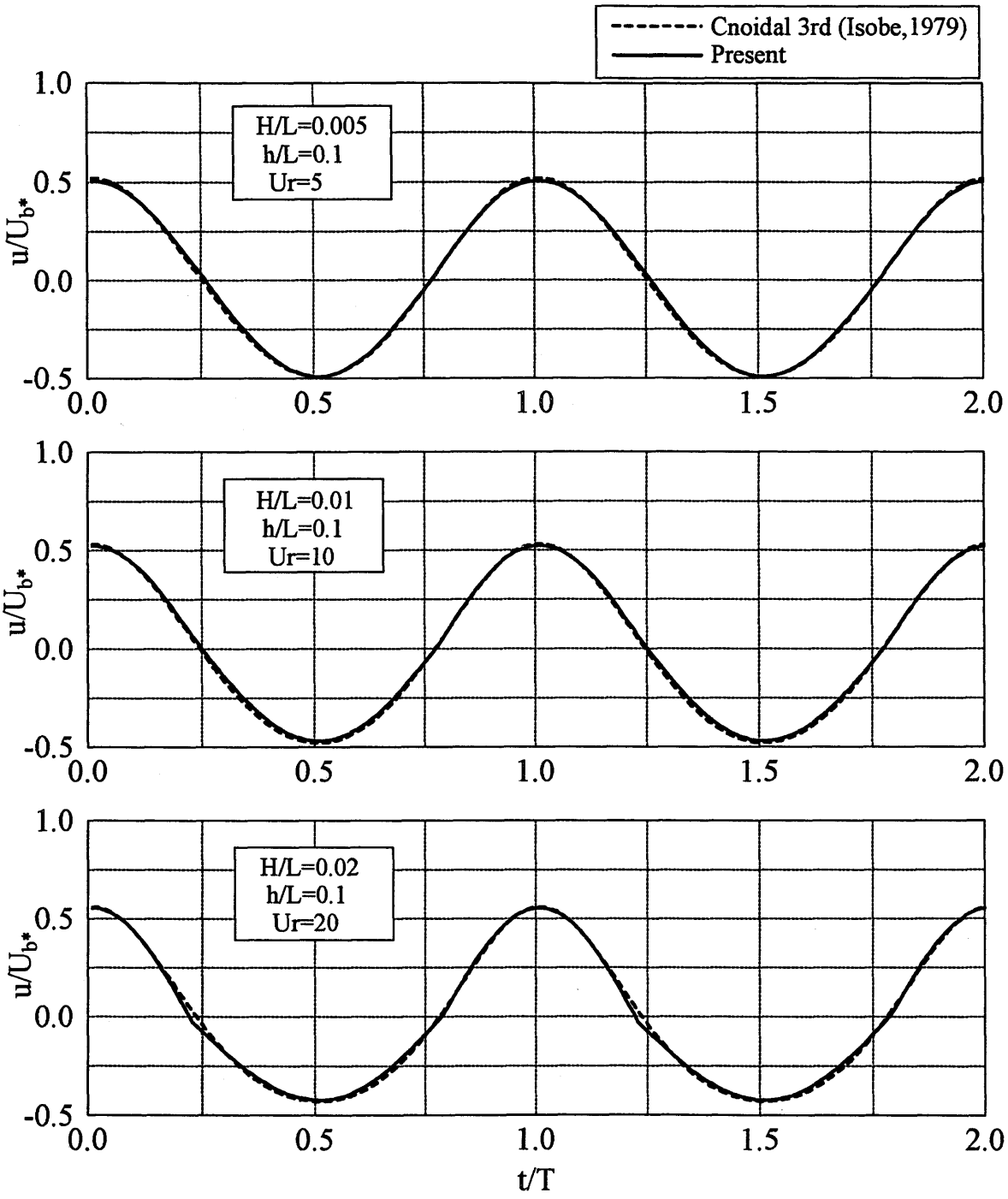

Figure-2.15 Approximation of the bottom orbital velocity profile with 3rd order Cnoidal wave theory

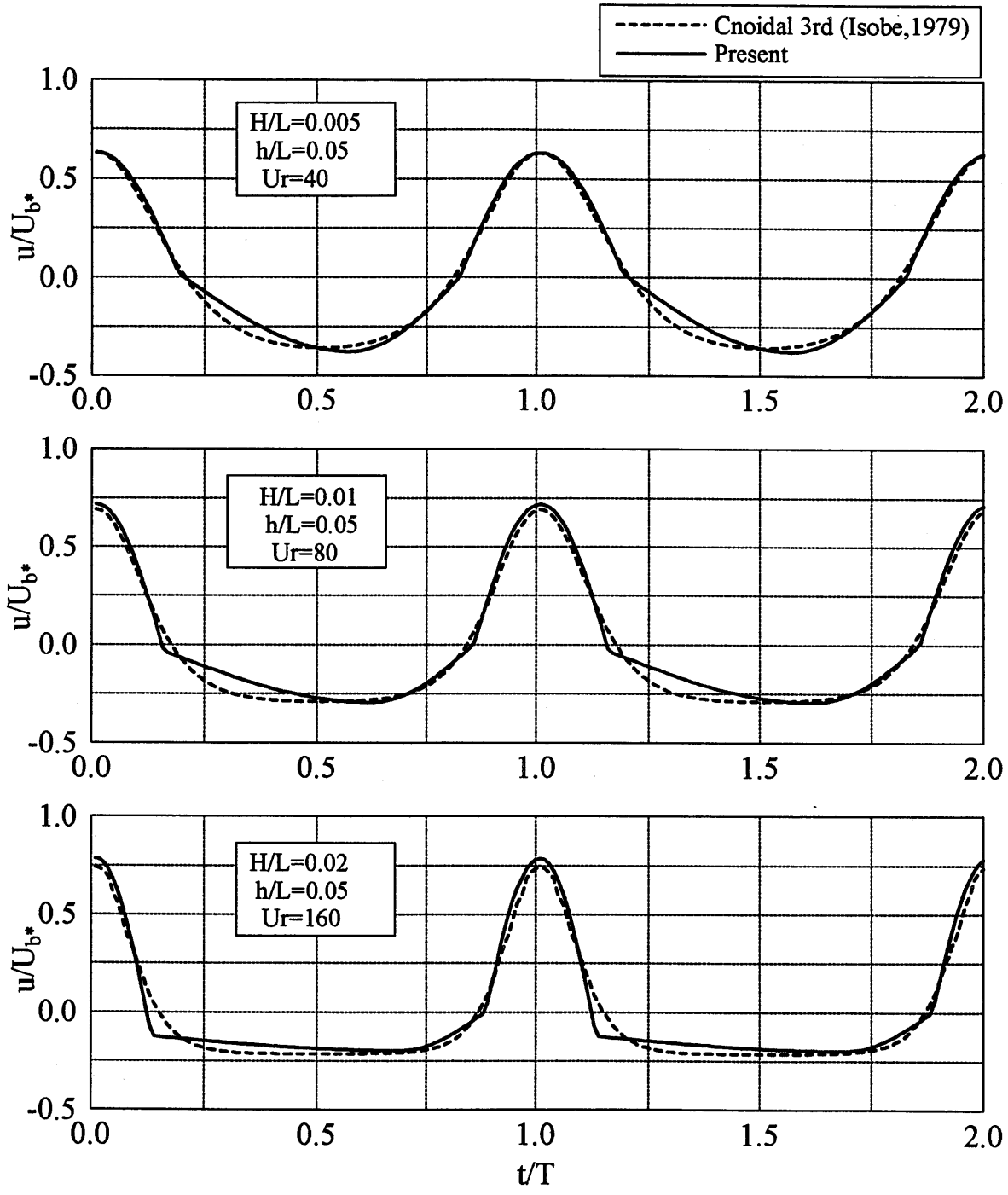

Figure-2.16 Approximation of the bottom orbital velocity profile with 3rd order Cnoidal wave theory

2.2 Breaking Wave Dissipation Model

In the Section 2.1, we proposed a semi-theoretical method to evaluate wave asymmetry and skewness from the local wave conditions based on linear wave theory. In this sense, our breaking wave model should also be based on linear wave theory and be able to evaluate local equivalent linear wave conditions accurately.

Generally, a breaking wave model consists of two steps. One is to find the breaking point and the other is to determine wave attenuation after the waves start to break. Both steps are to be consistent with our adopted methodology, i.e., to be based on linear wave theory. Especially for the second step, we need to estimate the attenuation of the equivalent linear wave height.

As for breaking criteria based on linear wave theory, Watanabe's (1984) breaking criteria is useful. As a parameter which determines onset of wave breaking, he used u_{cr}/C, the ratio of horizontal particle velocity under the wave crest and the wave celerity. Since u_{cr}/C is estimated from linear wave theory, we can determine the breaking point for the equivalent linear wave conditions. Because his model is based on Goda's (1970) breaking criteria, moreover, we can expect acceptable accuracy of his model.

As for breaking wave dissipation models based on linear wave theory, some semi-empirical energy dissipation models have been proposed and used in practice, e.g. Dally et al. (1985) and Watanabe and Dibajnia (1988). Although the applicability of these models is already confirmed through the comparison with measured data, each model still has different problems. Moreover, almost all models are calibrated to match computed linear

wave height with measured wave height even though actual measured wave heights include wave non-linearity and therefore are expected to be larger than the equivalent linear wave height.

In this section, we first review Watanabe's (1984) breaking criteria, which is adopted in our model. As for the breaking wave dissipation model, we summarize physical characteristics of breaking waves. We then review previous energy dissipation models and discuss their advantages and disadvantages and propose a modified breaking wave energy dissipation model. We extend its application to random waves and examine the validity of the model by comparing its prediction and measured data.

2.2.1 Watanabe's (1984) Breaking Criteria

Based on Goda's (1970) empirical breaking criteria, Watanabe (1984) presented a breaking criteria in terms of u_{cr}/C, the ratio of particle horizontal velocity under the wave crest to the wave celerity. This parameter is estimated by linear wave theory. Procedures for the estimation are as follows.

1. From Goda's (1970) breaking criteria, find the breaking depth, h_b, for arbitrary bottom slope, $\tan\beta$, and the deep water wave steepness, H_0/L_0.
2. Based on linear wave theory, compute u_{cr}/C at the breaking point by following formula,

$$\left(\frac{u_{cr}}{C}\right)_b = \frac{kH_{*b}}{2\tanh kh_b} \tag{2.20}$$

where u_{cr} is the horizontal particle velocity at the mean water level under the wave crest and H_{*b} is the equivalent linear wave height at the breaking point, which is also estimated from h_b and H_0/L_0 by linear wave theory. Note that this H_{*b} is generally smaller than actual breaking wave height estimated by Goda's (1970) criteria because waves around the breaking point include considerable non-linearity.

3. Using the obtained results, represent the new breaking criteria, $(u_{cr}/C)_b$, as a function of h_b/L_0 and $\tan\beta$.

Figure-2.17 shows Watanabe's breaking criteria obtained in this manner. An approximation to this criteria is obtained as,

$$\left(\frac{u_{cr}}{C}\right)_b = 0.53 - 0.3\exp\left[-2.5\sqrt{\frac{h_b}{L_0}}\right] + 5\tan^{\frac{3}{2}}\beta\exp\left[-45\left(\sqrt{\frac{h_b}{L_0}} - 0.1\right)^2\right] \qquad (2.21)$$

One of significant advantages of Watanabe's breaking criteria is that we can predict the breaking point by application of linear wave theory. By using equation (2.21), we can determine the breaking limit of $(u_{cr}/C)_b$ in arbitrary depth. When our u_{cr}/C equals this limit, the wave will break and when it exceeds this limit, we will apply our breaking wave attenuation model.

From equation (2.21), we can numerically estimate the breaking depth as a function of bottom slope, $\tan\beta$, and the deep water wave steepness, H_0/L_0. Once we determine the breaking depth, we can also estimate non-linear breaking wave height from our approximation formula (2.9). Figure-2.18 shows the distribution of h_b/H_0 as a function of H_0/L_0 and the uniform bottom slope. In the figure, solid lines are estimated by Watanabe's approximation formula (2.21) and circles are read from Goda's (1970) breaking wave

criteria. As shown in the figure, Watanabe's breaking criteria agrees well with Goda's (1970) breaking criteria. Similarly, Figure-2.19 shows the distribution of H_b/h_b as a function of h_b/L_0 and the uniform bottom slope. In the figure, solid lines are estimated by equation (2.21) to determine breaking point but equation (2.9) is also used to evaluate non-linear breaking wave height. Circles plotted in the figure are read from Goda's (1970) breaking criteria. As seen in the figure, the difference between these models becomes significant where h_b/L_0 is less than 0.005 while the error of both models is within 10% where h_b/L_0 is larger than 0.005. On the other hand, our estimations of H_b/h_b, which are shown by solid lines in Figure-2.19, decreases except zero slope condition when h_b/L_0 is decreases and becomes less than 0.005. The main reason of this phenomenon is that the effect of the bottom slope, which makes H/H_* smaller, becomes non-negligible especially when h_b/L_0 becomes small. In such a shallow water region, the accuracy of Goda's (1970) breaking criteria is also doubtful because almost all the measured data used by Goda(1970) was in the range of $h_b/L_0 > 0.005$. This also means that the range of $h_b/L_0 < 0.005$ is of little importance in terms of practical use of wave breaking criteria. For example, if we have waves with a period of $8(s)$, the wave breaking depth for $h_b/L_0=0.005$ is less than $50(cm)$ and therefore the breaking wave height is also much less than $50(cm)$. These values surely have little importance for coastal engineering. Figure-2.20 shows Goda's (1970) original breaking criteria with measured data for $\tan\beta=1/30$. From the figure, we can also see that measured H_b/h_b values vary in the range of 20% and our model is sufficiently within this range.

One of the advantages of our model is that our bottom orbital velocity is dependent on linear wave height but not on the non-linear wave height. In this sense, all the information we need from the breaking criteria is the exact location of breaking point, i.e., the breaking depth, h_b. From the Figure-2.18, it is seen that we can estimate accurately the breaking point.

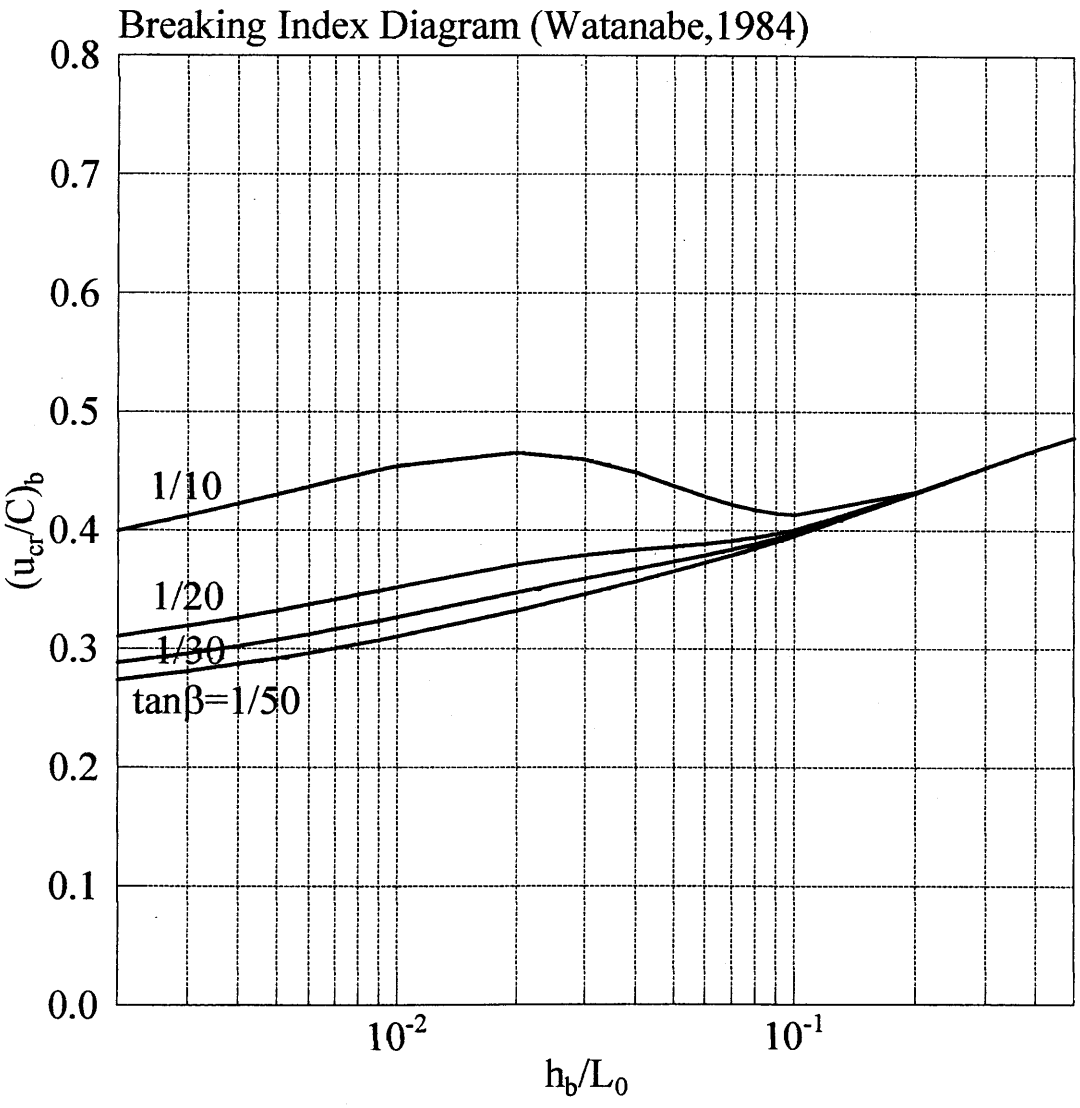

Figure-2.17 Watanabe's (1984) breaking criteria (approximation curve)

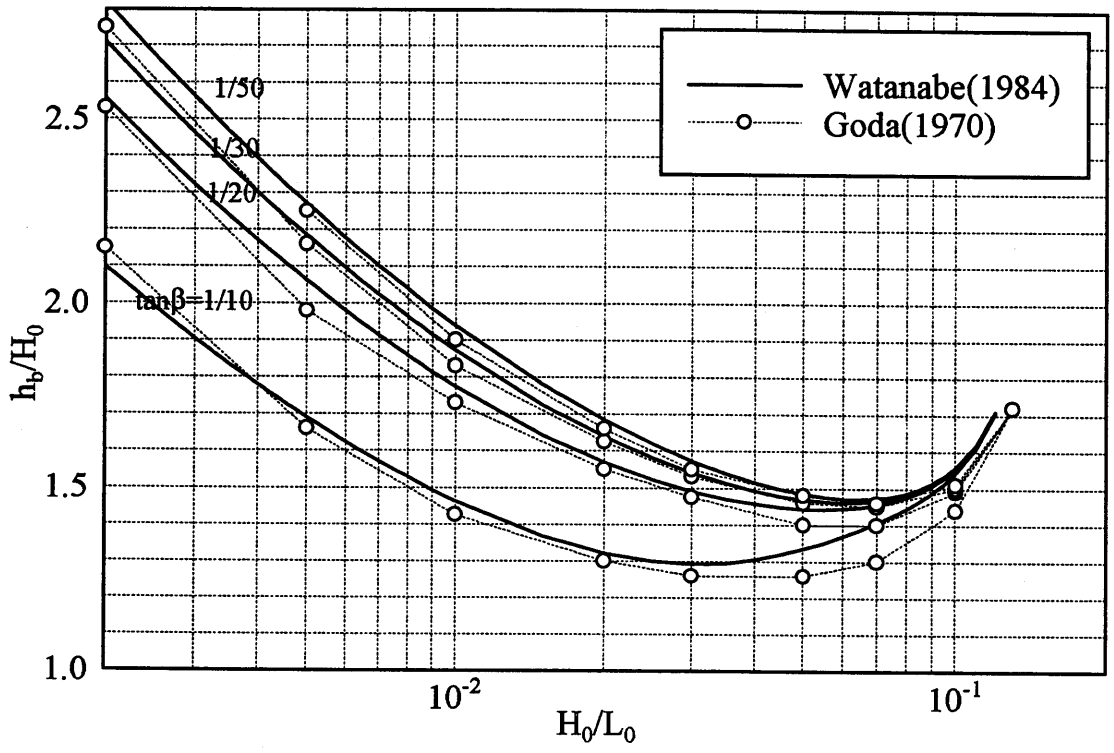

Figure-2.18 h_b/H_0 vs. H_0/L_0

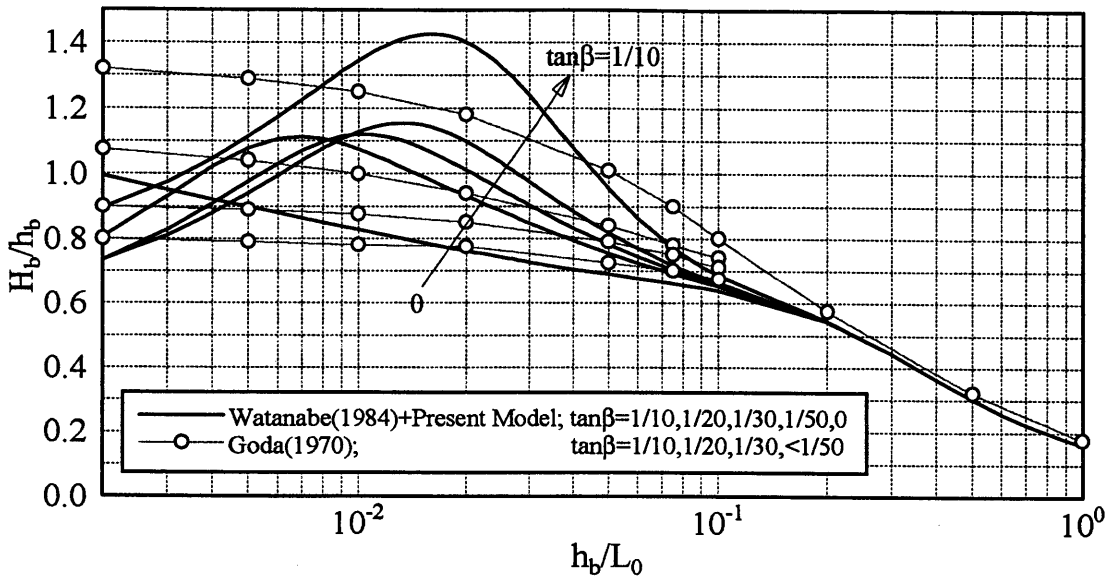

Figure-2.19 H_b/h_b vs. h_b/L_0

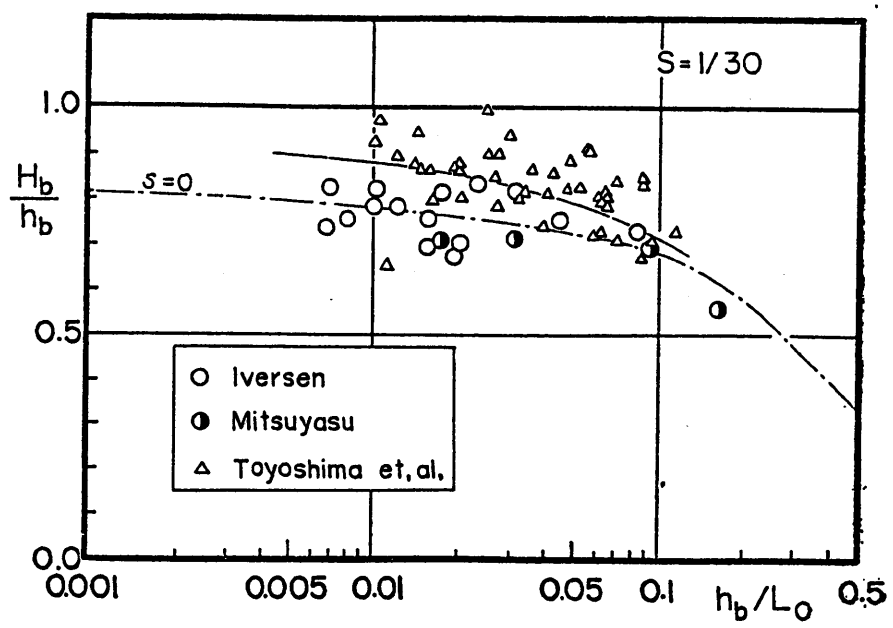

Figure-2.20 Goda's (1970) breaking criteria with experimental data

2.2.2 Physical Characteristics of Breaking Waves

From experimental data, physical characteristics of breaking-wave attenuation can generally be determined as follows. Here, γ is the ratio of wave height to the mean water depth.

1. Waves are taken to break when they reach a limiting value of $H/h=\gamma_b$.
2. When the breaking waves propagate on the constant depth, the ratio of wave height to the mean water depth, $\gamma=H/h$, goes to constant value, $\gamma=\gamma_r$ ($< \gamma_b$).
3. Breaking waves recover when $\gamma=\gamma_r$.
4. When the breaking waves propagate on a uniform slope, γ also goes to some constant value, γ_s, which is a function of the bottom slope, $\tan\beta$.
5. The relationship of γ_b, γ_r and γ_s is $\gamma_r \leq \gamma_s < \gamma_b$. When $\tan\beta=0$, $\gamma_r = \gamma_s$.

Note that all these observations are based on actual measured data, which includes wave non-linearity. Utilizing the observations of 1,2 and 3, Dally et al., (1985) developed the breaking wave energy dissipation model. In their model, however, the effect of the bottom slope is not considered while they comment that their constant parameter should be a function of bottom slope. Isobe (1987) developed a breaking wave energy dissipation model, which took into account the effect of bottom slope by utilizing facts 1, 2, 3 and 4. Watanabe and Dibajnia (1988) simplified Isobe's (1987) model by utilizing linear long wave theory. Since the Watanabe and Dibajnia's (1988) model is based on Isobe's (1987) model, these breaking dissipation models give quite similar results. In their model, breaking wave heights tend to be larger than experimental values especially when the bottom slope is

gentle. Although this problem can be modified by re-evaluating γ_s and γ_r, their model still have an inconsistency when $\tan\beta$ approaches zero. The Dally et al. (1985) and the Watanabe and Dibajnia (1988) models are reviewed hereafter.

2.2.3 Dally et al. (1985) Model

Dally et al. (1985) proposed that the breaking wave energy dissipation rate should be proportional to the difference of the local energy flux from recovery energy flux on the local depth, which is the energy flux rate when breaking waves recover after attenuation. From dimensional analysis, they also assumed that wave energy flux dissipation rate is inversely proportional to the water depth. Their energy dissipation rate is therefore defined as

$$\frac{\partial}{\partial x}\left(EC_g\right)=-\frac{K}{h}\left(EC_g-\left(EC_g\right)_r\right) \tag{2.22}$$

where K is constant, E is wave energy, C_g is the group velocity, h is the mean water depth and x is the horizontal axis in the shore-ward direction. Applying linear long wave theory, (2.22) is simplified as,

$$\frac{\partial}{\partial x}\left(\gamma^2 h^{\frac{5}{2}}\right)=-Kh^{\frac{3}{2}}\left(\gamma^2-\gamma_r^2\right) \tag{2.23}$$

Dally et al. (1985) calibrated the value of K and γ_r through comparison of equation (2.23) with experimental data obtained by Horikawa and Kuo (1966). Through this calibration, they found that the optimum values of K and γ_r are functions of the bottom slope. For practical convenience, however, they also showed that the average value of $K=0.15$ and

$\gamma_r=0.35$ gave sufficiently accurate breaking wave dissipation rates on an arbitrary bottom slope. When the waves break on the constant depth, (2.23) can be solved as

$$\gamma=\sqrt{\gamma_r^2+\left(\gamma_b^2-\gamma_r^2\right)\exp\left(-K\frac{x}{h}\right)} \tag{2.24}$$

Here $\gamma=\gamma_b$ at $x=0$ is specified as a boundary condition. From (2.24), γ surely converges to γ_r as x increases but requires an infinite "recovery distance", the distance from breaking point to recovery point where breaking waves reach γ_r.

Figure-2.21 shows the distributions of the wave height inside the surf zone on various uniform slopes, which are computed by this energy dissipation model with experimental data. In the figure, h' indicates still water depth. It is observed from the figure that energy dissipation rate is too small for the steeper slope but too large for the gentler slope. This clearly suggests that we need to determine the value of the constant K as a function of the bottom slope. The disadvantages of their models are summarized as follows.

1. Calibration was done by matching their estimated wave heights, which are based on linear long wave theory, with measured wave heights, which unavoidably include wave non-linearity.
2. If using constant value of $K=0.15$ and $\gamma_r=0.35$, their model gives too small dissipation rates on steep bottom slopes.
3. Recovery distance on a constant depth becomes infinite.

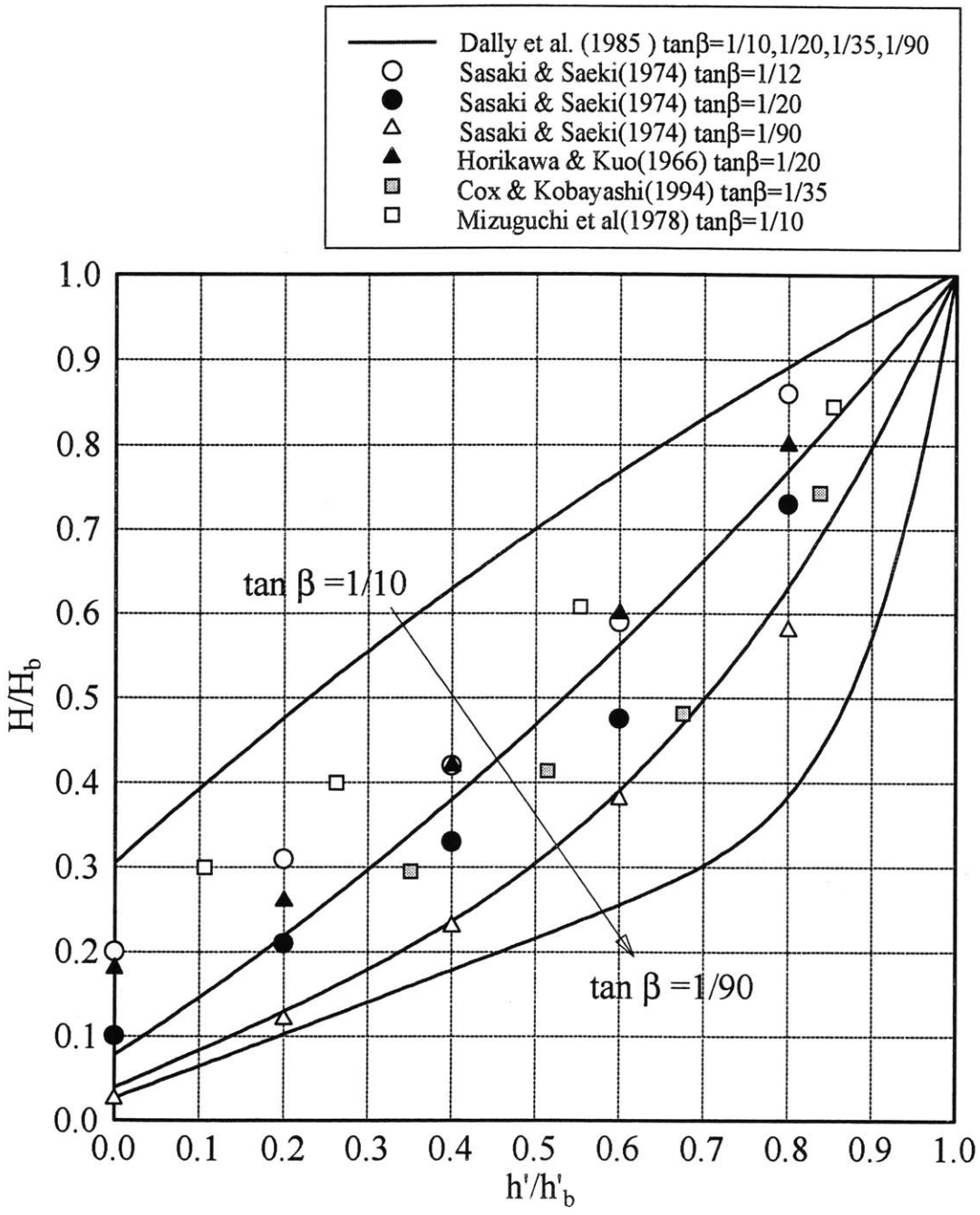

Figure-2.21 Comparison of the Dally et al. (1985) model with measured data

2.2.4 Watanabe and Dibajnia (1988) Model

For comparison with Dally et al. (1985) model, we review Watanabe and Dibajnia's (1988) model for $\gamma=H/h$. At first, they defined the energy dissipation rate as

$$\frac{\partial}{\partial x}(EC_g)=-\frac{A}{h}EC_g(\gamma-\gamma_r)^m \tag{2.25}$$

where A is a constant, which is a function of slope to be determined later by comparison with experimental results. The power of m is attached in order to obtain a finite recovery distance on the uniform depth, i.e., to remove the third disadvantage of Dally et al.'s (1985) model. By taking the power of m to be less than unity, the recovery distance becomes finite. This feature is shown with $m=1/2$, the value which Watanabe and Dibajnia (1988) used. Adopting linear long wave theory, and taking $m=1/2$, (2.25) becomes

$$\frac{\partial}{\partial x}\left(\gamma^2 h^{\frac{5}{2}}\right)=-A\gamma^2 h^{\frac{3}{2}}(\gamma-\gamma_r)^{\frac{1}{2}} \tag{2.26}$$

When the waves break on the uniform depth, (2.26) is analytically solved as

$$\gamma=\gamma_r\sec^2\left[-\frac{A\gamma_r^{1/2}}{4h}x+\arccos\sqrt{\frac{\gamma_r}{\gamma_b}}\right] \tag{2.27}$$

Similar to (2.24), $\gamma=\gamma_b$ at $x=0$ is specified as a boundary condition. From (2.27), γ becomes γ_r with finite recovery distance, $x=\frac{4h}{A\sqrt{\gamma_r}}\arccos\sqrt{\frac{\gamma_r}{\gamma_b}}$.

For uniformly sloping bed, (2.26) is represented as

$$2\gamma\frac{\partial\gamma}{\partial x}h^{\frac{5}{2}}+\frac{5}{2}\gamma^2 h^{\frac{3}{2}}\frac{\partial h}{\partial x}=-A\gamma^2 h^{\frac{3}{2}}(\gamma-\gamma_r)^{\frac{1}{2}} \tag{2.28}$$

Assuming that $\frac{\partial \gamma}{\partial x} = 0$ when $\gamma = \gamma_s$ and approximating $\frac{\partial h}{\partial x}$ as a gradient of the still water depth, i.e., $\frac{\partial h}{\partial x} = -\tan\beta$, A is determined from (2.28) as

$$A = \frac{5}{2\sqrt{\gamma_s - \gamma_r}} \tan\beta \tag{2.29}$$

Substituting (2.29) into (2.25), energy dissipation model is complete as

$$\frac{\partial}{\partial x}(EC_g) = -\frac{5}{2}\frac{EC_g}{h}\tan\beta\sqrt{\frac{\gamma - \gamma_r}{\gamma_s - \gamma_r}} \tag{2.30}$$

The determination of γ_s and γ_r is left. Based on experimental data(e.g. Maruyama and Shimizu (1986); and Saeki and Sasaki (1974)), Watanabe and Dibajnia (1988) defined these values as

$$\begin{cases} \gamma_r = 0.4\gamma_b \\ \gamma_s = 0.8(0.57 + 5.3\tan\beta) \end{cases} \tag{2.31}$$

where γ_b is γ at the breaking point. To obtain these values, they simply assumed that linear wave height is 80% of actual wave height and simply multiplied measured γ_s and γ_r obtained by Maruyama and Shimizu (1986) and Saeki and Sasaki (1974) by 0.8. Clearly, γ_s does not equal to γ_r when $\tan\beta$ is zero while, from the definition, these values should be identical for the no slope condition. In their model, moreover, dissipation rate becomes zero when $\tan\beta$ is zero. These problems can be resolved by modifying the definition of γ_r and γ_s. Figure-2.22 shows the distributions of the wave height inside the surf zone on various uniform slopes computed by Watanabe and Dibajnia (1988) model. From the figure, it is observed that the predicted variation of breaking wave heights with bottom slopes is much

smaller than suggested by the measured data. In other words, the Watanabe and Dibajnia (1988) model has too small a slope-dependency. As discussed before, moreover, it is expected that the Watanabe and Dibajnia (1988) model overestimates breaking wave heights when the bottom slope is small because their breaking wave dissipation rate becomes close to zero when the bottom slope approaches to zero. This, eventually, does not remove the third disadvantage of Dally et al.'s (1985) model. The disadvantages of Watanabe and Dibajnia's (1983) model are summarized as follows.

1. The model has too small a slope-dependency.
2. The breaking wave dissipation rate becomes too small when the bottom slope is very small.
3. The breaking wave dissipation rate becomes zero for the uniform depth conditions.

2.2.5 Modified Breaking Wave Dissipation Model

(1) Theoretical Formulation

Similar to Dally et al. (1985), we assume that energy dissipation rate, E_{diss}, is proportional to the difference between local wave energy, E, and recovery wave energy, E_r, i.e.,

$$E_{diss} \propto \frac{E - E_r}{\Delta t} \propto \frac{E - E_r}{h / C_g} \tag{2.32}$$

where characteristic time scale, Δt, is determined as $\Delta t = h/C_g$. Therefore, the energy dissipation equation due to breaking is expressed as

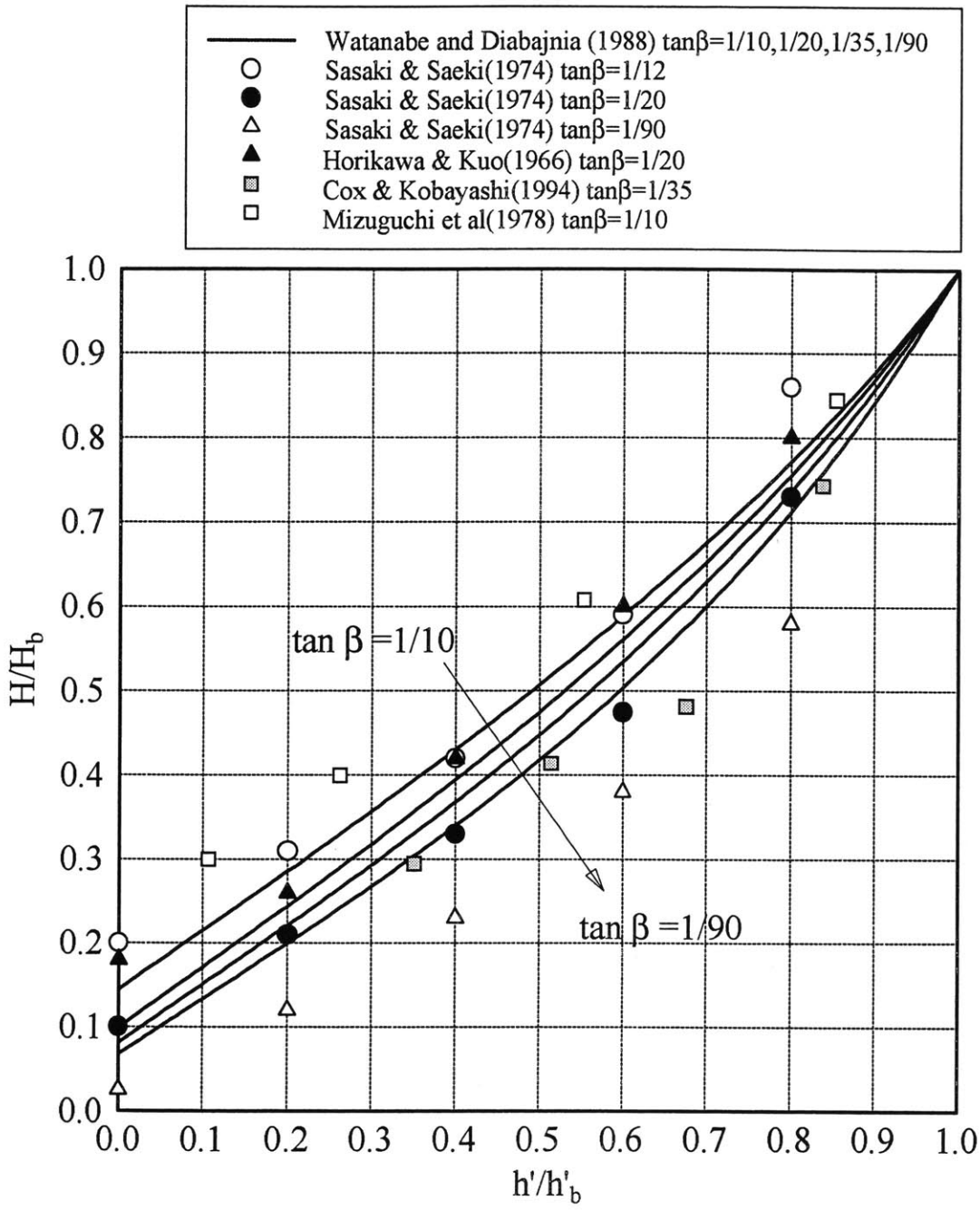

Figure–2.22 Comparison of the Watanabe and Dibajnia (1988) model with measured data

$$\frac{\partial}{\partial x}(EC_g) = -K\frac{C_g}{h}(E - E_r) \tag{2.33}$$

where K is a constant. This expression is identical to original Dally et al.'s (1985) definition (2.22). The same physical concept of the energy dissipation rate is to be applied later when developing a surface roller model. Although K is simply taken as a constant value in the original model, it is possible to determine K as a function of bottom slope by adopting a similar procedure to that employed by Watanabe and Dibajnia (1988). Assuming linear long wave theory, equation (2.33) becomes

$$\frac{\partial}{\partial x}\left(\gamma^2 h^{\frac{5}{2}}\right) = -Kh^{\frac{3}{2}}\left(\gamma^2 - \gamma_r^2\right) \tag{2.34a}$$

or

$$2\gamma\frac{\partial\gamma}{\partial x}h^{\frac{5}{2}} + \frac{5}{2}\gamma^2 h^{\frac{3}{2}}\frac{\partial h}{\partial x} = -Kh^{\frac{3}{2}}\left(\gamma^2 - \gamma_r^2\right) \tag{2.34b}$$

Assuming that $\frac{\partial\gamma}{\partial x} = 0$ when $\gamma = \gamma_s$, K is determined from (2.34b) as

$$K = \frac{-5\gamma_s^2}{2(\gamma_s^2 - \gamma_r^2)}\frac{\partial h}{\partial x} \tag{2.35}$$

According to Longuet-Higgins (1964), wave set-up inside the surf zone is determined by linear long wave theory as

$$\frac{\partial\overline{\eta}}{\partial x} = \frac{3\gamma^2}{8 + 3\gamma^2}\tan\beta \tag{2.36}$$

Here, it is assumed that γ and the bottom slope is constant inside the surf zone. Utilizing (2.36), and taking $\gamma = \gamma_s$, $\frac{\partial h}{\partial x}$ in (2.35) is expressed as

$$\frac{\partial h}{\partial x} = -\tan\beta + \frac{\partial \bar{\zeta}}{\partial x} = -\tan\beta\left(1 - \frac{3\gamma_s^2}{8+3\gamma_s^2}\right) \tag{2.37}$$

From (2.35) and (2.37), K is represented as

$$K = \frac{20\gamma_s^2}{8+3\gamma_s^2}\frac{\tan\beta}{\gamma_s^2-\gamma_r^2} \tag{2.38}$$

Substituting (2.38) into (2.32), energy dissipation model is finally determined as

$$\frac{\partial}{\partial x}(EC_g) = -\frac{5}{2}\rho g h C_g \gamma_s^2 \tan\beta\left(\frac{1}{8+3\gamma_s^2}\right)\frac{\gamma^2-\gamma_r^2}{\gamma_s^2-\gamma_r^2} \tag{2.39}$$

If we define γ_s and γ_r, referring to Watanabe and Dibajnia's (1986) model as

$$\begin{cases} \gamma_r = a \\ \gamma_s = a + b\tan\beta \end{cases} \tag{2.40}$$

it is clear that this modified model is still consistent when $\tan\beta$ is zero by the following examinations. When $\tan\beta$ is zero, K is estimated from (2.38) and (2.40) as

$$\lim_{\tan\beta\to 0} K = \lim_{\tan\beta\to 0}\frac{20\gamma_s^2}{8+3\gamma_s^2}\frac{\tan\beta}{\gamma_s^2-\gamma_r^2} = \lim_{\tan\beta\to 0}\frac{20(a+b\tan\beta)^2}{8+3(a+b\tan\beta)^2}\frac{\tan\beta}{(a+b\tan\beta)^2-a^2} = \frac{10a}{8+3a^2}\frac{1}{b} \tag{2.41}$$

Thus, K has some finite value as $\tan\beta$ goes to zero, which means that we still have a certain wave attenuation rate, while Watanabe and Dibajnia (1988) has zero dissipation rate, for constant depth conditions. Moreover, if substituting $a=0.28$ and $b=4.0$, which are obtained later, K is estimated from (2.37) as $K=0.085$. This value is reasonably consistent with K calibrated by Dally et al. (1985) for the non-slope condition.

(2) Determination of γ_s and γ_r

As mentioned above, γ_s is a function of the bottom slope and must be identical to γ_r when $\tan\beta$ is zero. Since our breaking wave dissipation model is based on linear wave theory, our γ_s and γ_r must also be based on equivalent linear wave theory. In order to avoid the conflicts of two different γ's determined by measured wave height or the equivalent linear wave height, we put subscripts "*m*" for actual measured values. In this section, actual values of γ_{sm} and γ_{rm} are first evaluated through comparison with various experimental data. Then, we finally determine γ_s and γ_r by converting γ_{sm} and γ_{rm}.

Figure-2.23 shows H/H_b vs. h'/h_b', on the *1/30* uniform slope, as obtained by Horikawa and Kuo(1966). Here, H is the local wave height inside the surf zone, H_b is the wave height at the breaking point, h' is still water depth and h_b' is still water depth at the breaking point. In the experiments, they observed that the characteristic curves of H/H_b vs. h'/h_b' are dependent on the bottom slope but hardly dependent on the wave steepness in deepwater, i.e., wave heights or wave periods. From the figure, we can also observe that H/H_b and h'/h_b' are linearly related to each other near the shoreline, i.e., the relationship of H/H_b and h'/h_b' is expressed as

$$\frac{H}{H_b} = \alpha \frac{h'}{h_b'} + \frac{H_s}{H_b} \tag{2.42}$$

where α is a constant and H_s is the wave height at the still water shoreline. From their observation, the value of α has little dependency on wave period and breaking wave height but is a function of $\tan\beta$. Table-2.2 shows α on various bottom slopes obtained by Horikawa and Kuo(1966) and Mizuguchi et al. (1978).

Table-2.2 α as a function of tanβ

tanβ	α
1/10	0.60(1)
1/20	0.59(2)
1/30	0.57(2)
1/65	0.49(2)
1/80	0.46(2)

(1) Mizuguchi et al. (1978)
(2) Horikawa and Kuo (1966)

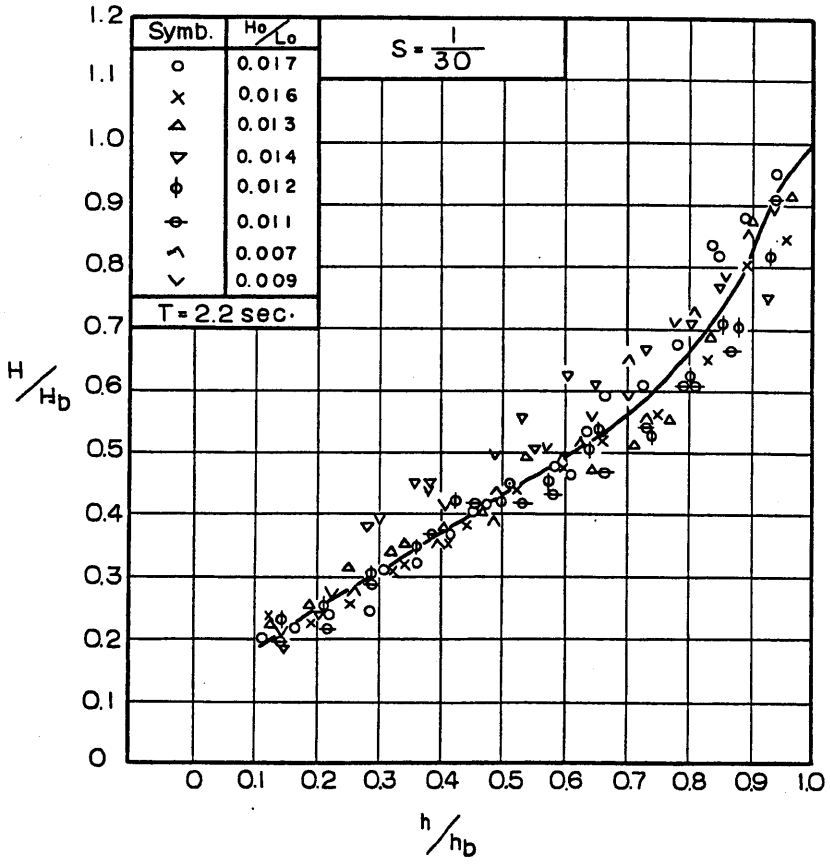

Figure-2.23 H/H_b vs. h'/h'_b on the 1/30 uniform slope (Horikawa and Kuo, 1966)

Differentiating (2.42) by horizontal axis, x,

$$\frac{\partial H}{\partial x} = \alpha \frac{H_b}{h_b'} \frac{\partial h'}{\partial x} = -\alpha \gamma_b \tan\beta \tag{2.43}$$

Therefore, γ_{sm} is determined from (2.43) as

$$\gamma_{sm} = \frac{\partial H}{\partial x} \Big/ \frac{\partial (h' + \overline{\eta})}{\partial x} \tag{2.44}$$

In order to compute (2.44), we need to estimate the wave set-up. Here, we again apply Longuet-Higgins' (1964) formula (2.36), which is to be valid near the shoreline because γ is observed to be a constant value, i.e., $\gamma = \gamma_{sm}$ as assumed for determining (2.36). From equations (2.36) and (2.44), γ_{sm} near the still water shoreline is determined as,

$$\gamma_{sm} = \frac{\partial H}{\partial x} \Big/ \frac{\partial (h' + \overline{\eta})}{\partial x} = \frac{-\alpha \gamma_{bm} \tan\beta}{-\tan\beta + \dfrac{3\gamma_{sm}^2}{8 + 3\gamma_{sm}^2} \tan\beta} = \alpha \gamma_{bm} \left(1 + \frac{3}{8} \gamma_{sm}^2 \right) \tag{2.45}$$

Therefore

$$\gamma_{sm} = \frac{1 - \sqrt{1 - 1.5\alpha^2 \gamma_{bm}^2}}{0.75 \alpha \gamma_{bm}} \tag{2.46}$$

The ratio of H/h at the initial breaking point, γ_{bm}, is evaluated by Goda's (1975) empirical formula as

$$\gamma_{bm} = 0.17 \frac{L_0}{h_b} \left[1 - \exp\left(-1.5\pi \frac{h_b}{L_0} \left(1 + 15 \tan^{4/3} \beta \right) \right) \right] \tag{2.47}$$

This γ_{bm} is identical to the actual γ at the breaking point. Although (2.36) is based on linear wave theory and therefore γ in (2.36) should be obtained by equivalent linear wave theory,

we used γ_{sm} in stead of γ_s in (2.45). Since wave set-up gradient is generally much smaller than bottom slope, this should be a reasonable approximation.

Figure-2.24 shows γ_{sm} predicted by equations (2.46) and (2.47) as a function of $\tan\beta$. When computing (2.47), h_b/L_0=*0.01* and *0.05* are used as a general value at a breaking point. The figure also includes γ_{sm}, which is directly measured in the experiments performed by Cox et al. (1995) and Okayasu et al. (1988, 1990). As seen in the figure, values estimated from (2.46) and (2.47) are dependent on h_b/L_0. Although this dependency becomes non-trivial when the bottom slope is steeper, we simply determine γ_{sm} as

$$\gamma_{sm} = 0.35 + 6.5\tan\beta \tag{2.48}$$

which is the straight line shown n the Figure-2.24. This implies that γ_{rm} is γ_{rm}=*0.35* which is identical to γ_{sm} when $\tan\beta$=0. This value is consistent with the Dally et al.(1985) model.

(3) Determination of γ_{sm} and γ_{rm}

Our estimation of γ_{sm} and γ_{rm} is now complete. In order to apply these values to our breaking wave dissipation model, we need to convert them into the values for the equivalent linear wave height. If a local depth, actual wave height and wave period are specified, the equivalent linear wave height can be estimated from equation (2.9) by following the same procedures discussed in the Section 2.1.6. Therefore, if the actual wave heights are determined by (2.48) on arbitrary local depth, we can estimate equivalent linear wave heights, i.e., γ_s as functions of a wave period and the bottom slope.

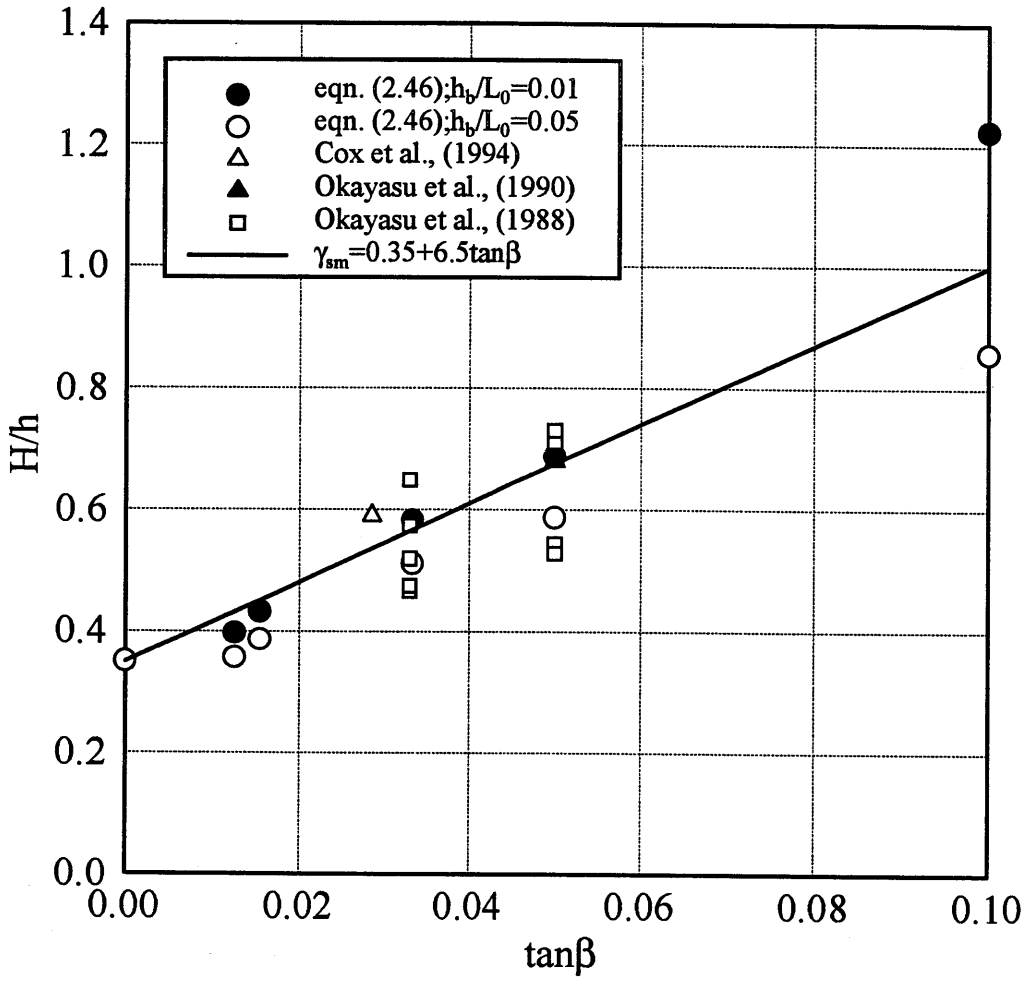

Figure-2.24 γ_{sm} vs. tanβ

Figure-2.25 shows the converted γ_s vs. h/L_0 for various slopes estimated in this manner. From the figure, it is seen that the value of γ_s has little dependency on h/L_0 and therefore it is reasonable that we can pick γ_s around $h/L_0=0.01$, where most breaking waves on the uniform slope are expected to reach γ_s. Figure-2.26 shows converted γ_s with γ_{sm} picked from the lines in Figure-2.25 at $h/L_0=0.01$ and $h/L_0=0.02$ as a function of $\tan\beta$. From the Figure-2.26, it is seen that both picked γ_s values at $h/L_0=0.01$ and 0.02 are close to each other. γ_s and γ_r are finally approximated by the straight line shown in the Figure-2.26, i.e.,

$$\begin{cases} \gamma_s = 0.28 + 4.0\tan\beta \\ \gamma_r = 0.28 \end{cases} \tag{2.49}$$

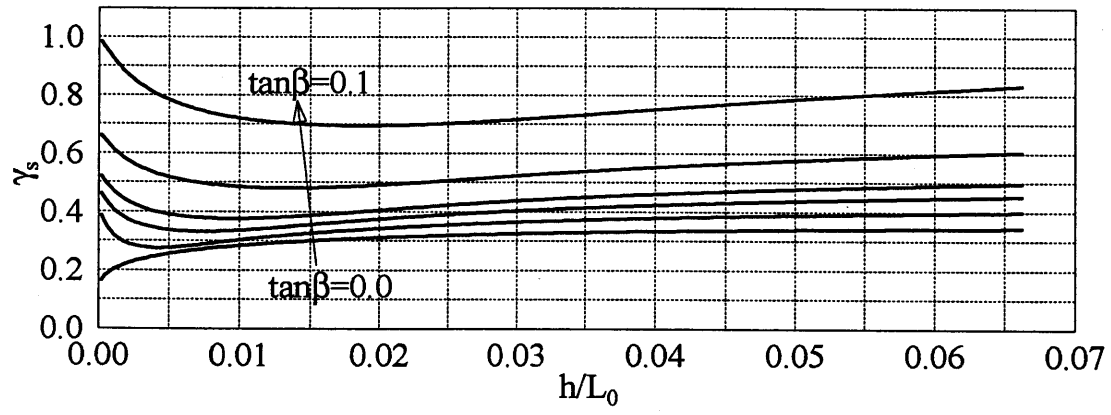

Figure-2.25 γ_s vs. h/L_0 for various bottom slope

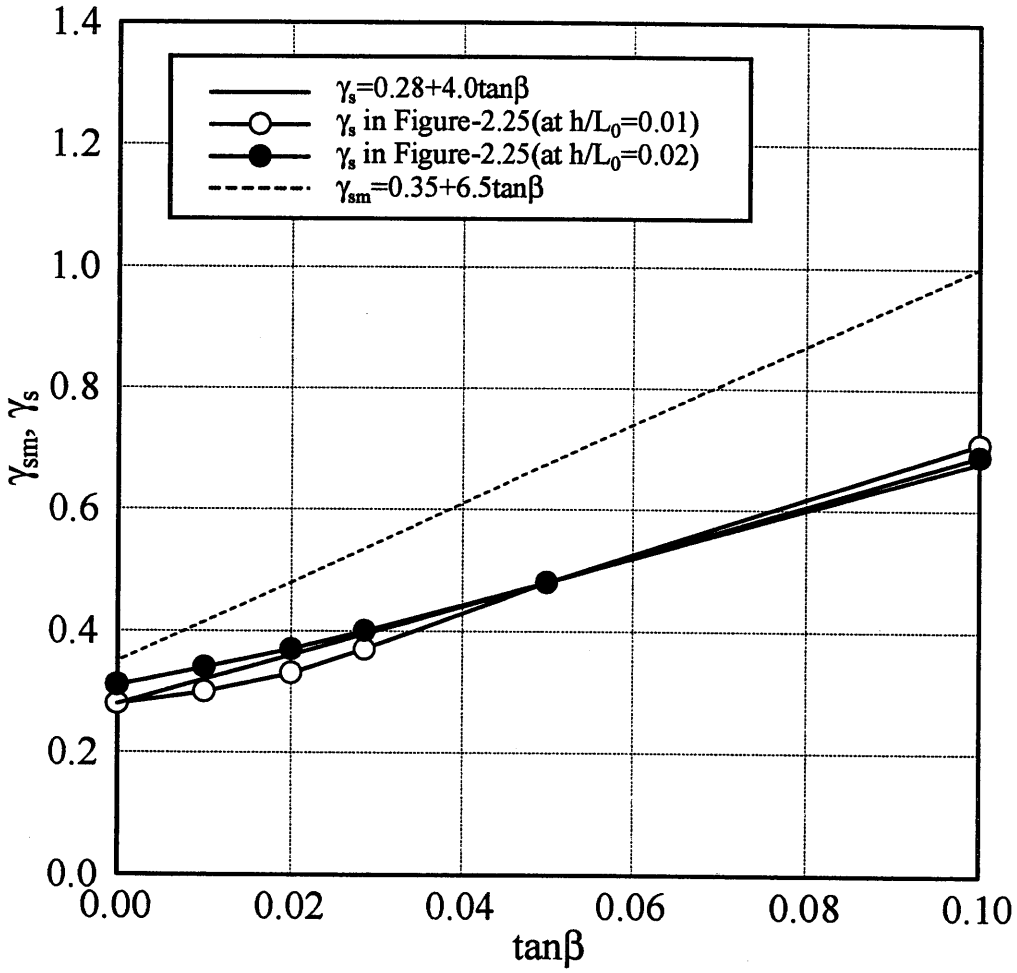

Figure-2.26 γ_s vs. tanβ

(4) Model Examination

Figure-2.27 shows the distributions of the non-linear wave heights inside the surf zone on various uniform slopes computed by the present model. In the figure, non-linear wave heights are estimated from our approximation formula (2.9). The detailed methodology for numerical application of the model is discussed later in the Section 2.3. From the figure, it is clear that our breaking dissipation model estimates wave attenuation more accurately than any of the previous models.

2.2.6 Model Extension for Random Wave Problem

The modified breaking wave dissipation model for regular waves is now complete. Since our model is entirely based on wave energy, it is possible to extend the model to the random wave problem by taking averages for all waves. To extend the model for random wave conditions, the following assumptions are made.

1. The frequency spectrum of the random waves is narrow banded, i.e., the frequency can be approximated by a single value.
2. The wave heights are Rayleigh distributed. According to Longuet-Higgins (1952), the probability density function for wave heights is expressed as

$$p(\xi) = 2\xi \exp\left(-\xi^2\right) \tag{2.50}$$

where $\xi = H/H_{rms}$ and H_{rms} is the root-mean-square wave height. Since this assumption of Rayleigh distribution is based on linear wave theory, these wave heights should be the equivalent linear wave heights.

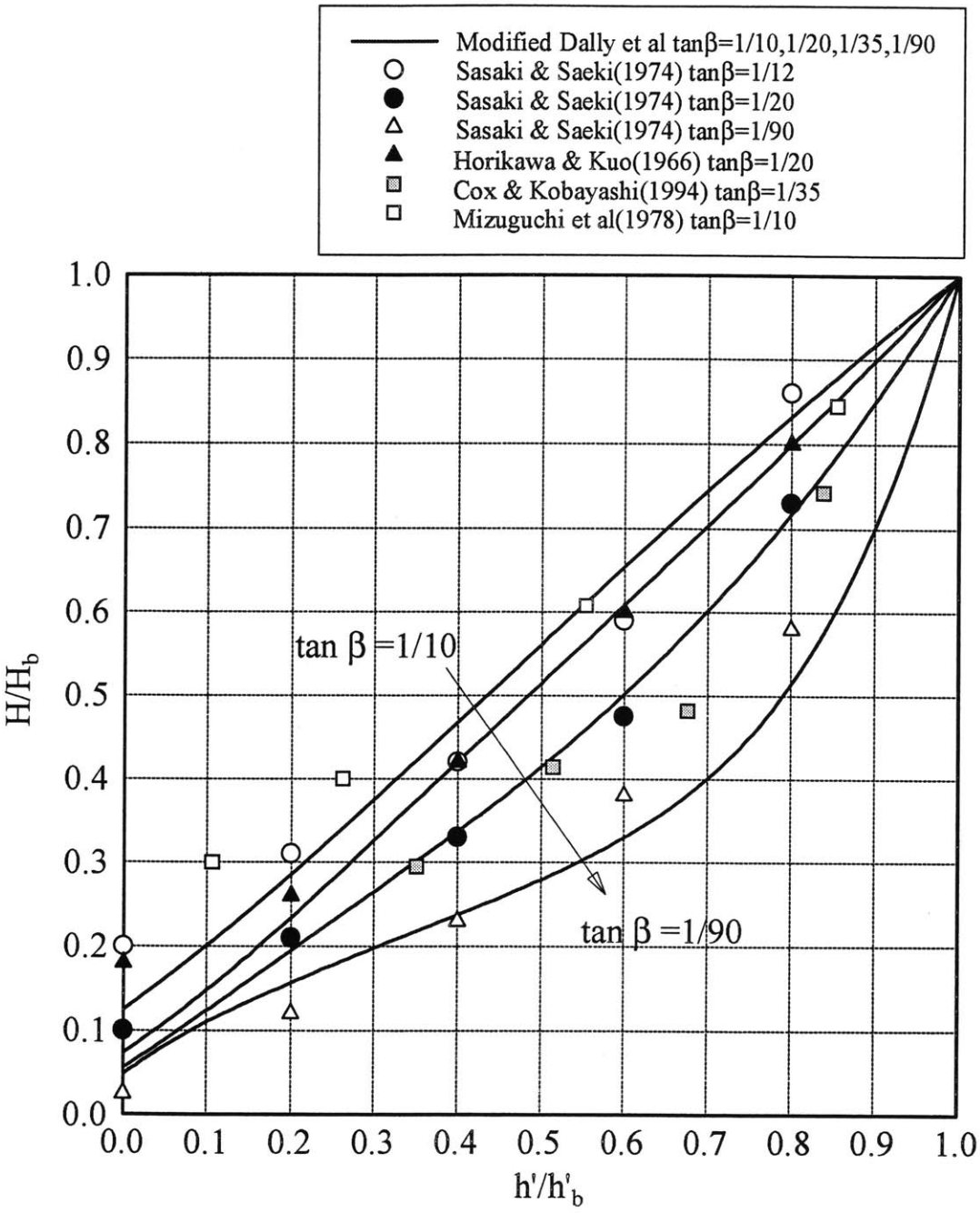

Figure-2.27 Comparison of the present model with measured data

3. Based on linear wave theory, the average energy of the random waves can be obtained by averaging the energy of each wave.

From these assumptions, the total energy of the arbitrary random wave is

$$E=\frac{1}{8}\rho g\int_0^\infty H_{rms}^2\xi^2 p(\xi)d\xi=\frac{1}{8}\rho g\int_0^\infty H_{rms}^2 2\xi^3\exp(-\xi^2)d\xi=\frac{1}{8}\rho g H_{rms}^2 \tag{2.51}$$

Assuming that mean water level varies insignificantly from one wave to the next, the wave set up can be approximated by its averaged value as

$$\frac{\partial\overline{\eta}}{\partial x}=-\frac{3\gamma_{rms}^2}{8+3\gamma_{rms}^2}\tan\beta \tag{2.52}$$

where $\gamma_{rms}=H_{rms}/h$. Since energy dissipation is only applied to breaking waves, total energy dissipation rate is expressed from (2.39) and (2.50) as

$$\frac{\partial}{\partial x}(EC_g)=\int_{\xi_b}^\infty p(\xi)\left[-\frac{5}{2}\rho g h C_g\gamma_s^2\tan\beta\left(\frac{1}{8+3\gamma_s^2}\right)\frac{\gamma^2-\gamma_r^2}{\gamma_s^2-\gamma_r^2}\right]d\xi \tag{2.53}$$

and

$$EC_g=\frac{1}{8}\rho g\gamma_{rms}^2 h^2 C_g \tag{2.54}$$

where $\xi_b=H_b/H_{rms}$ with H_b, breaking wave height in arbitrary local depth. From the assumption, group velocity, C_g, can be represented by a single value. Since γ is the only variable that is a function of ξ, (2.53) can be easily integrated as

$$\begin{aligned}\frac{\partial}{\partial x}(EC_g)&=-A\int_{\xi_b}^\infty p(\xi)(\gamma_{rms}^2\xi^2-\gamma_r^2)d\xi=-A\int_{\xi_b}^\infty 2\xi(\gamma_{rms}^2\xi^2-\gamma_r^2)\exp(-\xi^2)d\xi\\&=-A\exp(-\xi_b^2)\left((1+\xi_b^2)\gamma_{rms}^2-\gamma_r^2\right)\end{aligned} \tag{2.55}$$

where

$$A = \frac{5\rho g h C_g \gamma_s^2 \tan\beta}{2(8+3\gamma_s^2)(\gamma_s^2-\gamma_r^2)} \tag{2.56}$$

From (2.55) and (2.56), final form of the breaking dissipation rate for random waves is therefore written as

$$\frac{\partial}{\partial x}(EC_g) = -\frac{5}{2}\rho g h C_g \gamma_s^2 \tan\beta \left(\frac{1}{8+3\gamma_s^2}\right) \exp(-\xi_b^2) \frac{(1+\xi_b^2)\gamma_{rms}^2 - \gamma_r^2}{\gamma_s^2 - \gamma_r^2} \tag{2.57}$$

Since Watanabe's (1984) breaking criteria parameter, u_{cr}/C, is proportional to linear wave height, ξ_b can also be determined by this criteria as

$$\xi_b = H_{b*}/H_{rms} = (u_{cr}/C)_b / (u_{cr}/C)_{rms} \tag{2.58}$$

From (2.56), averaged dissipation rate of the wave energy flux and therefore averaged wave energy at an arbitrary point can be estimated numerically. Root-mean-square of random wave heights and linear significant wave height, H_s, are determined from (2.51) as

$$\begin{aligned} H_{rms} &= \sqrt{8E/\rho g} \\ H_s &= 1.416 H_{rms} \end{aligned} \tag{2.59}$$

More detailed methodologies for the numerical application of this model is discussed in the next section.

2.3 Model Application

Theoretical formulation of breaking wave dissipation model for regular waves and random waves is now complete. In this section, the methodology for the numerical application of the model is discussed and the applicability of the model is examined by comparing numerical results with experimental data.

2.3.1 Model Application for Numerical Computation

(1) Regular Waves

Adopting a forward difference scheme, the equation (2.39) for breaking wave energy dissipation rate is discretized as

$$\frac{(EC_g)_{i+1}-(EC_g)_i}{\Delta x}=-\frac{5}{2}\rho g h_i C_{g,i}\gamma_s^2(\tan\beta)_i\left(\frac{1}{8+3\gamma_s^2}\right)\frac{\gamma_i^2-\gamma_r^2}{\gamma_s^2-\gamma_r^2} \tag{2.60}$$

where $h_i=h'_i+\overline{\eta}_i$, $(\tan\beta)_i=(h'_{i+1}-h'_i)/\Delta x$ and h'_i is still water depth at $n=i$ ($n=1,2,...,N$). $\overline{\eta}_i$ is the mean surface water elevation due to wave set-up/set-down. From (2.54), we can estimate energy flux at $n=i+1$ explicitly if we specify all variables at point $n=i$. Wave height and mean surface water elevation at $n=i+1$ are then estimated by following procedure.

1. Taking initial value of $\overline{\eta}_{i+1}$ as $\overline{\eta}_{i+1}=\overline{\eta}_i$.
2. The mean water depth at $n=i+1$ is now estimated as $h_{i+1}=h'_{i+1}+\overline{\eta}_{i+1}$ and then the equivalent linear wave height at $n=i+1$ is estimated from obtained energy flux and group velocity as

$$H_{*,i+1}=\sqrt{8(EC_g)_{i+1}/\rho g C_{g,i+1}} \tag{2.61}$$

Note that the group velocity at $n=i+1$ is a function of $\overline{\eta}_{i+1}$, which should be determined.

3. The mean surface water elevation due to wave set-up/set-down is determined by linear wave theory.

$$\frac{d\overline{\eta}}{dx} = -\frac{1}{\rho g(h'+\overline{\eta})}\frac{dS_{xx}}{dx} \tag{2.62}$$

where the radiation stress S_{xx} is $S_{xx} = \frac{1}{8}\rho g H_*^2\left(\frac{1}{2}+\frac{2kh}{\sinh 2kh}\right)$. Adopting a central difference scheme, (2.60) is discretized as

$$\frac{\overline{\eta}_{i+1}^{new}-\overline{\eta}_i}{\Delta x} = -\frac{2}{\rho g(h'_i+h'_{i+1}+\overline{\eta}_i+\overline{\eta}_{i+1})}\frac{S_{x,i+1}-S_{xx,i}}{\Delta x} \tag{2.63}$$

Here, $S_{xx,i+1}$ is also a function of $\overline{\eta}_{i+1}$. The mean surface water elevation, $\overline{\eta}_{i+1}^{new}$, is newly determined from equation (2.63).

4. Taking $\overline{\eta}_{i+1} = \overline{\eta}_{i+1}^{new}$, iterate the same procedures until $\overline{\eta}_{i+1}$ converges.

Starting from $n=2$ with initially given offshore wave conditions at $n=1$, equivalent linear wave heights and mean surface water level at $n=2,3,...,N$ are computed one by one. Here, assuming that the water depth at offshore boundary is deep enough and therefore the wave set-up/set-down is negligibly small, we take $\overline{\eta}_1 = 0$. During the computation, (2.60) is applied when $u_{c,i}/C_i > (u_c/C)_{b,i}$ where $(u_c/C)_{b,i}$ is estimated by Watanabe's breaking criteria, (2.21). Once waves start to break, breaking wave energy dissipation (2.60) is applied until the ratio of the local wave height to mean water depth, $H_{*i}/(h'_i+\overline{\eta}_i)$, becomes less than γ_r. To make the distance for wave recovery finite, we determine the recovery point by $H_{*i}/(h'_i+\overline{\eta}_i) < 1.01\gamma_r$.

(2) Random Waves

The basic idea for numerical computation of breaking wave dissipation for random waves is the same as that for regular waves, which is discussed in the previous section. As for breaking wave energy dissipation, however, we use (2.57) instead of (2.39). Dicretized formula of (2.57) is

$$\frac{(EC_g)_{i+1}-(EC_g)_i}{\Delta x}=-\frac{5}{2}\rho g h_i C_{g,i}\gamma_s^2(\tan\beta)_i\left(\frac{1}{8+3\gamma_s^2}\right)\exp(-\xi_{b,i}^2)\frac{(1+\xi_{b,i}^2)\gamma_{rms,i}^2-\gamma_r^2}{\gamma_s^2-\gamma_r^2} \tag{2.64}$$

Mean surface water elevation is determined by (2.63) but the averaged radiation stress S_{xx} is determined based on root-mean-squared wave height, i.e.,

$$S_{xx}=\frac{1}{8}\rho g H_{rms}^2\left(\frac{1}{2}+\frac{2kh}{\sinh 2kh}\right) \tag{2.65}$$

Similarly starting from $n=2$ with initially given offshore wave conditions at $n=1$, root-mean-squared wave heights and mean surface water level at $n=2,3,...,N$ are computed one by one. The significant difference between numerical methodologies for regular waves and random waves is that wave energy dissipation is always computed by (2.64) for random waves while energy dissipation is applied only after waves start to break for regular waves.

2.3.2 Model Test

For further examination, other tests are carried out on experimental data presented by Cox et al. (1995) and Okayasu and Katayama (1992). Table-2.3 shows conditions of all cases. In the table, h_i is offshore water depth, H_i is incident wave height and H_0 is deepwater wave height. The deepwater wave height, H_0, is estimated by linear wave theory after converting measured incident wave height into equivalent linear wave height by Cnoidal wave theory. For the random waves, significant wave heights and significant wave period are shown in the table.

Table-2.3 Conditions of the Experiments

CASE	beach type	slope	wave condition	h_i(cm)	H_i(cm)	H_0(cm)	T(s)
1	uniform	1:35	regular	40.0	11.50	11.10	2.200
2	uniform	1:20	regular	35.0	7.85	8.60	1.200
3	uniform	1:20	random	35.0	8.28	9.06	1.260
4	bar-type	1:20	random	32.0	5.67	6.12	0.945
5	bar-type	1:20	random	32.0	7.52	8.24	1.140

1 : Cox et al. (1995)
2-5: Okayasu and Katayama (1992)

Figures 2.28 to 2.32 show comparison of computed wave heights and mean water level with measured data. In the Figures 2.28 (Case 1) and 2.29 (Case 2), the dotted line is the linear wave height computed directly from the local energy flux and the solid line is the converted non-linear wave height. In the random wave cases, linear significant wave height is plotted. Since our breaking wave dissipation model for random waves is based on Rayleigh distribution and the ratio of non-linear wave height to equivalent linear wave height is different for each wave, this model cannot estimate significant wave heights including wave non-linearity. It is however found that our model estimates wave height attenuation fairly well. It is also seen that computed mean water level coincides well with measured data.

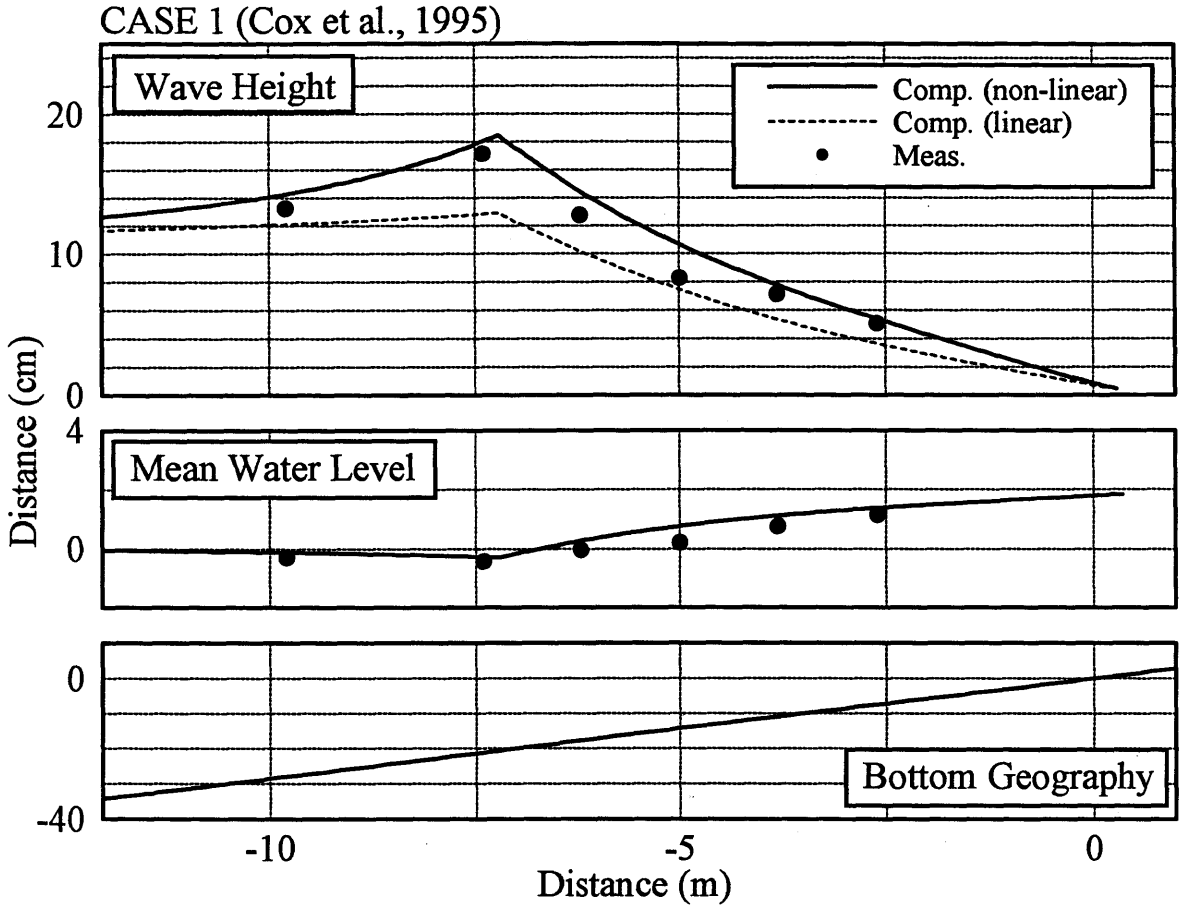

Figure-2.28 Wave heights and mean water level
(CASE 1 Cox et al., 1995)

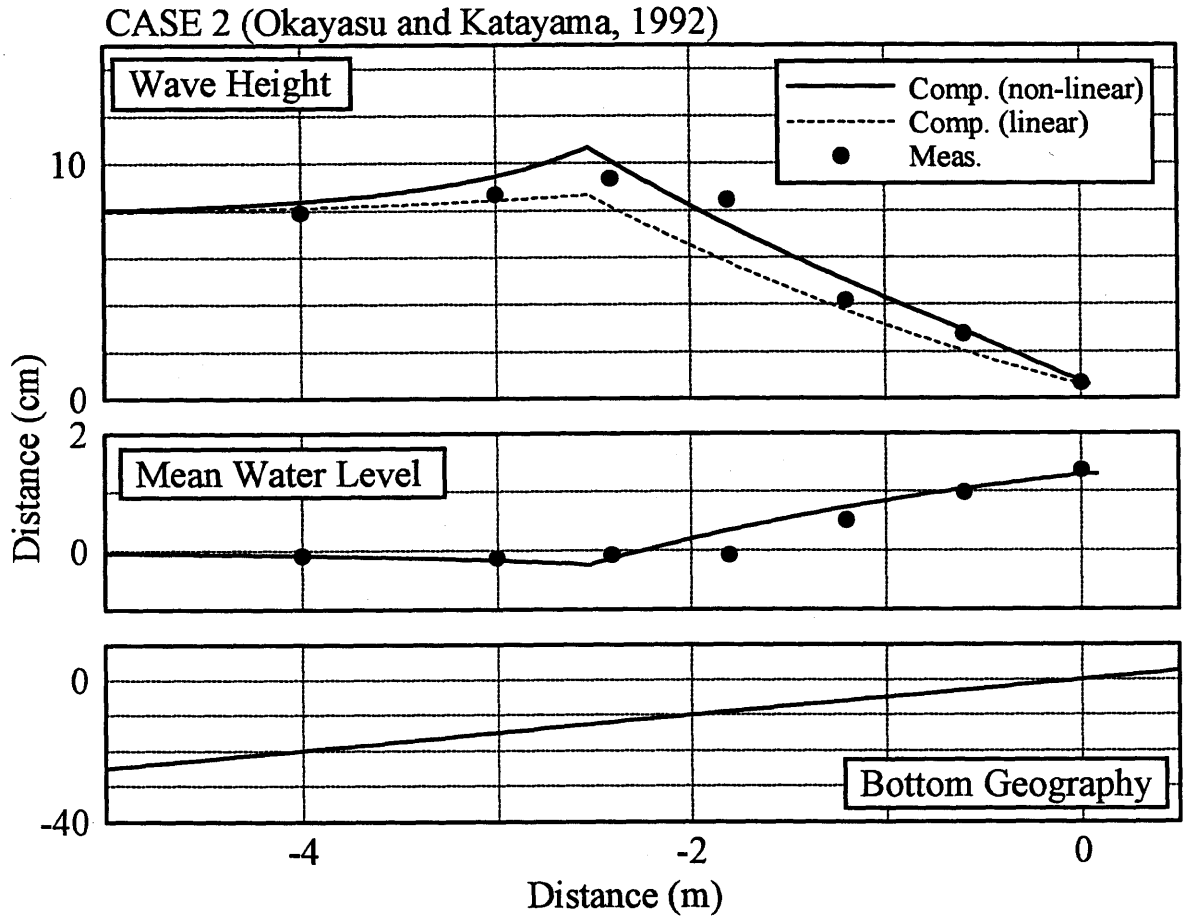

Figure-2.29 Wave heights and mean water level
(CASE 2 Okayasu and Katayama, 1992)

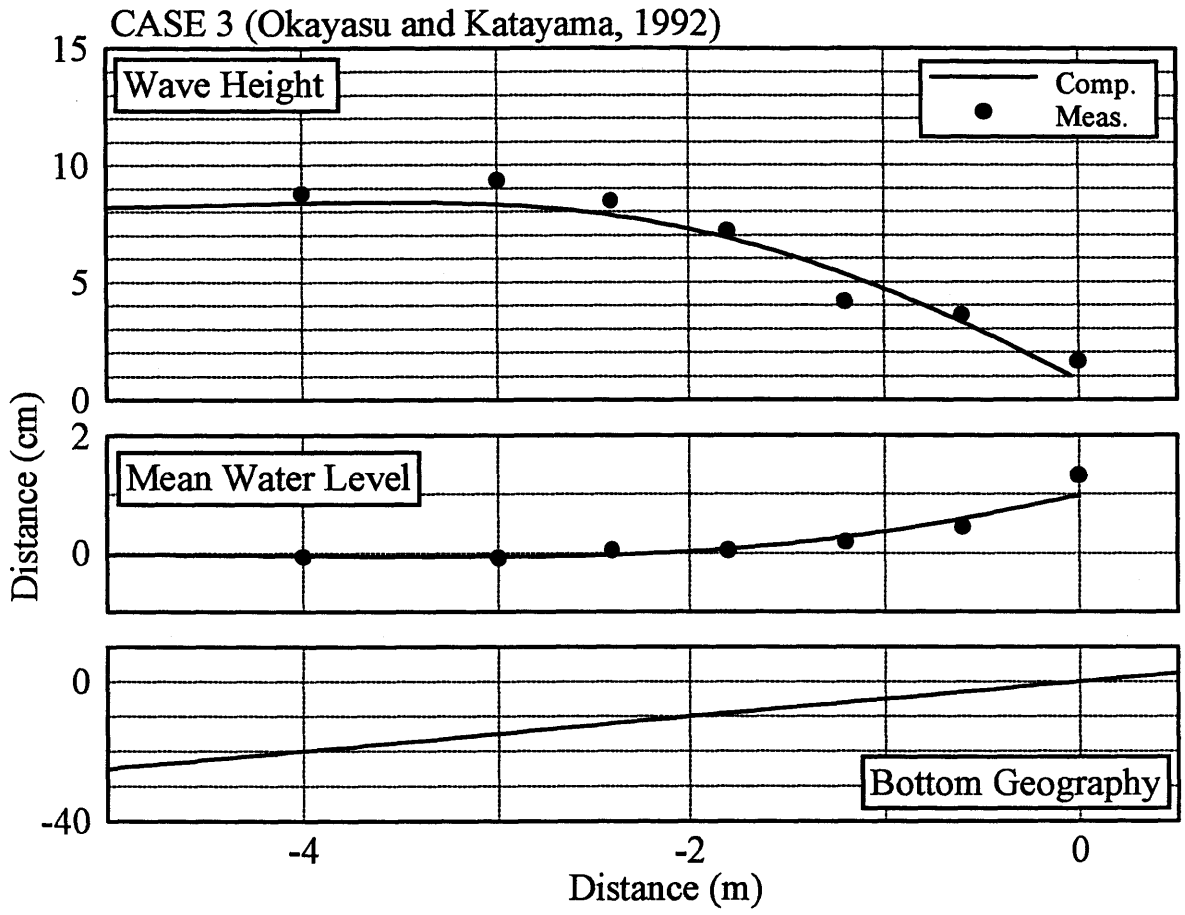

Figure-2.30 Wave heights and mean water level
(CASE 3 Okayasu and Katayama, 1992)

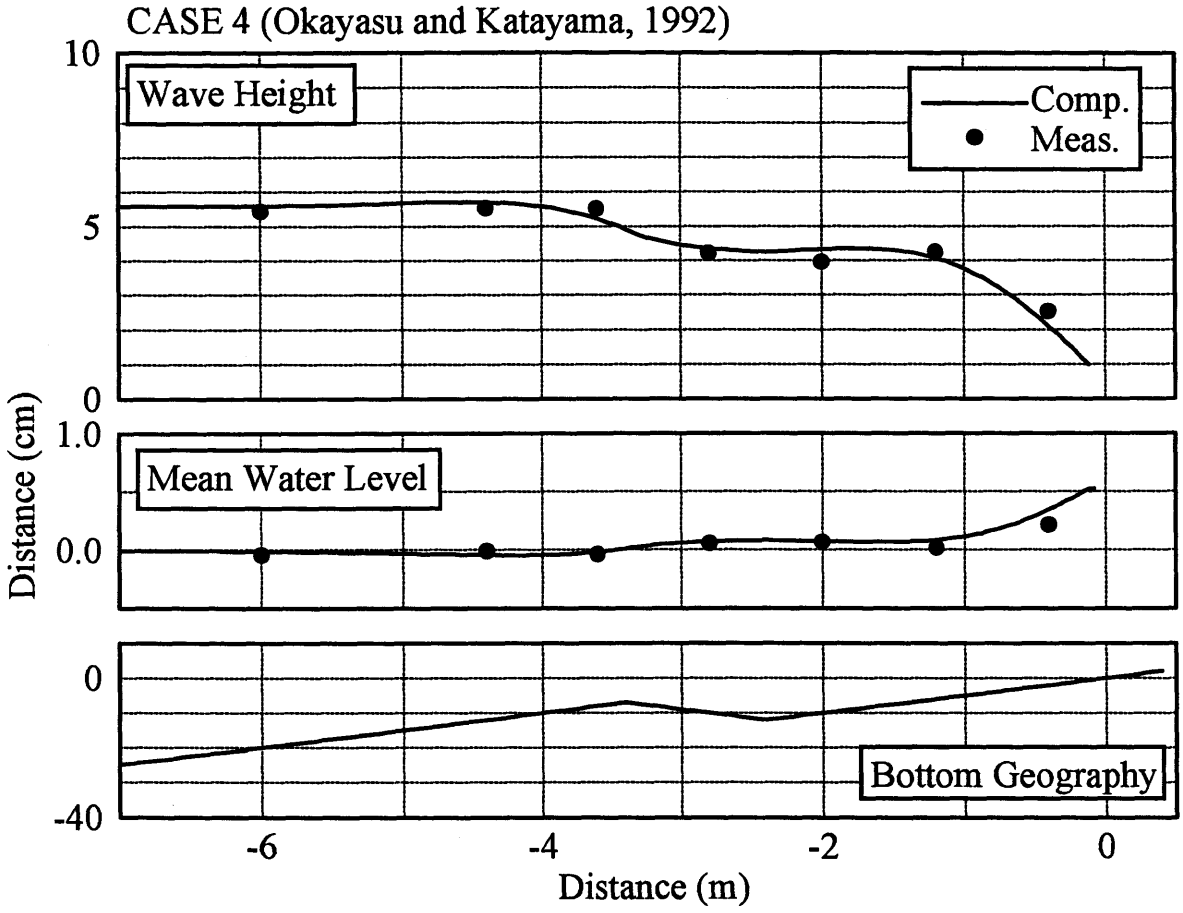

Figure-2.31 Wave heights and mean water level
(CASE 4 Okayasu and Katayama, 1992)

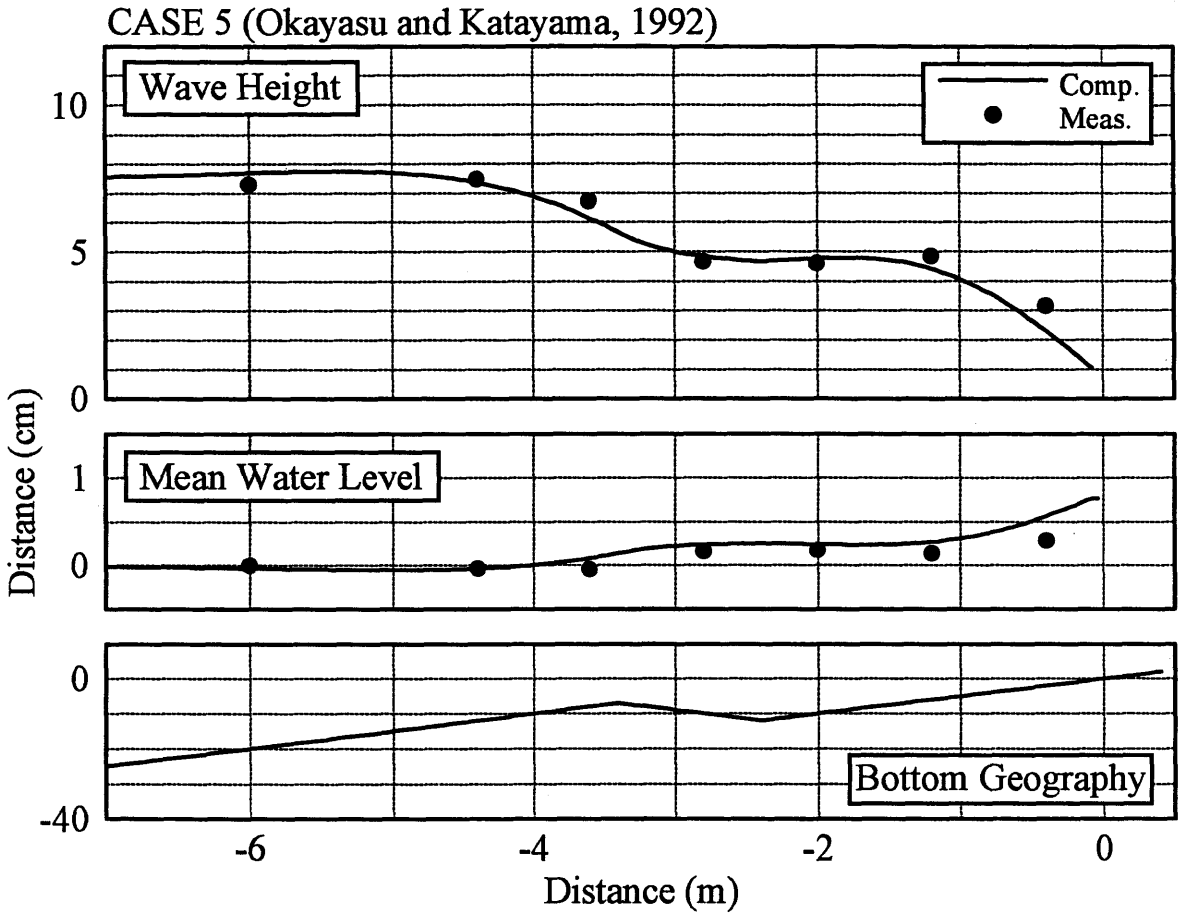

Figure-2.32 Wave heights and mean water level
(CASE 5 Okayasu and Katayama, 1992)

Chapter 3

3 Undertow Model

The wave asymmetry and the breaking wave dissipation models are complete. In this chapter, an undertow model is developed. In order to keep our models consistent, the undertow model should also be based on linear wave theory.

3.1 Physical Mechanism of the Undertow

Figure-3.1 illustrates the undertow phenomenon. The undertow is a seaward return flow, which compensates shoreward mass transport due to propagating waves. Moreover, it is generally known that the time-averaged return flow, i.e., the undertow, has a vertical variation. This phenomenon can be explained by the local mismatch of the turbulent shear stress in the water column, while depth-integrated shoreward force due to waves and wave setup are balanced. In this sense, the undertow model is developed by formulating shoreward mass transport due to waves and the vertical distribution of shoreward turbulent shear stress. Theoretical formulation of the undertow is discussed hereafter.

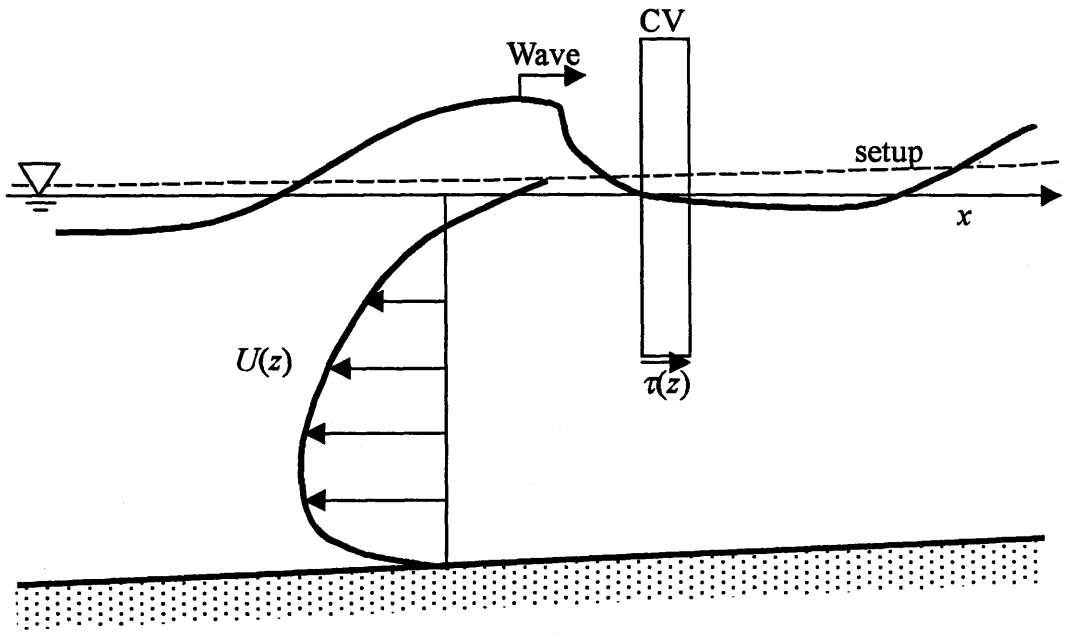

Figure-3.1 Graphical illustration of the undertow

3.2 Theoretical Formulation

Assuming irrotational incompressible flow, the Euler equation for the horizontal direction in the *x-z* plane is expressed as follows.

$$\frac{\partial u}{\partial t}+u\frac{\partial u}{\partial x}+w\frac{\partial u}{\partial z}=-\frac{1}{\rho}\frac{\partial p}{\partial x} \tag{3.1}$$

where x is a horizontal axis, z is upward with $z=0$ at the still water level, u and w are particle velocities in x and z directions, respectively. Continuity equation is

$$\frac{\partial u}{\partial x}+\frac{\partial w}{\partial z}=0 \tag{3.2}$$

Combining (3.1) and (3.2), the horizontal momentum equation is expressed as

$$\frac{\partial u}{\partial t}+\frac{\partial}{\partial x}\left(u^2\right)+\frac{\partial}{\partial z}(uw)=-\frac{1}{\rho}\frac{\partial p}{\partial x} \tag{3.3}$$

In order to take time-average of (3.3), we express each velocity component as a combination of periodic wave, undertow and turbulent fluctuation components. Each particle velocity is therefore expressed as

$$\begin{aligned} u &= \tilde{u}+u'+U \\ w &= \tilde{w}+w' \end{aligned} \tag{3.4}$$

where $\tilde{u}$ and $\tilde{w}$ are components of the periodic wave, u' and w' are components of a turbulent fluctuations and U is time-averaged undertow velocity. Assuming that time variance of turbulent fluctuation is equally distributed, time-averaged particle velocities, $\overline{u}$, $\overline{w}$, $\overline{u^2}$ and $\overline{uw}$ are expressed as follows. Here, over bar denotes the time-averaged value.

$$\begin{aligned} \overline{u} &= U \\ \overline{w} &= 0 \\ \overline{u^2} &= U^2+\overline{\tilde{u}^2}+\overline{u'^2}+2\overline{\tilde{u}u'}\approx U^2+\overline{\tilde{u}^2}+\overline{u'^2} \\ \overline{uw} &= \overline{\tilde{u}\tilde{w}}+\overline{u'w'}+\overline{\tilde{u}w'}+\overline{u'\tilde{w}}\approx \overline{u'w'} \end{aligned} \tag{3.5}$$

where $\overline{\tilde{u}\tilde{w}}$ becomes zero according to linear wave theory and it is therefore reasonably assumed that contribution of the turbulent components dominate the wave motion inside the surf zone, i.e., $\overline{\tilde{u}\tilde{w}} << \overline{u'w'}$. Taking time-average of (3.3) after substituting (3.5), the time-averaged momentum equation is expressed as

$$\frac{\partial}{\partial x}\left(U^2+\overline{\tilde{u}^2}+\overline{u'^2}\right)+\frac{\partial}{\partial z}\left(\overline{u'w'}\right)=-\frac{1}{\rho}\frac{\overline{\partial p}}{\partial x} \tag{3.6}$$

Moreover, we assume that the undertow velocity is much smaller than the wave velocity component, i.e., $U^2 << \overline{\tilde{u}^2}$ and turbulent fluctuation components are isotropic with a horizontal length scale much larger than the vertical length scale, i.e., $\frac{\partial}{\partial x}\left(\overline{u'^2}\right) << \frac{\partial}{\partial z}\left(\overline{u'w'}\right)$. Applying these

assumptions and a turbulent eddy viscosity model, (3.6) is approximated as

$$\frac{\partial}{\partial x}\overline{\left(\frac{p}{\rho}+\tilde{u}^2\right)} \cong -\frac{\partial}{\partial z}\left(\overline{u'w'}\right)=\frac{1}{\rho}\frac{\partial \tau}{\partial z}=\frac{\partial}{\partial z}\left(\nu_t \frac{\partial U}{\partial z}\right) \tag{3.7}$$

where ν_t is the turbulent eddy viscosity and τ is time-averaged shear stress at arbitrary depth. Integrating (3.7) within an arbitrary control volume, which is shown in the Figure-3.1, and applying Gauss's theorem, time-averaged turbulent shear stress at arbitrary depth, τ, is determined as follows.

$$\tau = \frac{\partial}{\partial x}\overline{\int_{-z}^{\eta}\left(p+\rho\tilde{u}^2\right)dz} \tag{3.8}$$

From the Bernoulli equation, (3.8) is represented by

$$\tau = \rho\frac{\partial}{\partial x}\overline{\int_{z}^{\eta}\left(-\frac{\partial \phi}{\partial t}+\frac{1}{2}\left(\tilde{u}^2-\tilde{w}^2\right)-g(\overline{\eta}-z)\right)dz} \tag{3.9}$$

where ϕ is a velocity potential. The right hand side of (3.9) is separated into two parts as

$$\tau = \rho\frac{\partial}{\partial x}\overline{\int_{z}^{\overline{\eta}}\left(-\frac{\partial \phi}{\partial t}+\frac{1}{2}\left(\tilde{u}^2-\tilde{w}^2\right)-g(\overline{\eta}-z)\right)dz} + \rho\frac{\partial}{\partial x}\overline{\int_{\overline{\eta}}^{\eta}\left(-\frac{\partial \phi}{\partial t}+\frac{1}{2}\left(\tilde{u}^2-\tilde{w}^2\right)-g(\overline{\eta}-z)\right)dz} \tag{3.10}$$

Utilizing Stokes second order wave theory, integration of (3.10) is performed up to the second order. Since the first term of the right hand side of (3.10) is *0*th order integrand, we keep all terms up to the second order. On the other hand, only the first order terms are kept for the second term because the integrand is the first order. From the Stokes wave theory, each value in (3.10) is expressed as follows.

$$\phi^{(1)} = \frac{a_*\omega}{k}\frac{\cosh k(h'+z)}{\sinh k(h'+\overline{\eta})}\sin(kx-\omega t)$$

$$\phi^{(2)} = +\frac{3}{8}a_*^2\frac{\cosh k(h'+z)}{\sinh^4 k(h'+\overline{\eta})}\sin 2(kx-\omega t) - U_r x - \frac{a_*^2\omega^2}{4}\frac{t}{\sinh^2 k(h'+\overline{\eta})} + O(\varepsilon^3)$$

$$\overline{\frac{\partial\phi^{(1)}}{\partial t}} = 0$$

$$\overline{\frac{\partial\phi^{(2)}}{\partial t}} = -\frac{a_*^2\omega^2}{4}\frac{1}{\sinh^2 k(h'+\overline{\eta})} + O(\varepsilon^3) = -\frac{1}{2}\left(\overline{u^2} - \overline{w^2}\right) + O(\varepsilon^3)$$

$$\overline{u^2} = \frac{a_*^2\omega^2}{2}\frac{\cosh^2 k(h'+z)}{\sinh^2 k(h'+\overline{\eta})} + O(\varepsilon^4)$$

$$\overline{w^2} = \frac{a_*^2\omega^2}{2}\frac{\sinh^2 k(h'+z)}{\sinh^2 k(h'+\overline{\eta})} + O(\varepsilon^4)$$

$$p = -\rho\frac{\partial(\phi^{(1)}+\phi^{(2)})}{\partial t} - \frac{\rho}{2}(u^2+w^2) - \rho gz + O(\varepsilon^3) = -\rho\frac{\partial\phi^{(1)}}{\partial t} - \rho gz + O(\varepsilon^2)$$

$$\frac{\partial\phi^{(1)}}{\partial t} = -g\eta + O(\varepsilon^2) \qquad at\ z = \overline{\eta}$$

Substituting these formulae into (3.10) and keeping terms up to the second order, (3.10) is rewritten as

$$\tau = \rho\frac{\partial}{\partial x}\int_z^{\overline{\eta}}\left(\widetilde{u}^2 - \widetilde{w}^2 + g(\overline{\eta}-z)\right)dz + \rho\frac{\partial}{\partial x}\overline{\int_{\overline{\eta}}^{\eta} g(\eta-\overline{\eta}+z)dz} \tag{3.11}$$

Therefore

$$\overline{\tau} = \frac{\partial}{\partial x}\left(\frac{1}{2}\rho g a_*^2\left(\frac{2k(\overline{\eta}-z)}{\sinh 2kh} + \frac{1}{2}\right) - \frac{1}{2}\rho g(\overline{\eta}-z)^2\right) \qquad (-h' < z < \overline{\eta}) \tag{3.12}$$

or

$$\overline{\tau} = \frac{\partial}{\partial x}\left(E\left(\frac{2k\overline{\eta}}{\sinh 2kh} + \frac{1}{2}\right)\right) - z\frac{\partial}{\partial x}\left(E\left(\frac{2k}{\sinh 2kh}\right)\right) - \rho g(\overline{\eta}-z)\frac{\partial\overline{\eta}}{\partial x} \tag{3.13}$$

where $E = \frac{1}{2}\rho g a_*^2$ is the wave energy and $h = h'+\overline{\eta}$ is the mean water depth. In (3.13), the first two terms are shear stresses due to the waves and the last term is due to the wave setup. Figure-3.2 illustrates the contribution of each shear stress. From (3.13), it is also seen that the shear

stress varies linearly in z. When $z=\overline{\eta}$, surface shear stress, τ_s, is estimated from (3.12) as

$$\tau_s = \frac{1}{4}\rho g \frac{\partial a_*^2}{\partial x} = \frac{1}{2}\frac{\partial E}{\partial x} \tag{3.14}$$

When there exists a bottom slope, the water column is subjected a seaward force, F_x, at $z=-h'$ due to the weight of water column itself, i.e.,

$$F_x = \rho g(h'+\overline{\eta})\frac{\partial h'}{\partial x} \tag{3.15}$$

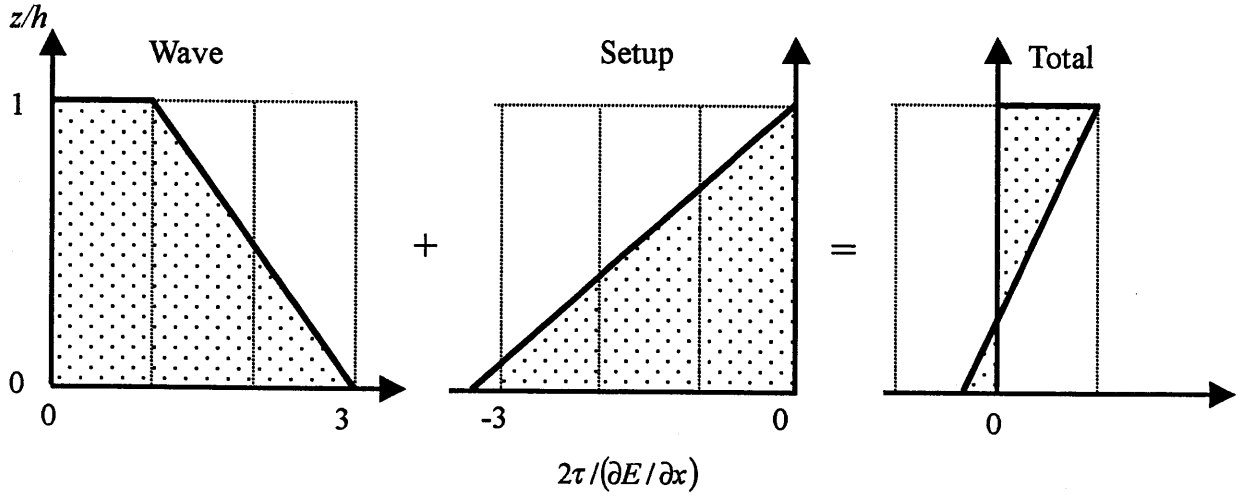

Figure-3.2 Vertical distribution of the shear stress

Combining (3.12) and (3.15), the current bottom shear stress, $\tau_c = \overline{\tau}(z=-h')$, is determined as

$$\begin{aligned}\tau_c &= \frac{\partial}{\partial x}\left(E\left(\frac{2kh}{\sinh 2kh}+\frac{1}{2}\right)\right)-\rho g h\frac{\partial(h'+\overline{\eta})}{\partial x}+\rho g h\frac{\partial h'}{\partial x} \\ &= \frac{\partial}{\partial x}S_{xx}-\rho g h\frac{\partial \overline{\eta}}{\partial x}\end{aligned} \tag{3.16}$$

where $S_{xx} = E\left(\frac{2kh}{\sinh 2kh}+\frac{1}{2}\right)$ is the radiation stress. Since both τ_c and $\frac{\partial \overline{\eta}}{\partial x}$ are still unknown variables, we need another definition of τ_c to solve the problem. This procedure is discussed in the following section. Once τ_c is specified, we can evaluate the wave setup from (3.16).

From here, we shift the origin of the z-axis to $z=0$ at the bottom in order to formulate the undertow profile. From (3.7), (3.13), (3.14) and (3.16), the relationship between undertow velocity and time-averaged shear stress is simply expressed by τ_s and τ_c as

$$\overline{\tau} = \rho \nu_t \frac{\partial U}{\partial z} = (\tau_s - \tau_c)\frac{z}{h}+\tau_c \tag{3.17}$$

According to Stive and Wind (1986), the turbulent eddy viscosity, ν_t, can be approximated fairly well as a constant, i.e., independent of z. In this study, therefore, we assume that ν_t is constant over depth and integrate equation (3.17) to obtain

$$U = \frac{\tau_s-\tau_c}{2\rho\nu_t h}z^2+\frac{\tau_c}{\rho\nu_t}z+C \tag{3.18}$$

Here, the integration constant, C, is determined by specifying the total amount of the return flow rate. Since the volume of the return flow must balance the amount transported shoreward due to mass transport,

$$U_m h = \int_0^h U dz \tag{3.19}$$

where U_m is the mean velocity of the return flow. Substituting (3.19) into (3.18), the general formula for the undertow profile is written in the following form.

$$U = \frac{\tau_s - \tau_c}{\rho \nu_t h}\left(\frac{z^2}{2} - \frac{h^2}{6}\right) + \frac{\tau_c}{\rho \nu_t}\left(z - \frac{h}{2}\right) + U_m \tag{3.20}$$

3.3 Determination of Parameters

In order to estimate the undertow profile from (3.20), we need to determine the following three unknown parameters. (1) depth-averaged return flow velocity, U_m, (2) surface shear stress, τ_s, and (3) bottom current shear stress, τ_c. In this model, all these parameters are also determined by linear wave theory. Applicability of the use of linear wave theory for the determination of these parameters is examined in Appendix B through a comparison with the Stream function method (Dean, 1965).

3.3.1 Average Return Flow

Applying first order linear wave theory, the free surface elevation, η, and horizontal particle velocity, u, are expressed as

$$\eta = a\cos\theta \tag{3.21}$$

$$u = U + \tilde{u} = U + a\omega\frac{1}{\tanh kh}\cos\theta \tag{3.22}$$

where a is wave amplitude, U is steady current velocity, ω is angular frequency, k is wave number and h is mean water depth. The time-averaged particle velocity, $\bar{u}$, is $\bar{u} = U$ under the trough level, i.e., at $z < -a$. Above the trough level, Eulerian mass transport velocity is expected.

Since particle velocity is zero above the free surface, the time-averaged particle velocity above the trough level ($z > -a$) is expressed as

$$\bar{u} = \frac{1}{2\pi}\int_{-\theta_w}^{\theta_w}(U + u_w\cos\theta)d\theta = \frac{1}{\pi}(U\theta_w + u_w\sin\theta_w) \tag{3.23}$$

where

$$\cos\theta_w = \frac{z}{a} \quad (-a \le z \le a,\ 0 \le \theta \le \pi) \tag{3.24}$$

Figure-3.3 shows the vertical distribution of the time-averaged horizontal particle velocity. From the figure, it is seen that the time-averaged steady current above the trough level is symmetrical around the mean water level.

Assuming zero mass transport, depth integration of (3.23) determines return flow velocity, U, as

$$\begin{aligned}&\int_{-h}^{a}\frac{1}{\pi}(U\theta_w + u_w\sin\theta_w)dz = 0\\ &\rightarrow Uh = -\frac{1}{\pi}\int_{-a}^{a}u_w\sqrt{1-(z/a)^2}\,dz = \frac{2}{\pi}\int_{0}^{\pi/2}u_w\sin^2\theta d\theta = -\frac{1}{2}au_w\end{aligned} \tag{3.25}$$

Therefore, depth and time-averaged return flow velocity due to wave, U_w, is

$$U_w = -\frac{au_w}{2h} = -\frac{a^2\omega}{2h\tanh kh} = -\frac{E}{\rho hC} \tag{3.26}$$

where C is the wave phase velocity and E is the wave energy.

It has been proposed that there will be an increase of mass transport within the surf zone due to effects of the surface roller. Stive and Wind(1986) proposed an empirical equation to obtain the return flow velocity.

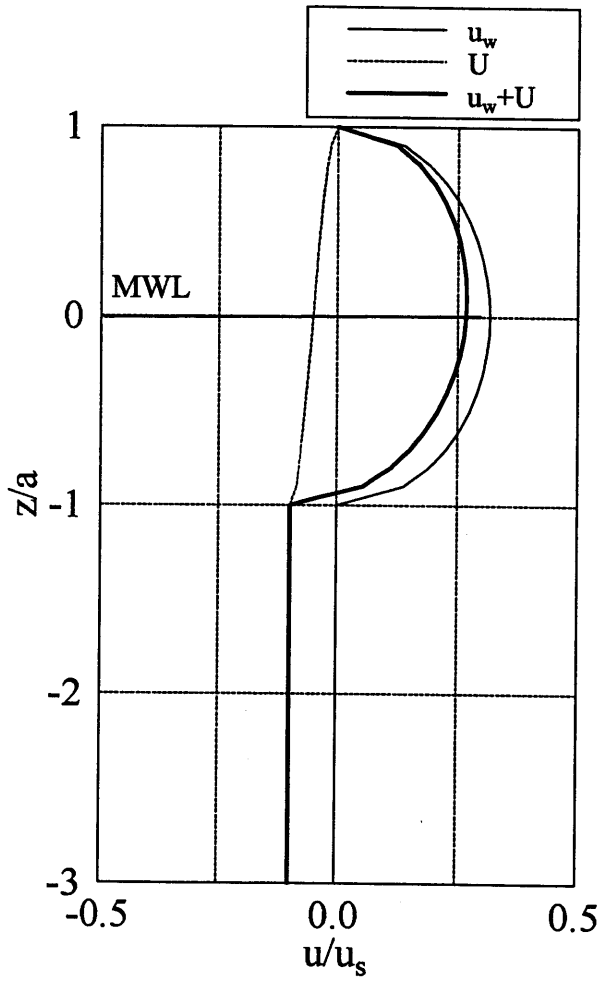

Figure-3.3 Vertical distribution of time-averaged horizontal velocity

$$U_w = -\frac{1}{10}\sqrt{gh}\frac{H}{h} \tag{3.27}$$

The result corresponds closely to the solution of linear wave theory (3.26) when $H=0.8h$. Since their empirical equation is based on measured wave heights, wave height in (3.27) should be non-linear wave heights. Svendsen(1984) presented the return flow velocity as

$$U_w = -C\left(\frac{H}{h}\right)^2\left(B_0 + \frac{S}{H^2}\frac{h}{L}\right) \tag{3.28}$$

where C is the wave phase velocity, $B_0=0.08$ is a shape factor and S is the area of the roller estimated to be $0.9H^2$. Since his model is also calibrated with measured wave heights, non-linear wave heights should be used for estimation. The second term of (3.28) accounts for a surface roller effect, which should be added only inside the surf-zone. These models are compared later.

3.3.2 Surface Shear Stress

The surface shear stress due to waves, τ_s, is also estimated by linear wave theory. As discussed in the derivation of theoretical undertow profile model, the surface shear stress is determined by linear wave theory as

$$\tau_s = -\frac{1}{2}\frac{\partial E}{\partial x} \tag{3.29}$$

Similar to the return flow velocity, it is also expected that there will be a greater shear at the surface of the water inside the surf zone than there would be outside the surf zone. Svendsen(1984) proposed following semi-empirical equation to obtain the surface shear.

$$\tau_s = -\left(\frac{1}{16} + \frac{S}{H^2}\frac{h}{L}\right)\rho g \frac{\partial H^2}{\partial x} \tag{3.30}$$

Here the second term expresses the effect of the surface roller and S is the time-averaged area of the surface roller. Similar to return flow velocity, non-linear wave heights should be used in (3.30) since calibration was done with measured wave heights.

3.3.3 Bottom Current Shear Stress

The bottom current shear stress can be determined by introducing wave-current bottom boundary layer mechanics. According to the combined wave-current boundary layer model presented by Grant and Madsen(1986), boundary layer flow is determined as

$$u = \frac{1}{\kappa}\frac{u_{*c}^2}{u_{*m}} \ln\left(\frac{z}{z_0}\right) \qquad (z \le \delta_{cw}) \tag{3.31}$$

where u_{*c} is the bottom current shear velocity, u_{*m} is the maximum combined wave-current shear velocity, κ is von Karman's constant (κ=0.4), z_0 is determined as $z_0=k_N/30$ where k_N is the equivalent Nikuradse sand grain roughness and δ_{cw} is the thickness of the wave bottom boundary layer. Here k_N is taken as the diameter of the sand grain for rough turbulent flow or as $k_N = 3.3\nu / u_{*m}$ for smooth turbulent flow. The bottom current shear stress, τ_c, can be determined by matching condition of the boundary layer flow velocity (3.31) and the free stream flow velocity (3.20) at the edge of the wave boundary layer, i.e., at $z=\delta_{cw}$. Substituting $u_{*c} = \sqrt{\tau_c / \rho}$ into (3.31), τ_c is estimated from (3.20) and (3.31) by the following formula.

$$\tau_c = \frac{U_m + \frac{\tau_s}{\rho \nu_t}\left(\frac{\delta_{cw}^2}{2h} - \frac{h}{6}\right)}{\frac{1}{\kappa \rho u_{*m}} \ln\left(\frac{\delta_{cw}}{z_0}\right) + \frac{1}{\rho \nu_t}\left(\frac{h}{3} - \delta_{cw} + \frac{\delta_{cw}^2}{2h}\right)} \tag{3.32}$$

Since u_{*m} and δ_{cw} are still unknown and these parameters are dependent on τ_c, (3.32) must be solved by numerical iteration. The procedure of this computation is as follows.

According to Madsen(1994), the relationship between u_{*w} and u_{*m} is expressed as

$$u_{*m}^2 = C_\mu u_{*wm}^2 \tag{3.33}$$

where

$$C_\mu = \left(1 + 2\mu|\cos\phi_{wc}| + \mu^2\right)^{1/2}, \tag{3.34}$$

$$\mu = \frac{\tau_c}{\tau_{wm}} = \left(\frac{u_{*c}}{u_{wm}}\right)^2 \tag{3.35}$$

and ϕ_{wc} is the angle between waves and current, i.e., $\phi_{wc}=\pi$ when waves are normally incident on the parallel beach and the undertow is in the offshore direction. The maximum wave shear velocity, u_{*wm}, is expressed as

$$u_{*wm}^2 = \frac{1}{2} f_{cw} u_{bm}^2 \tag{3.36}$$

where f_{cw} is a wave friction factor and u_{bm} is the maximum near-bottom orbital velocity. Moreover, the boundary layer thickness, δ_{cw}, is then given by following formula (Madsen and Salles, 1998).

$$\delta_{cw} = \frac{A \kappa u_{*m}}{\omega} \tag{3.37}$$

with

$$A = \exp\left(2.96\left(C_\mu A_{bm}/k_N\right)^{-0.071} - 1.45\right) \tag{3.38}$$

where $A_{bm} = u_{bm}/\omega$ is the maximum bottom excursion amplitude and ω is the angular frequency. As seen in the equation (3.38), δ_{cw} is also a function of C_μ, i.e., a function of τ_c. The wave friction factor, f_{cw}, is determined through the following procedures.

1. Assuming rough turbulent flow, estimate a friction factor by the following explicit formula (Madsen, 1994).

$$f_{cw} = \begin{cases} C_\mu \exp\left[7.02\left(C_\mu A_{bm}/k_N\right)^{-0.078} - 8.82\right] & for\ \ 0.2 < \left(C_\mu A_{bm}/k_N\right) < 10^2 \\ C_\mu \exp\left[5.61\left(C_\mu A_{bm}/k_N\right)^{-0.109} - 7.30\right] & for\ \ 10^2 < \left(C_\mu A_{bm}/k_N\right) < 10^4 \\ C_\mu \exp\left[5.50\left(C_\mu A_{bm}/k_N\right)^{-0.120} - 7.02\right] & for\ \ 10^4 < \left(C_\mu A_{bm}/k_N\right) < 10^6 \end{cases} \tag{3.39}$$

These explicit approximation formulae are based on the exact solution obtained by Madsen(1994). When $A_{bm}/k_N > 10^6$, the wave friction factor is estimated by solving the following approximate formula numerically.

$$\frac{1}{4\sqrt{f_w/C_\mu}} + \log_{10}\frac{1}{4\sqrt{f_w/C_\mu}} = \log_{10}\frac{C_\mu A_{bm}}{k_N} - 0.17 \tag{3.40}$$

2. Under the assumption of rough turbulent flow, the maximum wave shear velocity, u_{*wm}, is estimated as

$$u_{*wm} = \sqrt{\frac{f_w}{2}}u_b \tag{3.41}$$

3. Check if our initial assumption of rough turbulent flow is valid by estimating the value of $k_N u_{*wm}/\nu$ where ν is kinematic viscosity (=10^{-6}m^2/s for sea water). If $k_N u_{*wm}/\nu > 3.3$, the flow is the rough turbulent. If $k_N u_{*wm}/\nu < 3.3$, the flow is smooth turbulent. Re-estimate a

friction factor by replacing the equivalent Nikuradse sand grain size by $k_N = 3.3\nu / u_{*wm}$.

5. The wave friction factor for the laminar flow is determined as

$$f_{cw} = \frac{2}{\sqrt{RE}} = 2\sqrt{\frac{\nu}{u_{bm} A_{bm}}} \tag{3.42}$$

Comparing this friction factor with the one determined for turbulent flow condition, we should apply the larger value for our wave friction factor.

All the variables except eddy viscosity are now determined. Evaluation of the eddy viscosity is discussed later. As noted previously, u_{*m} and τ_c are dependent on each other and iterative computation is therefore required in order to determine τ_c, δ_{cw} and u_{*m}. The iteration procedures are summarized as follows.

1. As initial value, assume $\tau_c << \tau_{wm}$ and take $\mu \approx 0$.
2. Estimate f_{cw} from (3.39)
3. Using present μ, estimate u_{*m} from (3.33) and δ_{cw} from (3.37).
4. With u_{*m} and δ_{cw}, evaluate τ_c from (3.32).
5. Evaluate new μ^{new} by (3.35) and compare with previously used μ. If there is considerable difference between these two values, take $\mu=\mu^{new}$ and go back 2 to iterate the same procedure.

3.3.4 Eddy viscosity

According to Stive and Wind(1986), the depth-independent eddy viscosity, ν_t, is empirically given as

$$\nu_t = 0.01Ch \tag{3.43}$$

Stive and Wind (1986) showed that this empirical eddy viscosity model gives reasonable undertow profiles inside the surf zone with their model. As seen in (3.43), however, this model can not take into account the difference of the wave heights. In other words, (3.43) overestimates the eddy viscosity when wave height is smaller and underestimate when wave height is larger since (3.43) is only a function of water depth and wave period. In this study, we therefore introduce a semi-empirical model based on Prandtl's second hypothesis.

According to Prandtl's second hypothesis, eddy viscosity is determined as

$$\nu_t \propto |u_{\max} - u_{\min}|\ell \tag{3.44}$$

where u_{max}/u_{min} is maximum/minimum fluid velocity and ℓ is a thickness of the turbulent flow. Applying this hypothesis to the undertow problem, the thickness scale can be represented by the water depth, i.e.,

$$\ell \approx h \tag{3.45}$$

The scale of the difference of fluid velocity can be represented from (3.20) as

$$u_{\max} - u_{\min} \approx U|_{z=0} - U|_{z=h} \approx \frac{(\tau_s + \tau_c)h}{2\rho\nu_t} \tag{3.46}$$

Substituting (3.45) and (3.46) into (3.44), general expression of our eddy viscosity is given as

$$\nu_t = k_1\sqrt{\frac{|\tau_s + \tau_c|}{\rho}}h \tag{3.47}$$

where k_1 is an empirical constant and k_1=0.3 was used in this study through comparison with experimental data. For practical convenience, we simply approximate (3.47) as

$$\nu_t = k_1 \sqrt{\frac{\max(|\tau_s|, |\tau_c|)}{\rho}} h \tag{3.48}$$

When the surface shear stress, τ_s, dominates the bottom current shear stress, τ_c, as often occurs inside the surf zone, the eddy viscosity in (3.48) can be determined explicitly because τ_s is already determined a parameter. Otherwise, numerical iteration is required because both τ_c and ν_t are now depending on each other. The applicability of this model is examined later.

3.3.5 Examination of parameters

In this section, we examine the applicability of our modeling of return flow velocity, surface shear stress and turbulent eddy viscosity through comparison with other models and experimental data obtained by Cox et al. (1995). Experimental conditions are the same as CASE1 presented in Section 2.3.2. In this computation, the return flow velocity, surface shear stress and turbulent eddy viscosity are estimated from (3.14), (3.29) and (3.48) respectively by using linear wave heights computed by our wave model. Moreover, the return flow velocities proposed by Stive and Wind(1986) and by Svendsen (1984), the surface shear stress by Svendsen (1984) and the turbulent eddy viscosity by Stive and Wind(1986), were estimated from (3.27), (3.28), (3.30) and (3.43), respectively, by using non-linear wave heights computed by our wave model.

Figure-3.4 shows the comparison of the depth-averaged return flow velocity (3.26), surface shear stress (3.29) and turbulent eddy viscosity (3.48) computed by present model and other models with measured data. From the figure, it is seen that return flow velocity increases

immediately after the wave breaking despite the fact that wave heights start to decrease. The return flow velocity computed by linear wave theory starts to decrease at the breaking point. Therefore, the linear wave theory underestimates return flow velocities inside the surf-zone although its prediction outside the surf-zone is very close to measured data. Stive and Wind's (1986) model predicts return flow velocities fairly well inside the surf-zone but clearly overestimates those velocities outside the surf-zone. These results suggest that linear wave theory should be applicable if waves are not breaking and that different phenomena other than wave actions should occur inside the surf-zone. Svendsen's (1984) model explains this excess amount of mass transport inside the surf-zone by introducing the surface roller model. As seen in the figure, Svendsen's (1984) model surely estimates the increase of return flow velocity inside the surf-zone. However, his model estimates too large a return flow velocity right after the breaking point since his model is calibrated to be appropriate only in the inner surf-zone. This also gives a large mismatch of return flow velocity at the breaking point.

The surface shear stress computed by linear wave theory is smaller than Svendsen's (1986) model. Since Svendsen's (1984) model is expected to be valid in the inner surf-zone, we can conclude that linear wave theory underestimates surface shear stress in the inner surf-zone and therefore, we should also introduce an additional model, which explains this excess shear stress. Moreover, it is also seen that both models have a peak shoreward surface shear stress right after the breaking point. This result cannot explain the observed facts, which will be presented later, that the peak shoreward shear stress occurs inside the surf-zone a certain distance away from the breaking point and the surface shear stress right after the breaking point tends to act in the seaward direction.

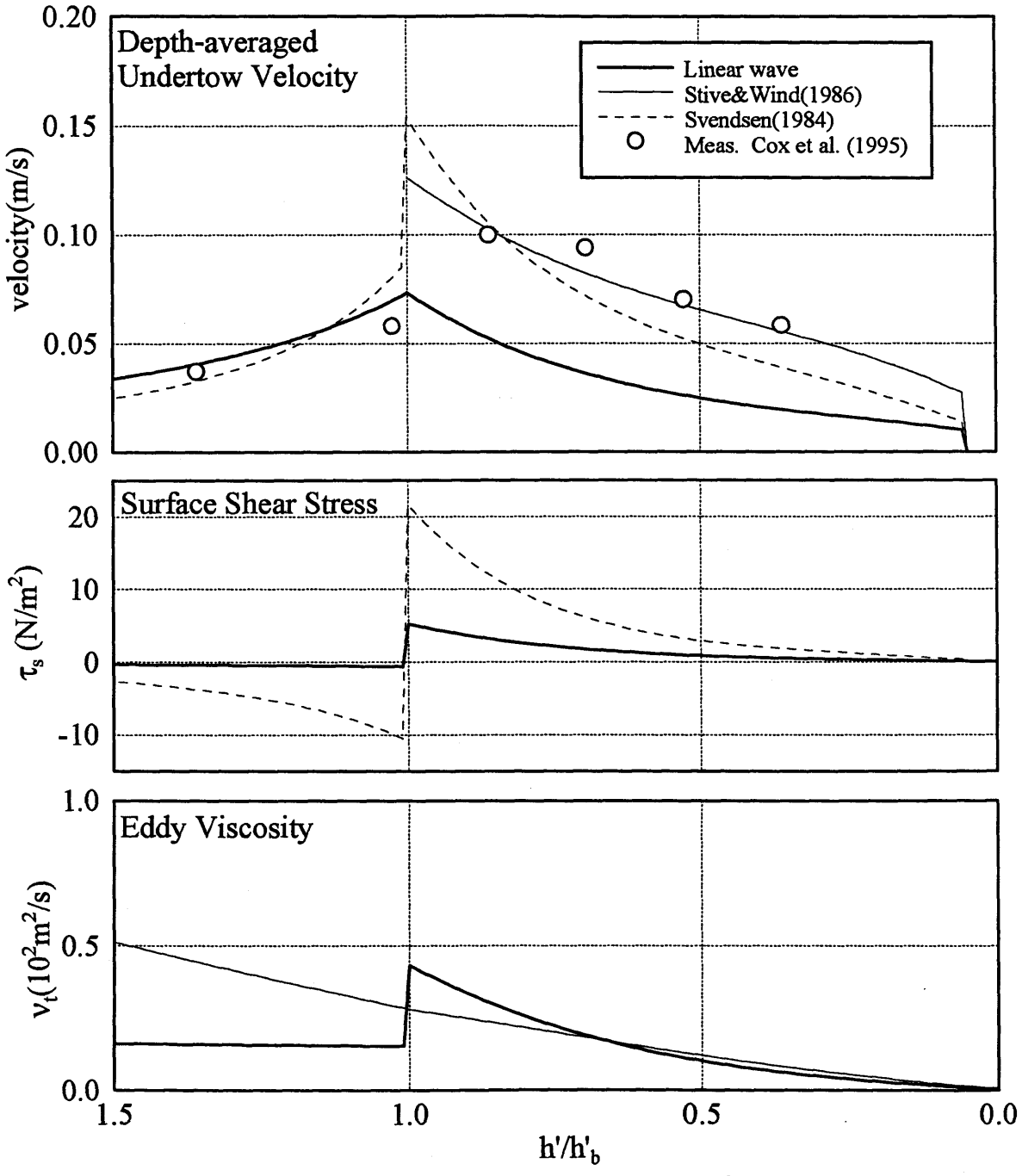

Figure-3.4 Computed parameters with measured data

3.4 Surface Roller Model

In the Section 3.2.5, it was seen that the mass transport rate evaluated by linear wave theory was too small inside the surf zone while these values agreed fairly well with measured data outside the surf zone. This obviously suggests that we have an additional phenomenon, which causes excess mass transport inside the surf zone.

As discussed before, Svendsen(1984) explained this excess amount of mass transport and the surface shear stress by introducing the effect of the surface roller. His model, however, estimates too large a surface shear stress in the outer surf-zone because his surface roller model is empirically developed from experimental data that are representative for in the inner surf zone.

Okayasu et al. (1990) pointed out this disadvantage and developed a new undertow model with the assumption that dissipated wave energy due to breaking is transferred to both the surface roller energy and turbulent energy. It is also assumed that dissipated wave energy at an arbitrary local point is evenly transferred to the turbulent energy through a certain distance, which is related to the local depth. The surface roller energy is then determined as an integration of the remaining dissipated wave energy, which is caused by wave breaking but not yet transferred to turbulent energy. Although their model estimates total volume of the return flow throughout the surf-zone fairly well, their model still overestimates the surface shear stress near the breaking point. Since their shear stress model depends only on energy dissipation rate, their surface shear stress always acts in shoreward direction, which cannot explain the observation that the surface shear stress near the breaking point tends to act in the seaward direction. This feature is shown later by the experimental data. Moreover, because of the complexity of their model, it is difficult to apply this model to random wave conditions.

Dally and Brown (1995) proposed a model to estimate the area of the surface roller and the mass transport rate based on similar concepts to those of Okayasu et al. (1990). In their model, it is assumed that the rate of dissipated turbulent energy is proportional to the amount of surface roller energy. Although the applicability of their model is proved only for the mass transport rate under regular wave conditions, it is expected that this concept is also applicable to the surface shear estimation. Because of the simplicity of this model, it is also expected that we can extend it to random wave problems.

In this study, therefore, we improve the Dally and Brown's (1995) model and develop a new surface roller model, which is applicable over the entire surf-zone and also applicable for random waves.

3.4.1 Theoretical Formulation of the Surface Roller Energy

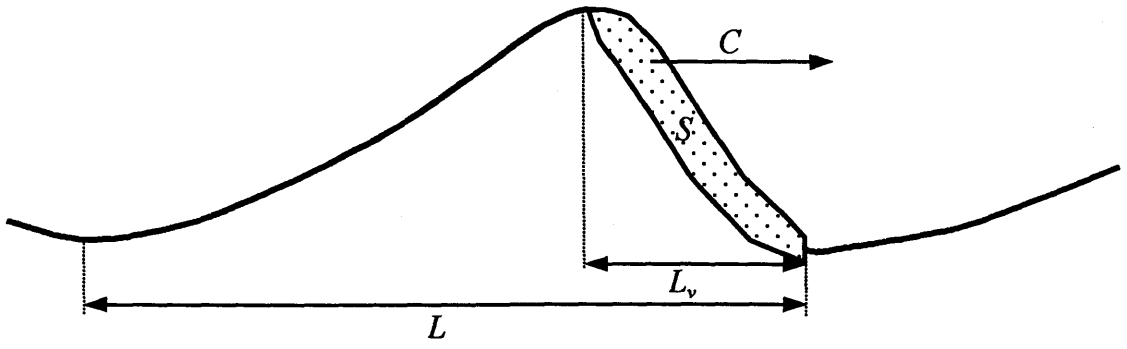

Figure-3.5 Sketch of the surface roller

Figure-3.5 illustrates the surface roller. In the figure, S is the area of the surface roller, L_v is a horizontal length of the surface roller, L is the wavelength. In this model, we assume that a particle in the surface roller moves horizontally with the phase velocity, C. Assuming that the thickness of the surface roller, d_v, is uniform, i.e., $d_v=S/L_v$, time-averaged total energy per unit area of the surface roller, E_v, is determined as

$$E_v = \frac{1}{T}\int_0^T \frac{1}{2}\rho d_v C^2 dt = \frac{1}{T}\int_0^{TL_v/L} \rho \frac{S}{2L_v} C^2 dt = \rho \frac{SC}{2T} \tag{3.49}$$

Here, the potential energy of the surface roller is neglected with the assumption that the surface roller is uniformly distributed in vertical direction around the mean water level and should have little potential energy change compared with the change in kinetic energy. Now, we assume that, from the total breaking wave dissipation energy, only the potential wave energy should be transferred to the surface roller energy since there should be no way for the surface roller to obtain kinetic energy which exists in the water column. The surface roller energy should then be dissipated to turbulent energy gradually. In the linear wave theory, this assumption implies that only half of the breaking wave dissipation energy is transferred to surface roller energy while the other half is dissipated separately from the surface roller. Based on these assumptions, energy flux conservation law leads

$$\frac{1}{2}\frac{\partial}{\partial x}(EC_g) + \frac{\partial}{\partial x}(E_v C) = D_b \tag{3.50}$$

where D_b is the dissipation rate per unit area from the surface roller to turbulent energy. Since the first term of (3.50), which denotes the dissipation rate of the wave energy, is already estimated by our breaking wave dissipation model, we can estimate surface roller energy once D_b is specified. From the assumption, D_b should be a function of surface roller energy. Assuming therefore that

D_b should be proportional to the surface roller energy flux, equation (3.50) is represented as

$$\frac{1}{2}\frac{\partial}{\partial x}(EC_g)+\frac{\partial}{\partial x}(E_v C)=-\alpha\frac{E_v C}{h} \tag{3.51}$$

Here, α is a dimensionless parameter and the mean water depth, h, is added to match up the dimensions. This formulation is surely consistent with our breaking wave dissipation model. Substituting (3.49) into (3.51), energy balance equation is represented in terms of the area of the surface roller as

$$\frac{1}{2}\frac{\partial}{\partial x}(EC_g)+\frac{\partial}{\partial x}\left(\rho\frac{SC^2}{2T}\right)=-\alpha\rho\frac{SC^2}{2Th} \tag{3.52}$$

If applying $C=\sqrt{gh}$ to (3.52) with the assumption of shallow water linear wave theory, equation (3.51) becomes equivalent to the Dally and Brown (1995) model except that the first term of the left-hand side of (3.52) is not divided by 2 in the Dally and Brown (1995) model. In other words, they assumed that all the dissipated wave energy is transferred to the surface roller energy while we assumed only the potential energy to be transferred to the surface roller. According to Dally and Brown (1995), the constant parameter, α=0.2, gives the reasonable results in terms of the prediction of the mass transport rate due to the roller, which is discussed later.

3.4.2 Determination of α

Although Dally and Brown (1995) applied a single constant value of α, it is expected that this α should also be a function of the bottom slope because the proportionality coefficient of our breaking wave energy dissipation model is determined to be a function of the bottom slope. In this section, we develop a semi-empirical formula to determine an appropriate value of α.

According to Svendsen (1984), the area of the surface roller, S, in the inner surf-zone becomes proportional to a square of the local wave height, i.e.,

$$S = A_r H^2 \tag{3.53}$$

Here A_r is a proportionality constant and the local wave height, H, should be the non-linear wave height since this expression is obtained from the experimental data. Although Svendsen(1984) proposed $A_r=0.9$, the larger values of A_r up to the order of 10 have been proposed through other experimental and field data(e.g., Okayasu et al., 1987; and Hiruta and Hattori, 1999). For example, Okayasu et al. (1987) proposed $A_r=2.0$ based on their experiments. As seen in the Figure-3.4, Svendsen's (1984) model underestimates the depth-averaged return flow velocity inside the inner surf-zone. This also suggests that A_r should be larger than 0.9. Moreover, it is expected that the value of A_r should be a function of the bottom slope although Svendsen (1984) applied the single constant value for A_r. For example, the surface roller area must approach zero on the no-slope depth condition because all the surface roller energy should be dissipated to turbulent when the breaking wave heights approach its recovery wave heights and no dissipated wave energy is supplied to the surface-roller. In this study, therefore, we determine the surface roller area in the inner surf-zone as

$$S = B \tan\beta H_*^2 \tag{3.54}$$

where the equivalent linear wave height is used in order to keep the consistency of our model. The empirical constant, B, is determined as $B=140$, which gives $S = 4H_*^2$ when $\tan\beta=1/35$. Since we are using the equivalent linear wave heights, proportionality constant should be larger than A_r. The validity of this B value is examined later.

Utilizing (3.54), we determine the value of α based on the following concepts. First, we assume that, on the uniformly sloping bed, the area of the surface roller approaches (3.54) as equivalent linear wave heights approach $H_*=\gamma_s h$. Substituting these conditions into (3. 52), we get

$$\frac{1}{2}\frac{\partial}{\partial x}\left(\frac{1}{8}\rho g\gamma_s^2 h^2 C_g\right)+\frac{\partial}{\partial x}\left(\rho\frac{B\tan\beta\gamma_s^2 h^2}{2T}C^2\right)=-\alpha\rho\frac{B\tan\beta\gamma_s^2 h}{2T}C^2 \tag{3.55}$$

As discussed before, $\frac{\partial\gamma_s}{\partial x}=0$. Note that (3.55) is still valid for non-slope condition because all the terms in (3.55) becomes zero when tanβ=0. Applying shallow water linear wave theory, i.e., $C=C_g=\sqrt{gh}$, (3.55) is simplified as follows.

$$\frac{5}{32}(gh)^{\frac{3}{2}}\gamma_s^2\frac{\partial h}{\partial x}+\frac{3gB\tan\beta\gamma_s^2 h^2}{2T}\frac{\partial h}{\partial x}=-\alpha\frac{gB\tan\beta\gamma_s^2 h^2}{2T} \tag{3.56}$$

As derived in (2.37), $\frac{\partial h}{\partial x}$ is determined from Longuet-Higgins (1963) as

$$\frac{\partial h}{\partial x}=-\frac{8}{8+3\gamma_s^2}\tan\beta \tag{3.57}$$

From (3.56) and (3.57), α is finally determined as

$$\alpha=\frac{8}{8+3\gamma_s^2}\left(\frac{5T}{16B}\sqrt{\frac{g}{h}}+3\tan\beta\right) \tag{3.58}$$

3.4.3 Return Flow Velocity due to the Surface Roller

Since it is assumed that the total volume, S, of the surface roller moves for one wave period, depth-averaged return flow velocity, U_v, is determined as

$$U_v=-\frac{S}{T}\frac{1}{h}=\frac{2}{\rho Ch}E_v \tag{3.59}$$

3.4.4 Shear Stress due to the Surface Roller

Similar to the wave shear stress model, the shear stress due to the surface roller is also determined by integrating the momentum equation in an arbitrary control volume. Since the surface roller is always located above the free surface, it is reasonable to assume that the pressure in the surface roller is identical to an atmospheric pressure and therefore constant in the x-direction. Moreover, the shear stress due to the surface roller becomes constant in depth below the lower edge of the roller because there should be no surface roller below the free surface. The time-averaged shear stress due to the surface roller is therefore expressed as

$$\tau_{sv} = \frac{1}{T}\frac{\partial}{\partial x}\int_0^T \rho d_v C^2 dt = \frac{\partial}{\partial x}\frac{\rho SC}{T} = \frac{\partial}{\partial x} 2E_v \tag{3.60}$$

This expression is identical to the Svendsen's (1984) model, i.e., the second term of (3.28). The significant difference from his model is the variation of the surface roller area. In Svendsen's model, the surface shear stress due to the surface roller is always negative, i.e., acts in the shore-ward direction since the surface roller area always decrease in the surf-zone as wave dissipates. In the present model, on the other hand, (3.60) becomes positive, i.e., τ_{sv} acts in the sea-ward direction, right after the breaking because the surface roller grows when the waves start to break. This feature will be shown and discussed in the Section 3.6.

3.4.5 Model Application for Numerical Computation

The theoretical formulation of the surface roller model is now complete. In order to estimate the surface roller energy for arbitrary waves and bottom conditions from (3.51), numerical computation is required. In this section, we discuss the methodology of the numerical

solution of (3.51).

Applying trapezoidal rule, (3.51) is discretized as follows.

$$\frac{E_{i+1}C_{g,i+1}-E_iC_{g,i}}{2\Delta x}+\frac{E_{v,i+1}C_{i+1}-E_{v,i}C_i}{\Delta x}=-\frac{\alpha_{i+1/2}}{2}\left(\frac{E_{v,i+1}C_{i+1}}{h_{i+1}}+\frac{E_{v,i}C_i}{h_i}\right) \tag{3.61}$$

Here the subscript, i, denotes the grid number in the shore-ward direction. Note that α is also a function of mean water depth but a known parameter. From (3.61), the only unknown variable, $E_{v,i+1}$, is estimated explicitly as

$$E_{v,i+1}=\frac{E_{v,i}C_i\left(1-\frac{\alpha_{i+1/2}\Delta x}{2h_i}\right)-\frac{1}{2}\left(E_{i+1}C_{g,i+1}-E_iC_{g,i}\right)}{C_{i+1}\left(1+\frac{\alpha_{i+1/2}\Delta x}{2h_{i+1}}\right)} \tag{3.62}$$

The boundary condition is given as zero surface roller energy outside the surf-zone, i.e., at the offshore boundary.

3.4.6 Modification of the Undertow Model

Taking the surface roller effect into account, the determinations of time and depth-averaged return flow velocity and the surface shear stress are modified from our original undertow model. Since the shear stress due to the surface roller is constant in depth, the assumption of the vertical linear distribution of the shear stress, i.e., (3.17) is still valid. The only change in the formulation of our undertow model is, therefore, the determinations of return flow velocity, U_m, and surface shear stress, τ_s. Combining linear wave model and the presented surface roller model, U_m and τ_s are determined as follows.

$$U_m = \frac{E}{\rho h C} + \frac{2E_v}{\rho h C} \tag{3.63}$$

$$\tau_s = \frac{\partial}{\partial x}\left(\frac{1}{2}E + 2E_v\right) \tag{3.64}$$

3.5 Model Extension for Random Wave Problem

As seen in (3.63) and (3.64), both the return flow velocity and the surface shear stress are proportional to wave and surface roller energies. Moreover, statistically averaged surface roller energy for random wave condition should be simply estimated from (3.51) if the wave energy dissipation rate, the first term of (3.51), is also determined as statistically averaged for the random wave condition. It is therefore reasonable to apply our undertow model to the random wave problem by simply taking rms-wave height as a regular single wave height. The applicability of this extension is examined later.

3.6 Model Examination

3.6.1 Area of the Surface Roller

Figure-3.6 shows the area of the surface roller as a function of still water depth. In the figure, dotted lines are Svendsen's (1984) expression (3.53) for the surface roller area. It is seen that the present model surely approaches $S = 4H_*^2$ as assumed when developing the model. Here H_* is the equivalent linear wave height and this assumption of $S = 4H_*^2$ appears reasonable because the estimated area is close to $S = 2H^2$ in the inner surf-zone, which is the relationship proposed by Okayasu, et al. (1987) where H is the non-linear wave height.

From the figure, it is seen that the surface roller estimated by the present model starts to grow at the breaking point and decrease after reaching its peak value inside the surf-zone. This feature explains a continuous increase of return flow velocity and the surface roller energy in the outer surf-zone. This increase of the surface roller energy causes the seaward surface shear stress right after the breaking point.

3.6.2 Examination of Parameters

Figure 3.7 shows the same graph as Figure 3.5 with the return flow velocity, surface shear stress and turbulent eddy viscosity estimated by the present model added. Although the return flow velocity is underestimated right after the breaking point, it is seen that our model predicts reasonable return flow velocities for the entire region. As discussed before, it is also seen that the present model estimates the sea-ward surface shear stress right after the breaking point while other models predicts shore-ward shear stress for the entire surf-zone. As shown later in the Section 3.6.3, it is observed that the surface shear stress acts in the sea-ward direction right after the breaking point. In this sense, therefore, this feature is one of improvements of the present model over other models. Moreover, our model agrees well with Svendsen's (1984) model in the inner surf-zone, where the validity of his model has already been confirmed. Turbulent eddy viscosity is estimated within the same order of Stive and Wind(1986) model. Since a combination of the shear stress and turbulent eddy viscosity determines the undertow profile, the validity of the turbulent eddy viscosity should be examined by comparing computed undertow profiles with measured data.

3.6.3 Undertow Profile

To examine the applicability of our undertow model, numerical computations are carried out on the same experimental data presented in Section 2.3.2. The bottom boundary roughness is k_N=*1.0*(mm) for Case1(Cox et al., 1995) and smooth-wall condition for the other cases(Okayasu and Katayama, 1992). Other conditions are shown in the Table-2.3. Cox and Kobayashi (1997) present more detailed measurements about undertow profiles in Cox et al.'s (1995) experiments.

Figures 3.8 to 3.12 show comparison of computed undertow profiles and wave heights with measured data. In the figures, it is seen that measured undertow profiles, dotted curves, are drastically changes around the trough level. This is simply because measured data includes the components of mass transport due to wave above the trough level. This feature was discussed in the Section 3.2.1 and was shown in the Figure-3.3. In this sense, we should compare the computed undertow profiles with measured data only below the trough level because the computed undertow profiles do not include the components of mass transport above the trough level. From these figures, it is seen that our model predicts undertow profiles fairly well both inside and outside of the surf-zone. From Figures 3.10, 3.11 and 3.12, it is also seen that our model predicts reasonable undertow profiles for the random wave problems.

From Figures 3.9 and 3.10, it is also seen that measured undertow velocity under the trough level near the breaking point increase in upper-ward. This feature indicates that the surface shear stress acts in the sea-ward direction near the breaking point.

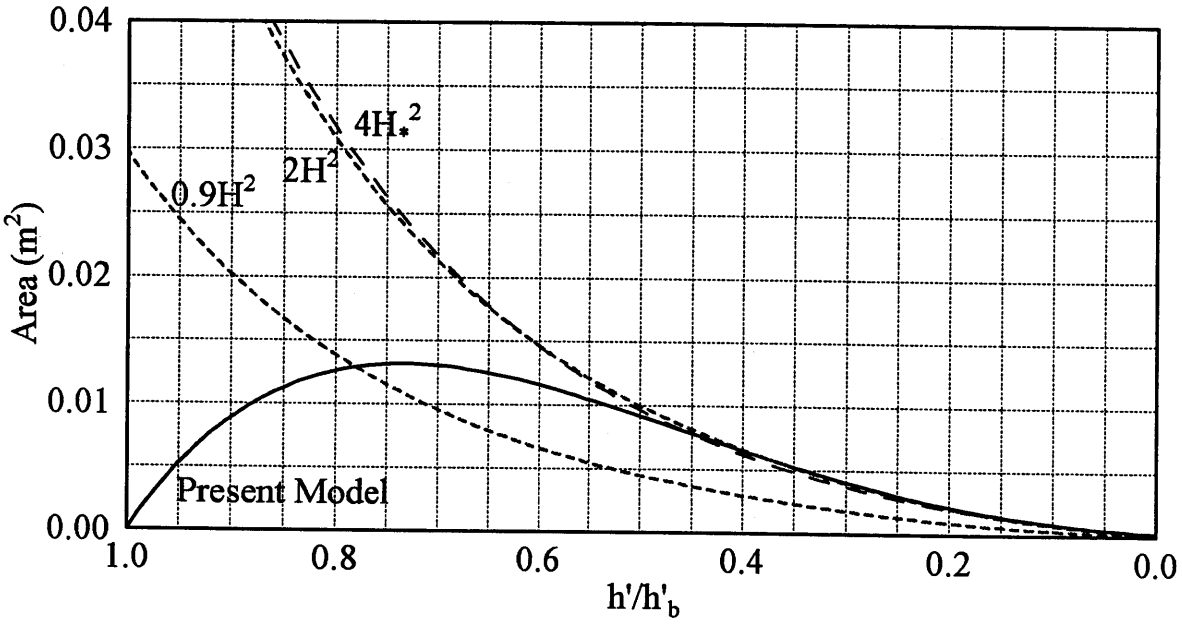

Figure-3.6 Area of the surface roller vs. h'/h'_b

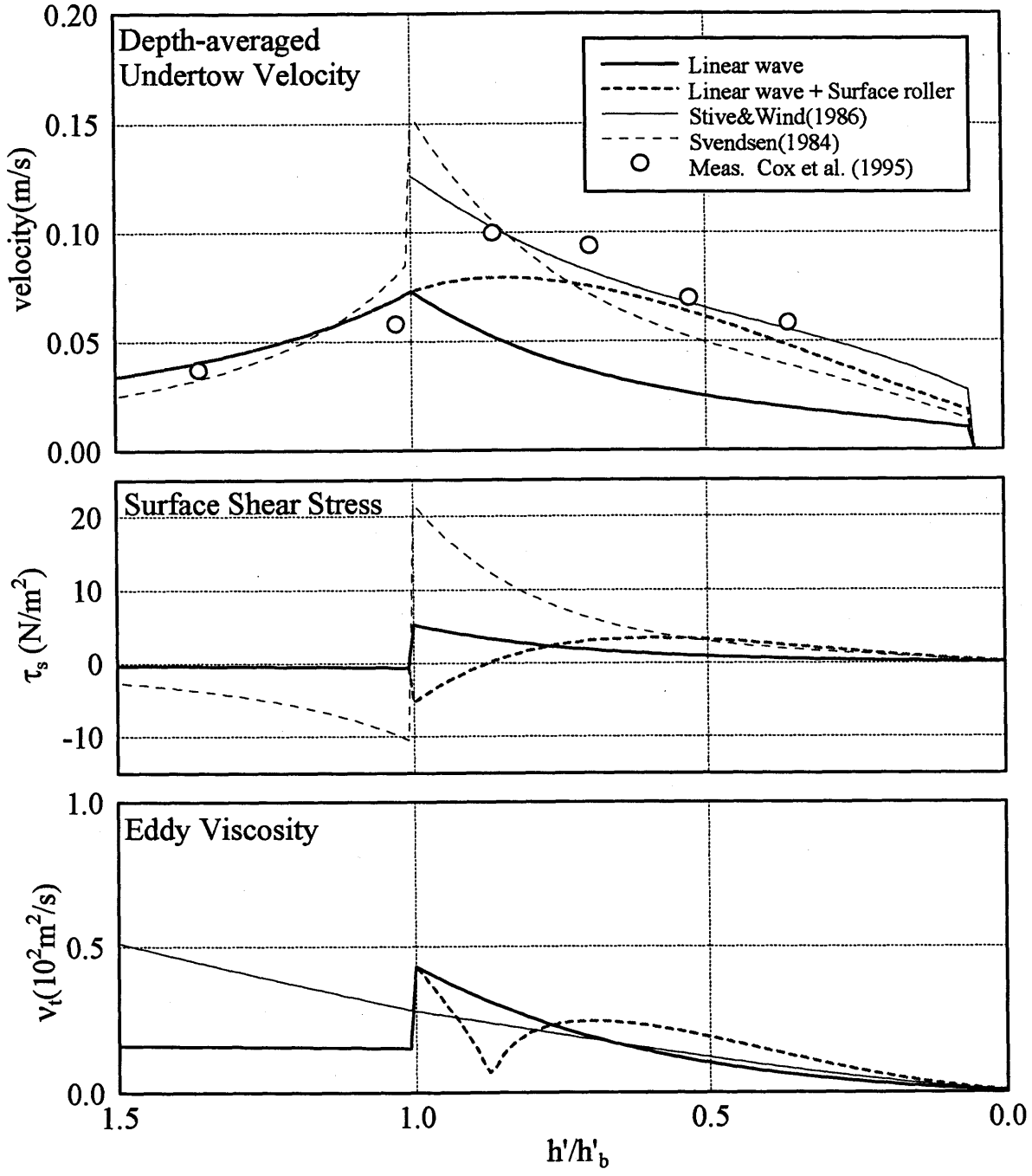

Figure-3.7 Computed parameters with measured data

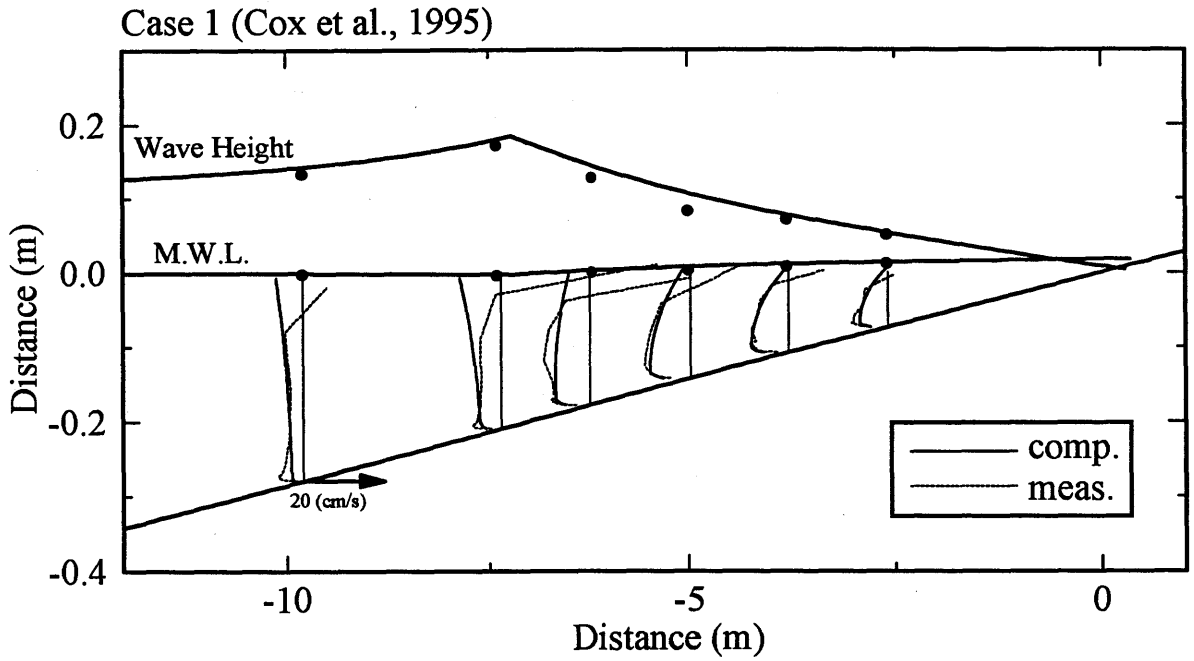

Figure-3.8 Undertow Profiles with measured data(Case 1)

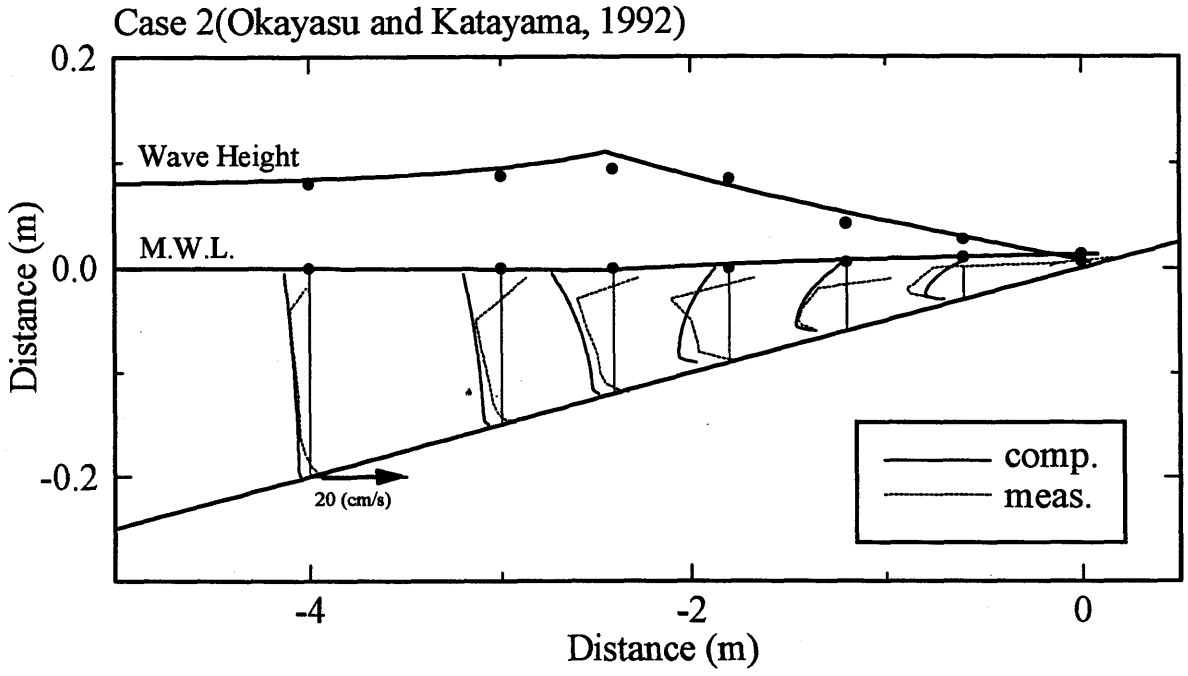

Figure-3.9 Undertow Profiles with measured data(Case 2)

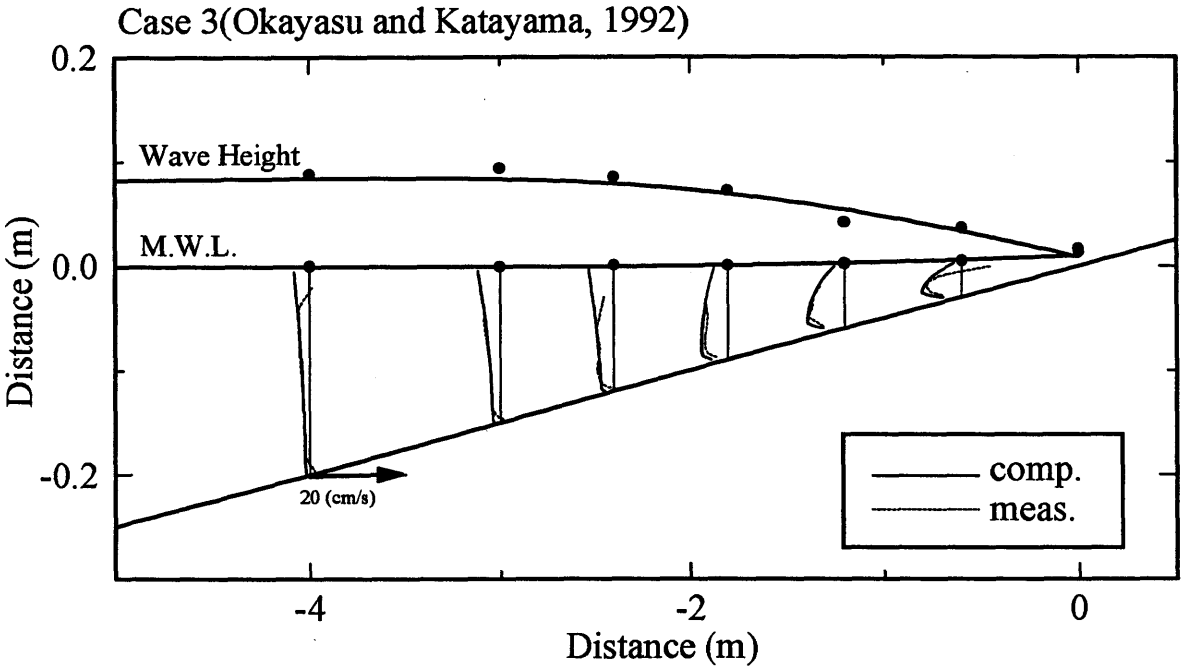

Figure-3.10 Undertow Profiles with measured data(Case 3)

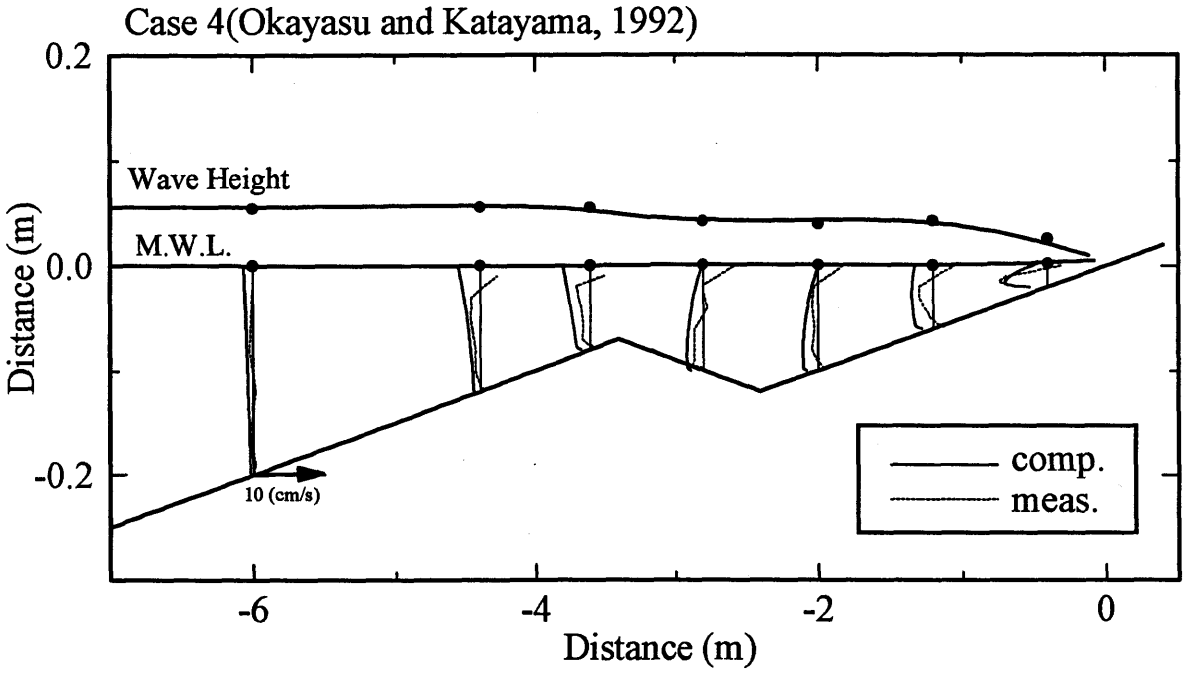

Figure-3.11 Undertow Profiles with measured data(Case 4)

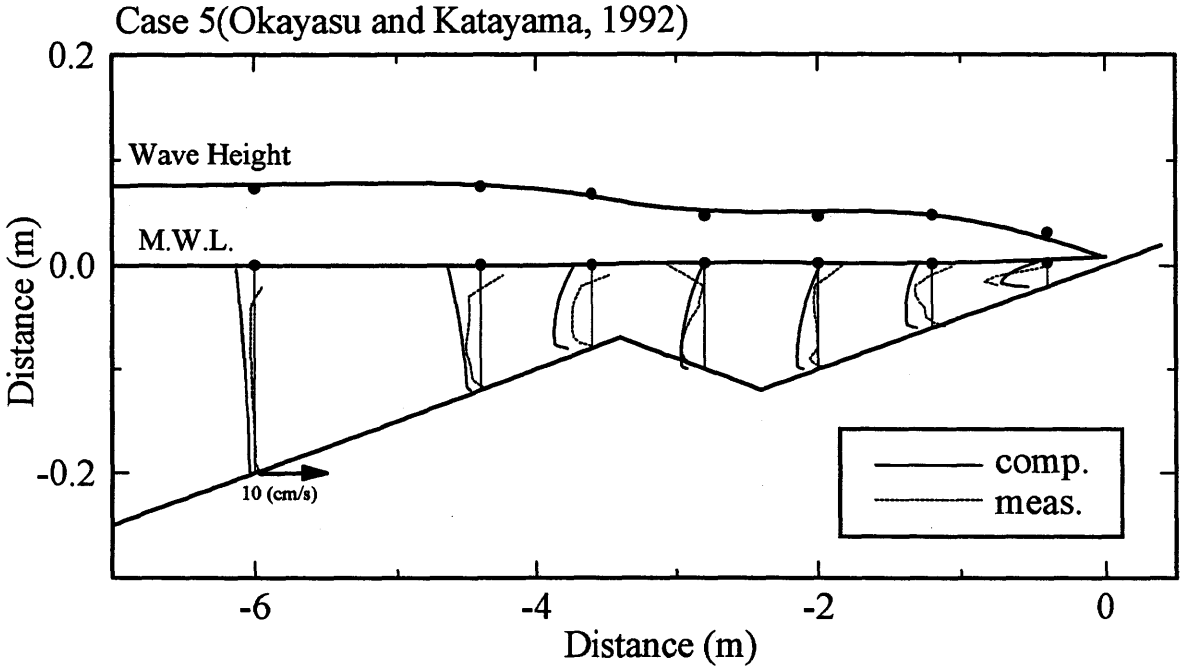

Figure-3.12 Undertow Profiles with measured data(Case 5)

Chapter 4

4. Conclusion

In this study, a hydrodynamics model for application outside and inside the surf-zone was developed. Although a strong non-linearity is expected inside the surf-zone, we simply applied linear wave theory by adopting the concept of an equivalent linear wave, which takes non-linear wave effects into account.

The model broadly consists of following three models. (1) Non-linear wave asymmetry and skewness model due to wave non-linearity and bottom slope, (2) Breaking wave dissipation model and (3) Undertow model. Since all these models are based purely on the linear wave theory, it is easy to apply these models to practical problems. Moreover, the equivalent linear wave theory also enables us to extend the models to random wave conditions rather easily. In conclusion, all the models are summarized and further refinements and extensions of the models are discussed.

4.1 Non-Linear Wave Model

The main goal of this model is to evaluate the non-linear (actual) bottom orbital velocity profiles from the equivalent linear wave conditions. In order to know the relationship between equivalent linear wave and non-linear wave, we performed numerical experiments on uniform slopes using Nwogu's (1993) Boussinesq equations. Through the experiments, the relationship between equivalent linear wave and non-linear wave was determined under the assumption that energy flux should be conserved between both theories.

From the experiments, five parameters were extracted to evaluate the non-linear wave height, non-linear "height" of the bottom orbital velocity and the asymmetry/skewness of the bottom orbital velocity from the equivalent linear wave conditions. These parameters were plotted as a function of h/L_0 and H_0/L_0, which are determined from the equivalent linear wave conditions. The semi-empirical formulae, which approximate these plotted curves as a function of h/L_0 and H_0/L_0, were also proposed.

The bottom orbital velocity profile is approximated by a combination of four sinusoidal curves, each of which represents asymmetry/skewness parameters. The approximated profiles agreed well with experimental data obtained by Cox, et al. (1995). Although the model is developed for uniformly sloping bed condition, the model also agreed well with Cnoidal wave theory for constant depth conditions. The advantage of this model is that all the parameters can be explicitly determined from linear wave theory.

4.2 Breaking Wave Dissipation Model

In order to evaluate the accurate breaking point from the linear wave conditions, we applied Watanabe's(1984) breaking criteria to the model. Once the waves are judged to be breaking from Watanabe's (1984) breaking criteria, breaking wave energy dissipation model is applied.

As for breaking energy dissipation model, we reviewed the Dally et al.'s (1985) and the Watanabe and Dibajnia's (1988) models and discussed advantages and disadvantages of these models through the comparison of wave heights obtained by their model with experimental data. The main disadvantage of the Dally et al.'s (1985) model is that the proportionality constant, which determines the amount of energy dissipation rate, is not given as a function of slope but given as a single constant. This problem results in evaluating too large/small wave heights in the surf-zone when the bottom slope is steeper/gentler. Although the Watanabe and Dibajnia's (1988) model took the effect of the bottom slope into account, their model was not applicable to the constant depth condition, which is expected to occur inside the surf-zone. Furthermore, it is found from the comparison with experimental data that their model has too small a slope-dependency.

We applied the same concept as the Dally et al.'s (1985) model but took the effect of the bottom slope into account. We semi-empirically determined the proportionality constant as a function of the bottom slope based on observed characteristics of the wave heights attenuation inside the surf-zone. Through the comparison of wave heights estimated by present model and experimental data, it was found that the present model has a reasonable slope-dependency. Moreover, it is notable that our model is applicable even for constant depth conditions.

We also extended the model to random wave conditions by assuming wave heights to be

Rayleigh distributed. The breaking wave model agreed well with a number of experimental data for both periodic and random waves.

4.3 Undertow Model

Based on the two-dimensional horizontal momentum equation, we derived the theoretical formula for the time-averaged undertow profile. This formula requires three unknown variables; the surface shear stress, the bottom shear stress and the depth-averaged return flow velocity.

These three variables were also derived based on the equivalent linear wave theory. Through the comparison of these computed variables with experimental data obtained by Cox, et al. (1995), it was found that the linear wave theory predicts sufficiently accurate return flow velocities outside the surf-zone. However, it was also found that the linear wave theory could not explain the drastic increase of the return flow velocity inside the surf-zone. From this comparison, we conclude that the equivalent linear wave theory should be applicable for the entire region but that additional phenomena, such as surface roller effect, must be taken into account in order to evaluate the excess amount of return flow inside the surf-zone.

The surface roller model was therefore developed to evaluate the excess amount of return flow inside the surf-zone. Applying the similar concept of Dally and Brown's (1995) model, we developed an energy balance equation, which includes the growth/decay of the surface roller energy. Combining this energy balance equation with our breaking wave energy dissipation model, we determined the semi-empirical coefficient as a function of the bottom slope, which was taken as a single constant value in the Dally and Brown's (1995) model. Since the model is purely based on the equivalent linear wave theory, the surface roller model is also easily extended

to the random wave condition.

The surface shear stress due to the surface roller was also proposed. The combination of the surface shear stresses due to waves and surface roller reasonably explains the observed facts that the surface shear stress just after the breaking point acts in the seaward direction.

Finally, the complete undertow model was examined through the comparison of computed undertow profiles with experimental data of various cases. It was found that the undertow profiles evaluated by the present model agreed well with experimental data even for random wave conditions.

4.4 Model Extensions

If the waves are obliquely incident toward the coast, the decrease of the radiation stress due to the wave breaking causes a shore-parallel force in addition to the shore-normal force. The latter is the force causing wave setup and undertow, and is not greatly affected by the angle of wave incidence so long as this is relatively small. Thus, the present hydrodynamics model for the surf-zone should be approximately valid also for obliquely incident waves. The shore-parallel force, which depends on an angle of incidence even when this is small, causes longshore currents. The existence of longshore currents should affect the bottom friction shear stress and therefore should affect to some extent the undertow profiles. Furthermore, the surface roller should also yield a shore-parallel force. This additional shore-parallel force should affect the longshore currents. In this sense, therefore, the model should be extended to evaluate the interaction of the undertow and longshore current when the waves are obliquely incident on the shore.

According to Kampuis (1991), it is observed that the alongshore sediment transport rate

often has another peak around the mean shoreline besides the first peak inside the surf-zone. This phenomenon can not be explained by the present models because in these models the current velocity decreases toward the shoreline if the water depth also decreases. This excess amount of alongshore sediment transport should be strongly related to the swash-zone hydrodynamics. In order to estimate the topography evolution near the shoreline, therefore, it is necessary to develop the swash-zone model, which is consistent with present models.

Reference

Bagnold, R. A., 1963. "Mechanics of Marine Sedimentation," in *The Sea: Ideas and Observations*, vol.3, Interscience, NewYork.

Bailard, J. A., 1981. "An Energetics Total Load Sediment Transport Model fir a Plane Sloping Beach," *Journal of Geographical Research*, Vol.86(C11), pp.10938-10954.

Bruun, P., 1954. "Coast Erosion and the Development of Beach Profiles," *U.S. Army Beach Erosion Board Technical Memorandum*, No. 44.

Cox, D. and N. Kobayashi, 1997. "A Kinematic Undertow Model with a Logarithmic Boundary Layer," *Journal of Waterway, Port, Coastal, and Ocean Engineering*. Vol.123, No. 6, pp.344-360.

Cox, D., N. Kobayashi and A. Okayasu, 1995. "Experimental and Numerical Modeling of Surf Zone Hydrodynamics," *Report No. CACR-95-97*, Center for Applied Coastal Research, University of Delaware.

Cruz, E., H. Yokoki, M. Isobe and A. Watanabe, 1993. "Nonreflectiong boundary conditions for nonlinear wave equation," *Proceedings of Coastal Engineering*, JSCE, Vol. 40, pp.46-50. (in Japanese)

Dally, W. R., R. G. Dean and R. A. Dalrymple, 1985. "Wave Height Variation Across Beaches of Arbitrary Profile," *Journal of Geophysical Research*, Vol.90(C6), pp.11917-11927.

Dally, W. R. and C. A. Brown, 1995. "A Modeling Investigation of the Breaking Wave Roller with Application to Cross-shore Currents," *Journal of Geophysical Research*, Vol.100(C12), pp.24873-24883.

Dean, R. G., 1965. "Stream Function Representation of Nonlinear Ocean Waves," *Journal of Geophysical Research*, Vol. 70(18), pp. 4561-4572.

Dean, R. G., 1977. "Equilibrium beach profiles: U. S. Atlantic and Gulf coasts," *Department of Civil Engineering, Ocean Engineering Report* No.12, University of Delaware, Newark, Delaware.

Dean, R. G., 1991. "Equilibrium Beach Profiles: Characteristics and applications," *Journal of Coastal Research*, Vol. 7, No. 1, pp. 53-84.

Goda, Y., 1970. "A Synthesis Breaker Indices," *Proceedings of the Japan Society of Civil Engineers*, No. 180, pp. 39-49. (in Japanese)

Hiruta, H. and M. Hattori, 1999, "Evolutional Behaviors of Breaking Wave Rollers," *Proceedings of the 46th Japanese conference on Coastal Engineering*, JSCE, pp. 126-130. (in Japanese)

Hoffman, J. D., 1992. "Numerical Method for Engineers and Scientists," *McGraw-Hill, Inc.*, New York, 825p.

Horikawa, K., 1985. "Nearshore Dynamics and Coastal Processes," *University of Tokyo Press*, 522p. (in Japanese)

Horikawa, K. and C. T. Kuo, 1966. "A Study of Wave Transformation inside Surf Zone," *Proceedings of the 10th International Conference on Coastal Engineering*, Vol.1, pp.217-233.

Inman, D. L., M. H. S. Elwany and S. A. Jenkins, 1993. "Shorerise and Bar-Berm Profiles on Ocean Beaches," *Journal of Geophysical Research*, Vol. 98, N. C10, pp.18181-18199.

Isobe, M., 1979. "Hozonha no Setsudo-kai no Hako ni yoru Hyouji," *Annual Conference*, JSCE, II-394, pp.760-761. (in Japanese)

Isobe, M., 1985. "Calculation and Application of First-order Cnoidal Wave Theory," Coastal Engineering, Elsevier, Vol. 9, pp.309-325.

Isobe, M., 1987. "A Parabolic Equation Model for Transformation of Irregular Waves due to Refraction, Diffraction, Breaking," *Coastal Engineering in Japan*, JSCE, Vol.30, No. 1, pp. 33-47.

Isobe, M. and K. Horikawa, 1981. "Change in Velocity Field in and near the Surf Zone," *Proceedings of the 28th Japanese Conference on Coastal Engineering*, JSCE, pp.5-9. (in Japanese)

Kampuis, J. W., 1991. "Alongshore Sediment Transport Rate Distribution," Coastal Sediments '91, ASCE, pp.170-183.

Kuriyama, Y., 1998. "Field Measurements of Undertow on Longshore Bars," *Proceedings of the 26th International Conference on Coastal Engineering*, ASCE, pp.297-310.

Longuet-Higgins M. S., 1952. "On the Statistical Distribution of the Heights of sea waves," *Journal of Marine Research*, Vol.11, No.3, pp.245-266.

Longuet-Higgins, M. S. and R. W. Stewart, 1962. "Radiation Stress and Mass Transport in Gravity Waves, with application to "Surf Beat"," Journal of Fluid Mechanics, Vol.13, pp.481-504.

Longuet-Higgins, M. S. and R. W. Stewart, 1964. "Radiation Stresses in Water Waves; A Physical Discussion, with Applications," *Deep-Sea Research*, Pergamon Press Ltd., vol. 11, pp.529-562.

Madsen, O. S., 1991. "Mechanics of Cohesionless Sediment Transport in Coastal Waters," *Proceedings Coastal Sediments '91*, ASCE, Vol.1, pp.15-27.

Madsen, O. S., 1994. "Spectral Wave-Current Bottom Boundary Layer Flows," *Proceedings of the 24th International Coastal Engineering Conference*, ASCE, pp.384-398.

Madsen, O. S. and P. Salles, 1998. "Eddy Viscosity Models for Wave Boundary Layers," *Proceedings of the 26th International Coastal Engineering Conference*, ASCE, pp.2615-2627.

Madsen, O. S. and W. D. Grant, 1976. "Quantitative Description of Sediment Transport by Waves," *Proceedings of the 15th International Coastal Engineering Conference*, ASCE, Vol. 2, pp. 1093-1112.

Maruyama, K. and T. Shimizu, 1986. "Simulation model for wave deformation considering interaction of waves and a beach," *Proceedings of the 33rd Japanese conference on Coastal Engineering*, JSCE, pp. 109-113. (in Japanese)

Meyer, R. N. and O. S. Madsen, 1998. "Modeling Equilibrium Beach Profiles using a Theoretical Approach," *Master thesis of Massachusetts Institute of Technology*, Massachusetts Institute of Technology, 128p.

Mizuguchi, Y., K. Tsujioka and K. Horikawa, 1978. "Saihago no Hakohenka ni tsuite no Ichi-Kosatsu," *Proceedings of the 25th Japanese conference on Coastal Engineering*, JSCE, pp. 155-159. (in Japanese)

Nairn, R. B. and H. N. Southgate, 1993. "Deterministic Profile Modeling of Nearshore Processes, Part2. Sediment Transport and Beach Development," *Coastal Engineering*, Vol.19, pp.57-96

Nwogu, O., 1993. "Alternative Form of Boussinesq Equations for Nearshore Wave Propagation," *Journal of Waterway, Port, Coastal and Ocean Engineering*, ASCE, 119(6), pp.618-638.

Okayasu, A., T. Shibayama and K. Horikawa, 1988. "Vertical Variation of Undertow in the Surf Zone," *Proceedings of the 21st International Coastal Engineering Conference*, ASCE, pp.478-491.

Okayasu, A., A. Watanabe and M. Isobe, 1990. "Modeling of Energy Transfer and Undertow in the Surf Zone," *Proceedings of the 22nd International Coastal Engineering Conference*, ASCE, pp.123-135.

Okayasu, A. and H. Katayama, 1992. "Distribution of Undertow and Long-Wave Component Velocity due to Random Waves," *Proceedings of the 23rd International Coastal Engineering Conference*, ASCE, Vol.1, pp.883-893.

Saeki and Sasaki, 1974. "Saiha go no Nami no Henkei ni Kansuru Kenkyu," *Proceedings of the 21st Japanese conference on Coastal Engineering*, JSCE, pp. 39-44. (in Japanese)

Shuto, N., 1974. "Nonlinear Long Waves in a Channel of a Variable Section," *Coastal Engineering in Japan*, vol.17, pp1-12.

Stieve, M. J. F. and H. G. Wind, 1986. "Cross-shore Mean Flow in the surf Zone," *Coastal Engineering*, Elsevier, vol.10, pp. 325-340.

Svendsen, I. A., 1984. "Mass Flux and Undertow in a Surf Zone," *Coastal Engineering*, Elsevier, vol.8, pp. 347-365.

Watanabe, A. and M. Dibajnia, 1988. "A Numerical Model of Wave Difformation in Surf Zone," *Proceedings of 21st International Coastal Engineering Conference*, ASCE, pp. 579-587.

Watanabe, A., T. Hara and K. Horikawa, 1984. "Study on Breaking Condition for Compound Wave Trains," *Coastal Engineering in Japan*, JSCE, Vol.27, pp 71-82.

Zheng, P., 1999. "A High-Order Numerical Model for Waves and Curents Based on Boussinesq Equations," Dissertation at University of Tokyo, Department of Civil Engineering, University of Tokyo, Japan, 170p.

Appendix A

A. Numerical Methodology of the Boussinesq Equations

In this section, the numerical methodology for Nwogu's (1993) Boussinesq equations is presented. For numerical computations, Zheng's (1999) finite different scheme is applied.

A.1 Governing Equation

Governing equations of Nwogu's (1993) Boussinesq equations for 1-dimensional problem are as follows.

Continuity equation;

$$\eta_t + [(h+\eta)u]_x + \left[a_1 h^3 u_{xx} + a_2 h^2 (hu)_{xx}\right]_x = 0 \tag{A.1}$$

Momentum equation;

$$u_t + g\eta_x + uu_x + b_1 h^2 u_{xxt} + b_2 h (hu)_{xxt} = 0 \tag{A.2}$$

where the constants a_1, a_2, b_1 and b_2 are given by

$$a_1 = \frac{1}{2}\left(\frac{z_\alpha}{h}\right) - \frac{1}{6};\ a_2 = \frac{z_\alpha}{h} + \frac{1}{2};\ b_1 = \frac{1}{2}\left(\frac{z_\alpha}{h}\right)^2;\ b_2 = \frac{z_\alpha}{h} \tag{A.3}$$

In these equations, horizontal velocity, $u(x,t)$, is represented by the velocity at a certain depth, $z = z_\alpha$. According to Nwogu(1993), $z_\alpha = -0.553h$ gives the optimum dispersion relationship that is close to the small amplitude linear wave theory. We therefore applied $z_\alpha = -0.553h$ in this computation. For the sake of simplicity of the expression, we express (A.1) and (A.2) as follows.

$$\eta_t = E(\eta,u) \tag{A.4}$$

$$U_t = F(\eta,u) \tag{A.5}$$

where

$$E(\eta,u) = -[(h+\eta)u]_x - [a_1 h^3 u_{xx} + a_2 h^2 (hu)_{xx}]_x \tag{A.6}$$

$$U = u + b_1 h^2 u_{xx} + b_2 h (hu)_{xx} \tag{A.7}$$

$$F(\eta,u) = -g\eta_x - uu_x \tag{A.8}$$

These expressions are used later when we discuss the dicretization method in the time step.

A.2 Discretization in the Space Step

We apply a space staggered grid and shift the location of u_i by a half grid from the point of η_i and h_i. The locations of these values are shown in the Figure-A.1.

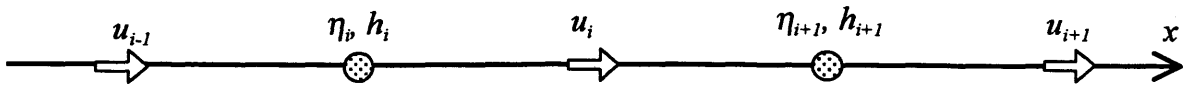

Figure-A.1 Staggered grid

Using this staggered grid, each term of the continuity equation (A.1) is discretized by centered difference scheme around η_i as follows.

$$\delta_x[(h+\eta)u]_i = \frac{1}{24\Delta x}[(h_{i-3/2}+\eta_{i-3/2})u_{i-2} - 27(h_{i-1/2}+\eta_{i-1/2})u_{i-1} + 27(h_{i+1/2}+\eta_{i+1/2})u_i + (h_{i+3/2}+\eta_{i+3/2})u_{i+1}] \quad \text{(A.9)}$$

$$\delta_{xx}u_i = \frac{1}{\Delta x^2}[u_{i+1} - 2u_i + u_{i-1}] \quad \text{(A.10)}$$

$$\delta_{xx}(hu)_i = \frac{1}{\Delta x^2}[h_{i+3/2}u_{i+1} - 2h_{i+1/2}u_i - h_{i-1/2}u_{i-1}] \quad \text{(A.11)}$$

$$\delta_x(h^3u_{xx})_i = \frac{1}{\Delta x}[h^3_{i+1/2}u_i - h^3_{i-1/2}u_{i-1}] \quad \text{(A.12)}$$

$$\delta_x(h^2(hu)_{xx})_i = \frac{1}{\Delta x}[h^2_{i+1/2}\delta_{xx}(hu)_i - h^2_{i-1/2}\delta_{xx}(hu)_{i-1}] \quad \text{(A.13)}$$

Here, the fourth-order centered difference scheme is applied to the first order differentiation terms while the second order scheme is applied to the higher order differentiation terms. Similarly, the momentum equation (A.2) is discretized around u_i as follows.

$$\delta_x(\eta)_i = \frac{1}{24\Delta x}[\eta_{i+1} - 27\eta_i + 27\eta_{i+1} - \eta_{i+2}] \quad \text{(A.14)}$$

$$(u\delta_x u)_i = \frac{1}{4\Delta x}(u_i - |u_i|)[-3u_i + 4u_{i+1} - u_{i+2}] + \frac{1}{4\Delta x}(u_i + |u_i|)[3u_i - 4u_{i-1} + u_{i-2}] \quad \text{(A.15)}$$

where the upward second-order scheme is used for the convection term in (A.15).

A.3 Discretization in the Time Step

The time-integration of the governing equations (A.4) and (A.5) consists of the third-order Adams-Bashforth predictor and fourth-order Adams-Moulton corrector schemes(Hoffman, 1992).

A.3.1 Predictor Step

The third order explicit Adams-Bashforth scheme is expressed as follows.

$$\eta_i^{(n+1)^*} = \eta_i^n + \frac{\Delta t}{12}\left[23E_i^n - 16E_i^{n-1} + 5E_i^{n-2}\right] \tag{A.16}$$

$$U_i^{(n+1)^*} = U_i^n + \frac{\Delta t}{12}\left[23F_i^n - 16F_i^{n-1} + 5F_i^{n-2}\right] \tag{A.17}$$

All variables on the right-hand side of (A.16) and (A.17) are known from the previous, nth-step computations. The variables superscribed by a star on the left-hand side of (A.16) and (A.17) are the predicted values for the $(n+1)$th-step, which are straightforward to obtain. For example, (A.17) is equivalent to a tridiagonal matrix equation and is therefore solved by applying the Thomas algorithm. Using these predicted values, we can estimate corresponding predicted values of $E_i^{(n+1)^*}$ and $F_i^{(n+1)^*}$. These values are used for the next corrector step.

A.3.1 Corrector Step

The fourth order Adams-Moulton scheme is expressed as follows.

$$\eta_i^{(n+1)} = \eta_i^n + \frac{\Delta t}{24}\left[9E_i^{(n+1)^*} + 19E_i^n - 5E_i^{n-1} + E_i^{n-2}\right] \tag{A.18}$$

$$U_i^{(n+1)} = U_i^n + \frac{\Delta t}{24}\left[9F_i^{(n+1)^*} + 19F_i^n - 5F_i^{n-1} + F_i^{n-2}\right] \tag{A.19}$$

From (A.18) and (A.19), newly corrected variables for the $(n+1)$th-step are computed. The corrector step is iterated by taking these new $(n+1)$th-step variables as predicted $(n+1)$th values until the error between two successive results reaches a required a limit. The error of each variable is defined as

$$\varepsilon(\eta)=\frac{\sum_i \left|\eta_i^{(n+1)}-\eta_i^{(n+1)*}\right|}{\sum_i \left|\eta_i^{(n+1)}\right|};\quad \varepsilon(u)=\frac{\sum_i \left|u_i^{(n+1)}-u_i^{(n+1)*}\right|}{\sum_i \left|u_i^{(n+1)}\right|} \tag{A.20}$$

where the star superscript denotes the values of the previous estimation, i.e., predicted value. The corrector step is iterated if any $\varepsilon(\eta)$ or $\varepsilon(u)$ exceeds *0.1%*.

A.4 Boundary conditions

A.4.1 Incident Wave Boundary

The time series of incident wave conditions at two space steps, $\eta_{I,1}$, $\eta_{I,2}$, u_{I1} and u_{I2} are specified analytically by Stokes wave theory or the Stream Function Method[Dean, 1965]. Using these values, variables inside $n > 2$ are computed.

A.4.2 Absorbing Boundary

Absorbing boundary consists of two conditions. The first is Sommerfeld radiation condition, which is applied just at the boundary where waves are supposed to go out. The second condition is the sponge layer (damping layer), which is applied over a certain distance in front of the boundary.

(1) Sommerfeld Radiation Condition

A non-reflective condition is used to absorb the outgoing waves, i.e., the wave conditions outside the boundary are determined by following.

$$\eta_t + C\eta_x = 0 \tag{A.21}$$

$$u_t + Cu_x = 0 \tag{A.22}$$

where $C = \sqrt{gh}$ is the wave phase velocity approximated by the linear long wave theory. For example, (A.21) is discretized by the first-order backward(forward) difference scheme and solved by applying the third-order Adams-Bashforth predictor and fourth-order Adams-Moulton corrector schmes [Hoffman, 1992]. The discretized formula is as follows.

Predictor Step;

$$\eta_{i+1}^{(n+1)*} = \eta_{i+1}^{n} - C\frac{\Delta t}{12\Delta x}\left[\left(23\eta_{i+1}^{n} - 16\eta_{i+1}^{n-1} + 5\eta_{i+1}^{n-2}\right) - \left(23\eta_{i}^{n} - 16\eta_{i}^{n-1} + 5\eta_{i}^{n-2}\right)\right] \tag{A.23}$$

Corrector Step;

$$\eta_{i+1}^{(n+1)} = \eta_{i+1}^{n} - C\frac{\Delta t}{24\Delta x}\left[\left(9\eta_{i+1}^{(n+1)*} + 19\eta_{i+1}^{n} - 5\eta_{i+1}^{n-1} + 5\eta_{i+1}^{n-2}\right) - \left(9\eta_{i}^{(n+1)*} + 19\eta_{i}^{n} - 5\eta_{i}^{n-1} + 5\eta_{i}^{n-2}\right)\right] \tag{A.24}$$

(2) Sponge Layer

Previously presented radiation boundary condition inevitably includes finite errors because of the numerical discretization or approximation of the phase velocity. This error can become the reflected wave components and can eventually cause the model to blow up in some cases. To reduce this reflection, a sponge layer is applied over a certain distance before the boundary. This sponge layer dissipates the wave energy and therefore makes wave heights or particle velocities at the boundary sufficiently small so that reflected wave components are negligible. Damping terms are added to the momentum equation (A.5) as

$$U_t = F(\eta, u) - \varepsilon u \tag{A.25}$$

where the damping coefficient, ε, is obtained by Cruz et al. (1993) as

$$\varepsilon = \frac{\theta\gamma}{2(\sinh\gamma - \gamma)}\sqrt{\frac{g}{h}}\left[\cosh(\gamma R / F) - 1\right] \tag{A.26}$$

where F is a thickness of sponge layer, which is about two or three times the wavelength, γ=*3*, θ=*0.15~5.0* and R is the distance from the beginning point of the sponge layer. As seen in (A.26), the damping due to the sponge layer becomes larger/smaller when q is larger/smaller. However, but the reflection due to the sponge layer also becomes stronger/weaker when θ is larger/smaller. In this sense, therefore, we need to determine the optimum value of θ so that the sponge layer absorbs the wave energy effectively but does not reflects waves. In this study, we adopted θ =*3*.

Appendix B

B. Linear Wave Theory vs. Stream Function Method

In this section, we examine the applicability of the linear wave theory using the concept of equivalent linear wave height based on the conservation law of the wave energy flux. Dean's (1965) Stream Function Method with 19 terms (SFM) was used to estimate characteristic variables including wave non-linearity, which are compared with those variables estimated by the equivalent linear wave theory.

B.1 Equivalent Linear Wave Height

Equivalent linear wave height is estimated under the assumption that energy flux should be conserved between linear wave theory and non-linear wave theory. In SFM, energy flux, $E_{f,SFM}$ is numerically computed by integrating the following formula.

$$E_{f,SFM} = \int_{-h}^{\eta} \left(p + \frac{1}{2}\rho(u^2 + w^2) + \rho g z \right) u dz = -\int_{-h}^{\eta} \rho \frac{\partial \phi}{\partial t} \frac{\partial \phi}{\partial x} dz \qquad \text{(B.1)}$$

where h is the still water depth, η is the free surface elevation and u and w are particle velocities

in the x and z directions, respectively. From the non-linear energy flux obtained from (B.1), the equivalent linear wave height, H_*, is determined by

$$H_* = \sqrt{8E_{f,SFM} / \rho g C_g} \tag{B.2}$$

Figure-B.1 shows H_{SFM}/H_* as a function of h/L_0 and H_{SFM}/h where H_{SFM} is the non-linear wave height of SFM and L_0 is the deep-water wavelength. As seen in the figure, H_{SFM}/H_* becomes larger when H_{SFM}/h is larger. For all the following comparison, the equivalent linear values are all based on the equivalent linear wave height obtained from (B.2).

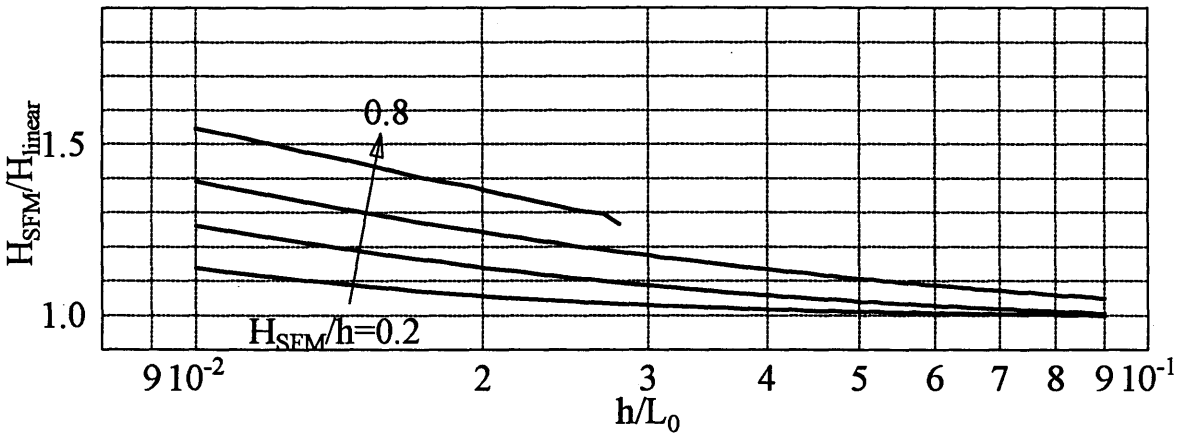

Figure-B.1 Comparison of the wave heights between SFM and the equivalent linear wave theory

B.2 Wave Energy

Generally, the wave potential energy, E_p, and wave kinetic energy, E_k, are determined as

$$E_p = \overline{\int_0^{\eta} \rho g z d} \tag{B.3}$$

$$E_k = \overline{\int_{-h}^{\eta} \frac{\rho}{2}(u^2 + w^2) dz} \tag{B.4}$$

According to the linear wave theory, both E_p and E_k have the same value and determined as

$$E_p = E_k = \frac{1}{16}\rho g H_*^2 \tag{B.5}$$

Figure-B.2 shows the comparison of these energies obtained by the equivalent linear wave theory and SFM. From the figure, it is observed that both kinetic and potential energies obtained by SFM become smaller than those obtained by the equivalent linear wave theory when H_{SFM}/h becomes larger. This result implies that the group velocity determined by SFM should be larger than that determined by the equivalent linear wave theory since energy flux should be conserved between both theories. This feature is discussed again in the next section. Moreover, it is also found that the wave potential energy becomes smaller than wave kinetic energy in SFM while both energies are identical to each other in the linear wave theory.

B.3 Phase Velocity and Group Velocity

The group velocity in SFM, C_{gSFM}, can be obtained from energy flux, E_{fSFM} and wave energy as

$$C_{gSFM} = E_{fSFM} / (E_p + E_k) \tag{B.6}$$

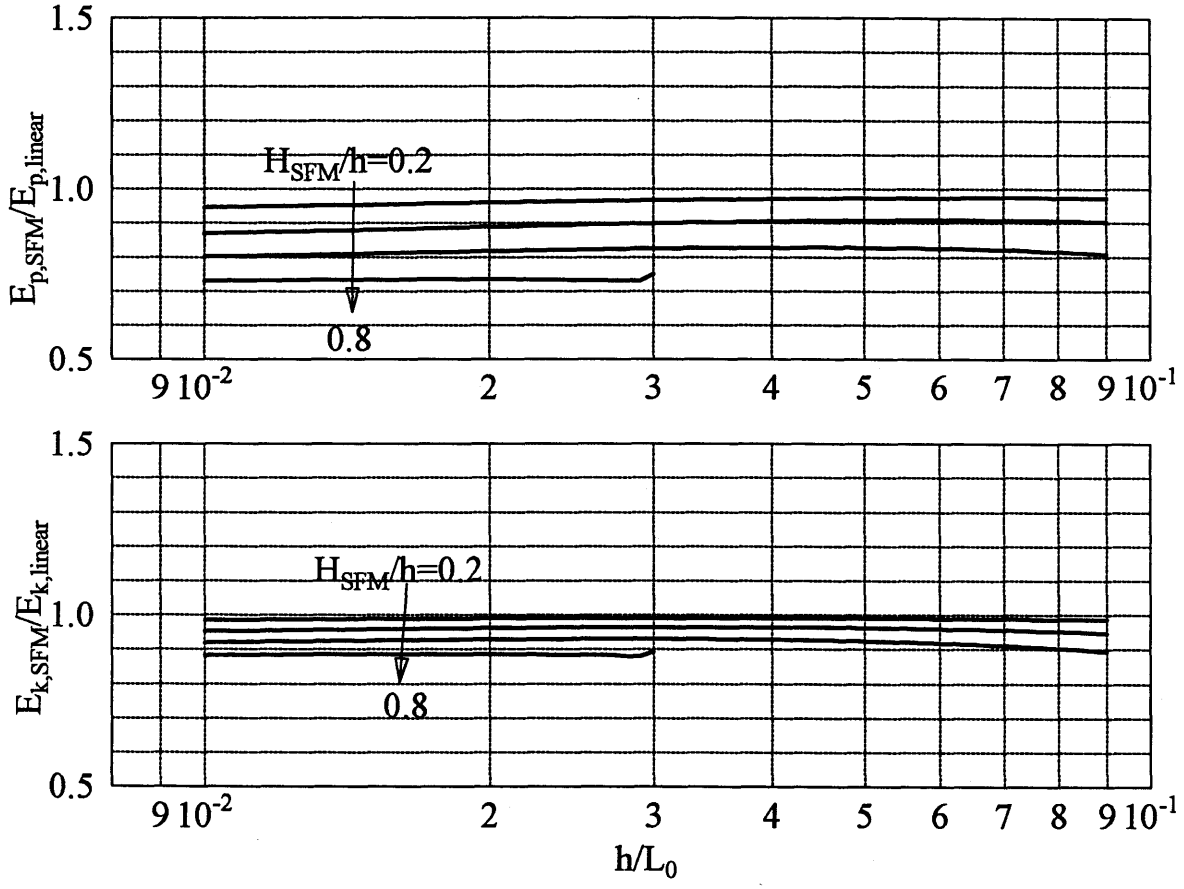

Figure-B.2 Comparison of the wave energy between SFM and the equivalent linear wave theory

Figure-B.3 shows C_{SFM}/C_{linear} and $C_{gSFM}/C_{glinear}$ as a function of H_{SFM}/h and h/L_0. From the figure, it is seen that both C_{SFM}/C_{linear} and $C_{gSFM}/C_{glinear}$ have similar characteristics. As discussed before, the group velocities obtained by SFM become larger than those obtained by the equivalent linear wave theory when H_{SFM}/h (h/L_0) becomes larger (smaller). This is surely the opposite tendency of the wave energy as discussed in Section B.3. However, it is also seen that the difference of these velocities between the equivalent linear wave theory and SFM is small compared with the difference of the wave heights.

B.4 Mass Transport

The time-averaged mass transport above the trough level is generally determined by

$$M = \overline{\int_{\eta_t}^{\eta} u dz} \tag{B.7}$$

Here $\eta_t < 0$ denotes the trough level. In SFM, the time-averaged mass transport is computed numerically from (B.7). In linear wave theory, the time-averaged mass transport above the trough level is analytically determined from (B.7) as

$$M_{linear} = \overline{\int_{-a_*}^{\eta} u dz} = \frac{a_*^2 \omega}{2 \tanh k(h+\overline{\eta})} \tag{B.8}$$

where a_* is the amplitude of the equivalent linear wave and $h+\overline{\eta}$ denotes the mean water depth. Figure-B.4 shows M_{SFM}/M_{linear} as a function of h/L_0 and H_{SFM}/h. From the figure, it is observed that the M_{SFM}/M_{linear} becomes smaller when H_{SFM}/h becomes larger while C_{SFM}/C_{linear} and $C_{gSFM}/C_{glinear}$ become larger as seen before. This is because the free surface profile of SFM becomes sharper due to wave non-linearity and eventually transports less water than linear wave does.

The difference between the models, however, is less than 20%. Moreover, it is expected that this difference becomes smaller for non-zero bottom slope condition because the free surface wave profile becomes saw-tooth type, which moderates the sharpness of the wave crest.

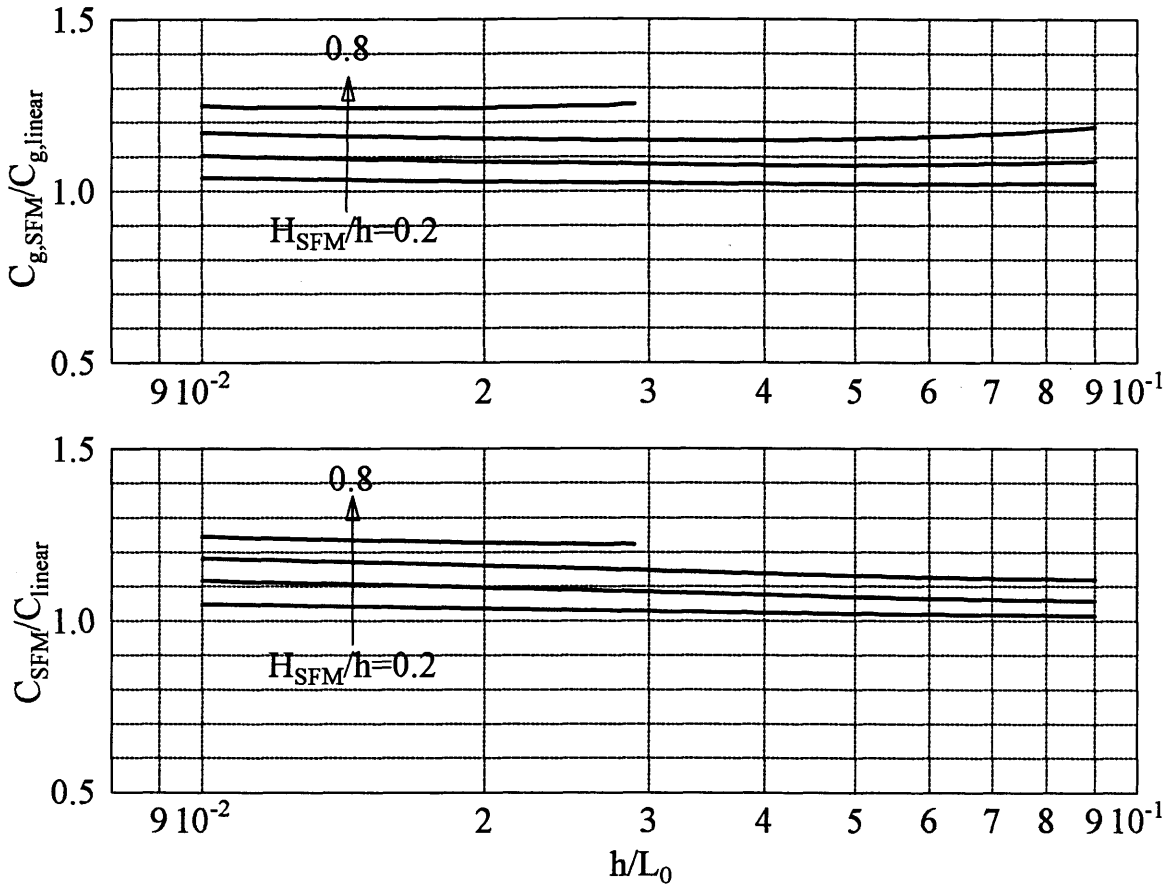

Figure-B.3 Comparison of the phase and group velocities between SFM and the equivalent linear wave theory

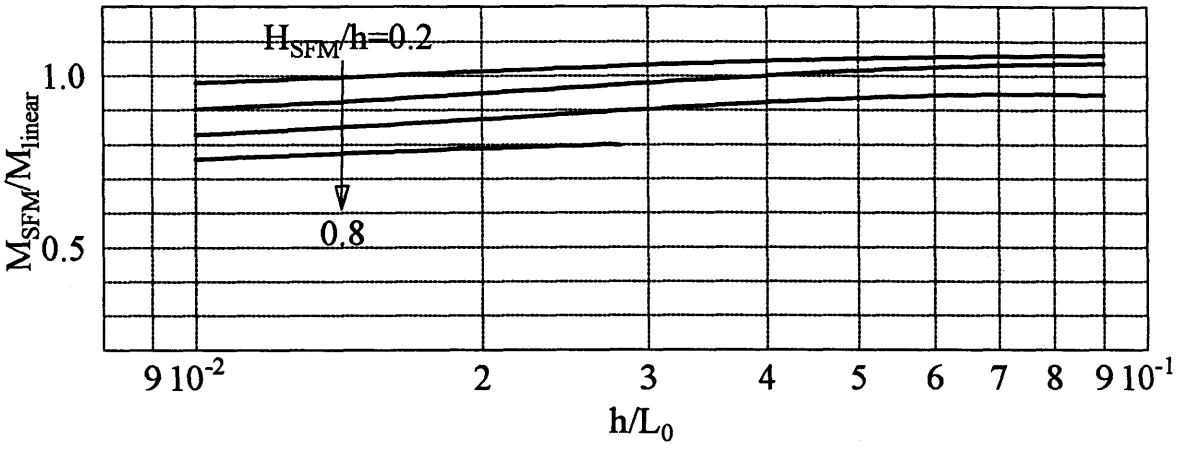

Figure-B.4 Comparison of the mass transport between SFM and the equivalent linear wave theory

B.5 Momentum Flux

Horizontal time-averaged momentum flux due to the wave, M_x, is generally determined by

$$M_x = \overline{p + \rho u^2 + \rho g z} \tag{B.9}$$

where $p = -\rho\frac{\partial \phi}{\partial t} - \frac{\rho}{2}(u^2 + w^2) - \rho g z$ is the total pressure. Integrating (B.9) with respect to z from the bottom to the free surface and subtracting the hydrostatic pressure, Radiation stress, S_{xx}, is determined as

$$S_{xx} = \overline{\int_{-h}^{\eta}(p + \rho u^2)dz} + \int_{-h}^{\bar{\eta}} \rho g z dz = \overline{\int_{-h}^{\eta}(p + \rho u^2)dz} + \frac{1}{2}\rho g(\bar{\eta}^2 - h^2) \tag{B.10}$$

where $\bar{\eta}$ is the mean water level and over bar indicates the time-averaged value. In SFM, the radiation stress is numerically computed from (B.10). In linear wave theory, (B.10) is analytically

represented by applying Stokes wave theory and keeping up to the second order as

$$
\begin{aligned}
S_{xx} &= \int_{-h}^{\overline{\eta}} \overline{(p+\rho u^2)}dz + \overline{\int_{\overline{\eta}}^{\eta} (p+\rho u^2)dz} + \frac{1}{2}\rho g(\overline{\eta}^2 - h^2) \\
&\equiv \int_{-h}^{\overline{\eta}} \left[\rho(\overline{u^2 - w^2}) - \rho g z\right]dz + \overline{\int_{\overline{\eta}}^{\eta} \rho g(\eta - z)dz} + \frac{1}{2}\rho g(\overline{\eta}^2 - h^2) \\
&= \frac{1}{8}\rho g H_*^2 \left(\frac{2k(h+\overline{\eta})}{\sinh 2k(h+\overline{\eta})} + \frac{1}{2}\right)
\end{aligned}
\tag{B.11}
$$

In order to estimate the shear stress at arbitrary depth, $\tau(z)$, we determine the "Partial Radiation stress", $S_{xx}(z)$, as an integration of (B.10) from an arbitrary depth to free surface. $S_{xx}(z)$ is therefore defined as

$$
S_{xx}(z) = \overline{\int_z^{\eta} (p+\rho u^2)dz} + \int_z^{\overline{\eta}} \rho g z dz = \overline{\int_z^{\eta} (p+\rho u^2)dz} + \frac{1}{2}\rho g(\overline{\eta}^2 - z^2) \tag{B.12}
$$

Taking the similar approach, $S_{xx}(z)$ for linear wave theory is determined from (B.12) as

$$
S_{xx}(z) = \frac{1}{8}\rho g H_*^2 \left(\frac{2k(\overline{\eta} - z)}{\sinh 2k(h+\overline{\eta})} + \frac{1}{2}\right) \tag{B.13}
$$

Horizontal momentum balance equation from arbitrary depth, z, to the free-surface is then expressed by $S_{xx}(z)$ and $\tau(z)$ as

$$
\frac{\partial}{\partial x} S_{xx}(z) + \rho g(\overline{\eta} - z)\frac{\partial \overline{\eta}}{\partial x} + \tau(z) = 0 \tag{B.14}
$$

From (B.14),

$$
\frac{\partial \overline{\eta}}{\partial x} = \frac{-1}{\rho g(h+\overline{\eta})}\frac{\partial}{\partial x} S_{xx}(-h) - \frac{\tau_b}{\rho g(h+\overline{\eta})} \tag{B.15}
$$

where τ_b is the shear stress at the bottom, i.e., $\tau_b = \tau(-h)$. From (B.11), (B.13), (B.14) and (B.15), the shear stress at an arbitrary depth for the linear wave theory is therefore expressed as

$$\tau(z)=-\frac{\partial}{\partial x}\frac{1}{16}\rho g H_*^2\left(1-\frac{\overline{\eta}-z}{\overline{\eta}+h}\right)+\frac{\overline{\eta}-z}{\overline{\eta}+h}\tau_b \tag{B.16}$$

When $z=\overline{\eta}$, the shear stress at the mean water level, τ_s, is then expressed as

$$\tau_s=-\frac{1}{16}\rho g\frac{\partial H_*^2}{\partial x} \tag{B.17}$$

Figure-B.5 shows the vertical distribution of $S_{xx}(z)$ estimated both by SFM (B.12) and linear wave theory (B.13). The wave condition is $H_{SFM}/h=0.6$ and $h/L_0=0.02$, where the strong non-linearity is expected. From the figure, it is seen that both theories give close value around the free surface even though the strong non-linearity is expected.

To compare the partial radiation stresses around the free surface between both theories for various wave conditions, we should note following differences between SFM and linear wave theory. In SFM, as seen in (B.12), both velocity, u^2, and pressure, p, terms are included everywhere below the free surface. In linear wave theory, however, the velocity term is counted only below the mean water level because the velocity term becomes the third order above the trough level (B.11). Moreover, the pressure force above the trough level is evaluated at the mean water level although the integration range is from the trough level to the free surface. This feature is also seen in the Figure-B.5 as the partial radiation stress at the mean water level by linear wave theory has the value (B.17), which is coincident with the integration of the pressure term (the second term of (B.11)). In this sense, it is not consistent to compare the partial radiation stresses at the mean water level because linear wave theory includes pressure force above the trough level while SFM includes the components only above the mean water level. In this study, therefore, we compare the partial radiation stresses at the trough level. The partial radiation stresses in each theory are determined as follows.

$$S_{xxT,SFM} = \overline{\int_{\eta_t}^{\eta} (p + \rho u^2) dz + \frac{1}{2} \rho g (\overline{\eta}^2 - z^2)} \tag{B.18}$$

$$S_{xxT,linear} = \frac{1}{8} \rho g H_*^2 \left(\frac{2k(\overline{\eta} + a_*)}{\sinh 2k(h + \overline{\eta})} + \frac{1}{2} \right) \tag{B.19}$$

Figure-B.6 shows $S_{xxT,SFM}/S_{xxT,linear}$ as a function of h/L_0 and H_{SFM}/h. In the figure, it is seen that partial radiation stress determined by the equivalent linear wave theory coincident well with that obtained by SFM.

B.6 Summary

Observed facts are summarized as follows.

1. The non-linear wave height becomes much larger than the equivalent linear wave height when H/h (h/L_0) becomes larger (smaller).
2. The non-linear wave energy becomes slightly smaller than the equivalent linear wave energy.
3. In SFM, the kinetic energy becomes slightly larger than the potential energy when H/h becomes larger, i.e.; the wave non-linearity becomes significant.
4. Since non-linear wave energy becomes smaller than linear wave energy but the energy flux is conserved, the non-linear group velocity becomes larger than the equivalent linear group velocity.
5. The non-linear phase velocity also becomes larger than the equivalent linear phase velocity. However, the difference of these velocities is small compared with the difference of the wave heights.

6. The time-averaged mass transport obtained by SFM becomes smaller than that obtained by the equivalent linear wave theory when H/h becomes larger.
7. The feature noted in 6 is cased by the sharper shape of the non-linear wave profile. This sharper profile reduces the mass transport although the non-linear phase velocity is larger than that of equivalent linear wave theory.
8. The difference of the mass transport above the trough between SFM and the equivalent linear wave theory is less than 20% and it is expected that this difference becomes smaller for non-zero bottom slope condition because the bottom slope affects to make wave profile gentler. The use of the equivalent linear wave theory for mass transport is therefore reasonable even in the surf-zone.
9. The partial radiation stresses at the trough level obtained by SFM and the equivalent linear wave theory coincident well with each other. Therefore the use of the equivalent linear wave theory for the evaluation of the surface shear stress is reasonable even in the surf-zone.

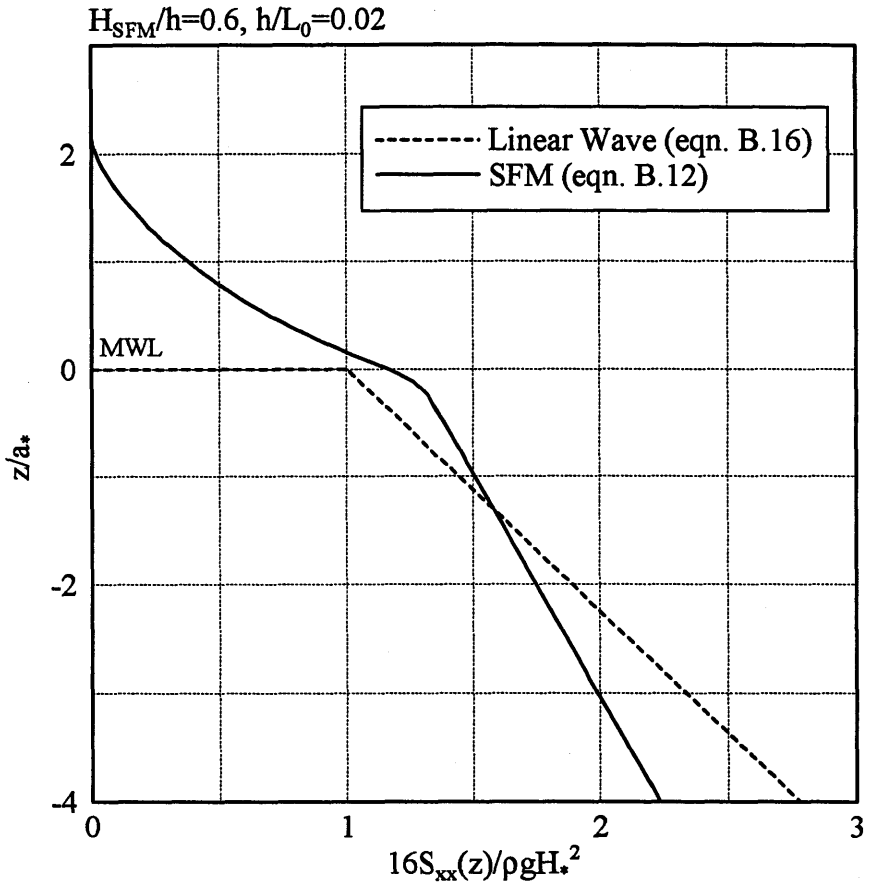

Figure-B.5 Comparison of S_{xx} between SFM and the equivalent linear wave theory

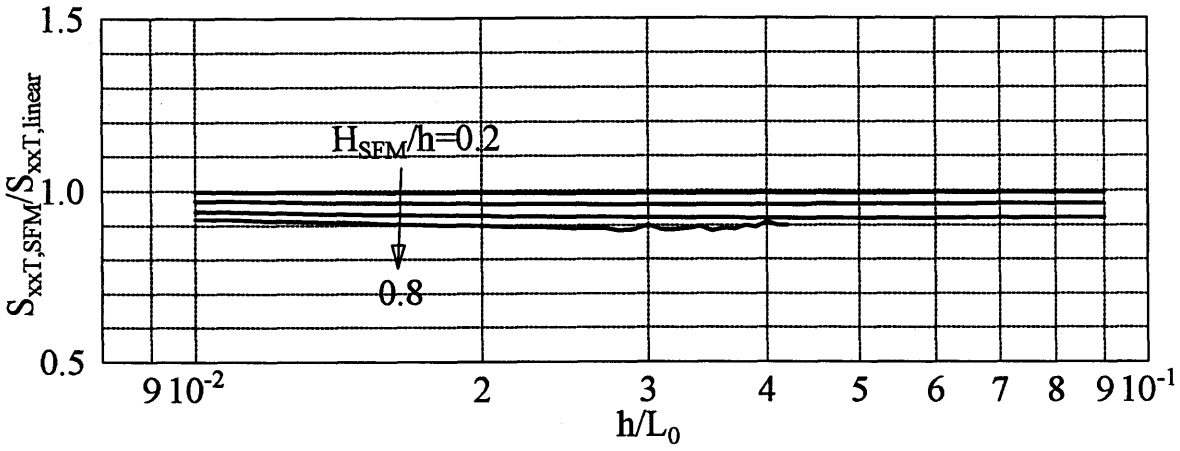

Figure-B.6 Comparison of S_{xxT} between SFM and the equivalent linear wave theory